

# Computer simulation of low-energy ion scattering

**Citation for published version (APA):**

Severijns, C. A. (1992). *Computer simulation of low-energy ion scattering*. [Phd Thesis 1 (Research TU/e / Graduation TU/e), Applied Physics and Science Education]. Technische Universiteit Eindhoven.  
<https://doi.org/10.6100/IR388788>

**DOI:**

[10.6100/IR388788](https://doi.org/10.6100/IR388788)

**Document status and date:**

Published: 01/01/1992

**Document Version:**

Publisher's PDF, also known as Version of Record (includes final page, issue and volume numbers)

**Please check the document version of this publication:**

- A submitted manuscript is the version of the article upon submission and before peer-review. There can be important differences between the submitted version and the official published version of record. People interested in the research are advised to contact the author for the final version of the publication, or visit the DOI to the publisher's website.
- The final author version and the galley proof are versions of the publication after peer review.
- The final published version features the final layout of the paper including the volume, issue and page numbers.

[Link to publication](#)

**General rights**

Copyright and moral rights for the publications made accessible in the public portal are retained by the authors and/or other copyright owners and it is a condition of accessing publications that users recognise and abide by the legal requirements associated with these rights.

- Users may download and print one copy of any publication from the public portal for the purpose of private study or research.
- You may not further distribute the material or use it for any profit-making activity or commercial gain
- You may freely distribute the URL identifying the publication in the public portal.

If the publication is distributed under the terms of Article 25fa of the Dutch Copyright Act, indicated by the "Taverne" license above, please follow below link for the End User Agreement:

[www.tue.nl/taverne](http://www.tue.nl/taverne)

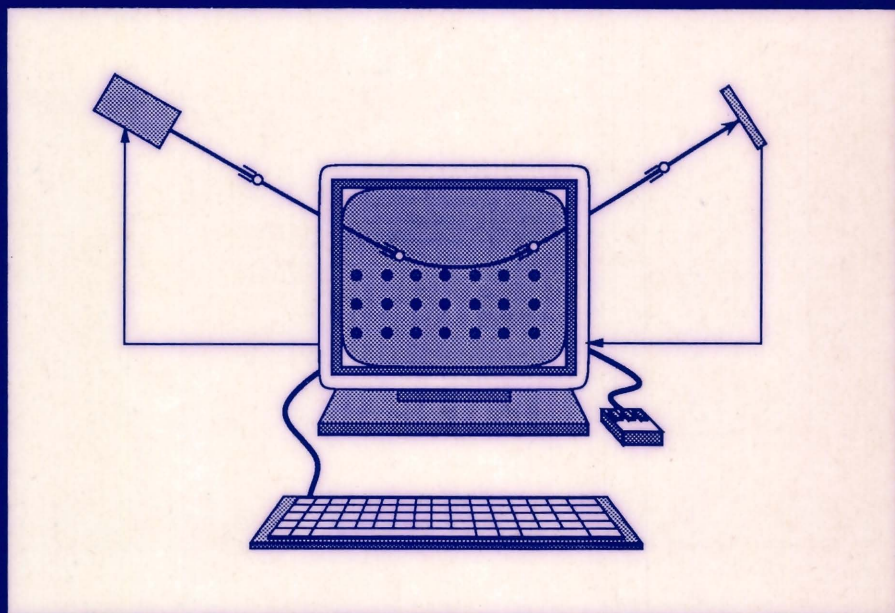
**Take down policy**

If you believe that this document breaches copyright please contact us at:

[openaccess@tue.nl](mailto:openaccess@tue.nl)

providing details and we will investigate your claim.

# Computer Simulation of Low-Energy Ion Scattering



**C.A. Severijns**

# Computer Simulation of Low-Energy Ion Scattering

## PROEFSCHRIFT

ter verkrijging van de graad van doctor aan de  
Technische Universiteit Eindhoven, op gezag van  
de Rector Magnificus, prof. dr. J.H. van Lint,  
voor een commissie aangewezen door het College  
van Dekanen in het openbaar te verdedigen op  
vrijdag 4 december 1992 om 16.00 uur

door

CAMILLUS ADRIANUS SEVERIJNS

Geboren te St.-Michielsgestel

Dit proefschrift is goedgekeurd  
door de promotoren  
prof. dr. H.H. Brongersma  
en  
prof. dr. J.T. Devreese



*Aan mijn ouders*

# Table of contents

<b>1</b>	<b>General introduction</b>	<b>1</b>
<b>2</b>	<b>Low-Energy Ion Scattering</b>	<b>5</b>
2.1	Introduction . . . . .	5
2.2	The binary-collision approximation . . . . .	6
2.3	Interaction potentials . . . . .	9
2.4	Inelastic energy loss . . . . .	10
2.5	Charge exchange . . . . .	12
2.6	Experimental equipment . . . . .	14
<b>3</b>	<b>The Simulation Code</b>	<b>19</b>
3.1	Introduction . . . . .	19
3.2	The global structure . . . . .	20
3.3	Supportive classes . . . . .	23
3.4	Three sample applications . . . . .	25
<b>4</b>	<b>Differential correction algorithm</b>	<b>29</b>
4.1	Introduction . . . . .	29
4.2	The differential correction algorithm . . . . .	30
4.3	Modifications for functions of two variables . . . . .	31
4.4	Physical problem: the LEIS collision integrals . . . . .	32
4.5	Results and discussion . . . . .	33
4.6	Conclusions . . . . .	39
<b>5</b>	<b>The SISS-92 computer code</b>	<b>41</b>
5.1	Introduction . . . . .	41
5.2	The simulation code . . . . .	42
5.3	Comparison with experiments . . . . .	46
5.4	Conclusions . . . . .	52
<b>6</b>	<b>Analytical results for the neutralization integral</b>	<b>55</b>
6.1	Introduction . . . . .	55

6.2	The ion fraction for a Coulomb trajectory . . . . .	58
6.3	Generalization of the neutralization rate . . . . .	59
6.4	Comparison of analytical and numerical results . . . . .	63
6.5	Conclusions . . . . .	64
<b>7</b>	<b>A computer study of charge exchange in LEIS</b>	<b>67</b>
7.1	Introduction . . . . .	67
7.2	Parameterizations for charge-exchange . . . . .	68
7.3	Experiments, simulations and fitting . . . . .	70
7.4	Results . . . . .	71
7.5	Discussion . . . . .	77
7.6	Conclusions . . . . .	78
<b>8</b>	<b>A preliminary study of the tails in LEIS spectra</b>	<b>81</b>
8.1	Introduction . . . . .	81
8.2	The motion of helium through the bulk . . . . .	82
8.3	Helium scattering from a tungsten surface . . . . .	89
8.4	Helium scattering from a silicon surface . . . . .	92
8.5	Conclusions . . . . .	95
	<b>Summary</b>	<b>97</b>
	<b>Samenvatting</b>	<b>99</b>
	<b>Dankwoord en curriculum vitae</b>	<b>101</b>
	<b>Publications</b>	<b>103</b>

# Chapter 1

## General introduction

Surfaces play an important role in a large number of industrial applications such as micro-electronics and chemistry. Due to the miniaturization of electronic devices, the surface-bulk ratio of these devices is increasing. Therefore, their properties are more and more determined by the surface. Nowadays, integrated circuits are often grown by depositing material on a semiconductor surface. Therefore, detailed information on the surface composition and structure is required for understanding and controlling the growth-process. For many chemical reactions a catalyst is needed in order to be useful. Since such a catalyst is often used as a solid, the reactions can only take place at the catalyst surface. As a result, the effectiveness of a catalyst depends on the structure and composition of its surface.

In surface science one studies the properties of and processes related to the interface between two media. In most cases one of these media is the vacuum and as a result the interface is a surface. Studying such a surface is more complicated than studying the bulk, both theoretically and experimentally. Theoretically, because the translational symmetry that simplifies the treatments of bulk properties, is not present perpendicular to the surface. Experimentally, because ultra-high vacuum conditions are needed in order to keep a freshly created or cleaned sample surface sufficiently long in its original state, since at ambient pressure a mono-layer may absorb in only  $10^{-9}$  s. Especially the fact that equipment guaranteeing ultra-high vacuum conditions only became available commercially in the early 1960's, caused the late start of surface science. Despite this, its results are widely applied in technological fields such as micro-electronics and heterogeneous catalysis.

The fact that the properties of a surface differ from those of the bulk can be illustrated in the following manner: consider an atom in the bulk. Such an atom is in equilibrium with all the atoms surrounding it. When a surface is made by cleaving a crystal, the bonds of the atoms at the cleavage plane are broken. Thus, the atoms at the freshly cut surface are no longer in equilibrium. By breaking the bonds the surface has also obtained extra energy, the *surface energy*. Therefore, in most cases the surface structure will change in order to minimize the surface

energy. This can be achieved by chemical bond formation with adsorbing particles, by atomic displacement either parallel (reconstruction) or perpendicular (relaxation) to the surface, or by change of the chemical composition of the outermost atomic layers (segregation).

There are many analytical techniques available in surface science to obtain information about a sample surface. Each of these has its advantages and drawbacks, and provides only a specific kind of information. Therefore, in general a combination of different analysis techniques is used to characterize a surface.

Most surface analysis techniques use the interaction of a beam of particles with the sample surface to obtain the information. These particles can be either ions, electrons or photons. An important aspect of a surface analysis technique is the *information depth*, i.e. the depth in the sample from which the information is obtained. The information depth depends on the mean free path of the particles, and thus determines the surface sensitivity of an analysis technique. Because most of the surface effects take place in the outermost atomic layers, the information depth should preferably be limited to only a few atomic layers. Low-energy ion scattering (LEIS) is such a technique.

In LEIS a primary beam of ions with an energy typically between 0.1 and 10 keV, is directed at a sample surface. The ions interact with the atoms in the surface and due to this interaction they lose a certain amount of energy. From this energy loss information on the elemental composition can be obtained. Because the interaction between an ion and an atom is repulsive, a certain area behind the atom cannot be reached by the impinging ion. This area is the *shadow cone*. Depending on the direction of the (parallel) primary ion beam, one surface atom can be inside or outside the shadow cone of a neighboring atom. This shadowing effect can be used to obtain structural information at an atomic scale.

In LEIS one very often uses a beam of noble gas ions. Due to their high neutralization probability, the fraction of particles, that return in a charged state after scattering from deeper layers, is very small. This and the fact, that only the ionized particles returning from the sample surface are analyzed, make LEIS a technique that is well suited to studying the outermost layers of atoms.

The interpretation of the spectra obtained with a LEIS technique is in general a difficult task, because a large number of particles is involved in the scattering process. Besides this, the ions are influenced by electronic processes, such as inelastic energy loss and neutralization, during the scattering process. Therefore, computer simulations are often used as an aid in the interpretation. In this thesis we will discuss the aspects, both physical and algorithmic, of ion-scattering simulation in order to develop a computer code that is well suited to LEIS simulation.

Two basic models for computer simulation have been worked out in the past: the classical dynamics (CD) model and the binary-collision approximation (BCA) model. In the CD model the movement of atoms in a solid is studied as a function

of time. Since all atoms within a finite volume are followed in small time steps, inter-atomic collisions are automatically included. The CD model is frequently used to study radiation damage in solids, such as, due to sputtering. It is not suited for ion-scattering simulation, because for most applications a large amount of computer time is required. In the BCA model the interaction of a moving particle with the atoms in the crystal is considered to be a sequence of successive binary collisions. This reduces the number of interactions that has to be considered dramatically. Since a semi-analytical solution to the single binary collision problem exists, the BCA model is often applied to ion-scattering simulation.

The programs based on the BCA model can be divided in two main categories: those, implementing a crystalline target structure, and those implementing random solids. A well-known example of the latter is the TRIM program [1], which was developed to study the transport of ions in matter. Several variations of this program exist, each for a specific application. Because the simulation of LEIS often requires a crystalline target structure in order to account for shadowing and blocking effects, this type of code is not suited for this purpose.

One of the most widely used simulation codes based on the BCA model that also implements a crystalline target structure, is the MARLOWE code [2]. Initially, this code was developed and used to study the implantation of ions in solids. It has also successfully been applied to ion-scattering problems. The MARLOWE code stimulated the development of a number of analogous codes, such as EDI [3], ARGUS [4], TAVERN [5], and several others. In these codes various methods are used to calculate a single binary collision and to search for the next collision partner. In some codes simultaneous collisions are handled or inelastic kinematics is treated. Others offer the possibility of tracing the recoil particles or taking thermal vibrations into account.

When the inter-atomic distances are much larger than the width of the shadow cones, the nuclear encounter concept can be applied [6]. In this case the path of the projectile can be approximated by straight incoming and outgoing trajectories. The projectile is scattered over a large angle only once. The thermal vibrations of the atoms in the crystal are used to calculate the scattering cross sections for a number of different trajectories, and these are combined into an intensity distribution of the backscattered projectiles. Since the shadow cones have to be small, the nuclear encounter concept can only be used when the energy of the projectiles is sufficiently high. This is in general not the case for simulations of LEIS.

Recently, a method was developed to calculate the angular dependence of the intensity for a projectile, which collides at most three times with two target atoms [7]. Experimentally the number of collisions per projectile can be limited by placing the detector near the source. Thus, the total scattering angle is almost  $180^\circ$ . This experimental set-up is used in impact-collision ion-scattering spectroscopy (ICISS) [8].

From the discussion presented above it will be clear that every code for ion-

scattering simulation is a trade-off between the amount of physics implemented, the generality of the applicability of the code, and the computer time required. In this thesis a new computer code, SISS-92 (Simulation of Ion-Surface Scattering 1992), for ion-scattering simulation is presented. It is based on the BCA model and implements a full three-dimensional simulation of ion scattering. Special attention has been paid to the efficiency of the code.

The contents of this thesis is as follows. In chapter 2, an overview of the theory of LEIS is given and a few experimental setups are described briefly. In chapter 3 the computer code is presented and its structure is discussed in detail. The main numerical procedures and algorithms implemented in the code are presented in the chapters 4 and 5. In the latter a comparison of experimental and simulation results is presented also. An important problem related to LEIS experiments is the fact, that the ions interact with the electrons in the surface leading to charge exchange (neutralization and ionization) between the ion and the surface. Although this is one of the main reasons for the high surface sensitivity of LEIS, it makes the quantitative interpretation of LEIS spectra more difficult. Therefore, charge exchange has to be considered in ion-scattering simulations. New analytical results for the neutralization integral in LEIS are presented in chapter 6. In chapter 7, the SISS-92 code is used to study charge exchange. A second important problem is the fact, that in many LEIS spectra a tail is observed at the low-energy side of the surface peaks. Such a tail is caused by ions that penetrate more deeply into the surface and are ionized just before they leave the surface. The phenomena that lead to the occurrence of tails are studied in chapter 8.

## References

- [1] J.P. Biersack, L.G. Haggmark, Nucl. Instr. Meth. 174 (1980) 257
- [2] M.T. Robinson, I.M. Torrens, Phys. Rev. B 9 (1974) 5008
- [3] E. Preuss, Rad. Eff. 38 (1978) 151
- [4] H.F. Helbig, M.W. Linder, G.A. Morris, S.A. Steward, Surf. Sci. 114 (1982) 251
- [5] D.P. Jackson, J. of Nucl. Mat. 93 & 94 (1980) 507
- [6] R.M. Tromp and J.F. van der Veen, Surf. Sci. 133 (1983) 159
- [7] R.S. Daley, J.H. Huang, R.S. Williams, Surf. Sci. 215 (1989) 281
- [8] M. Aono, Nucl. Instr. Meth. 49 (1984) 374

# Chapter 2

## Low-Energy Ion Scattering

### 2.1 Introduction

When an ion penetrates a solid, the ion will interact with the atoms in the solid. This interaction is a many particle problem and requires, at first instance, a quantum-mechanical description. Since the quantum-mechanical model is too complicated to be of any practical use for computer simulation, a number of approximations is made in order to obtain a much simpler model: the binary-collision approximation (BCA) model. This model forms the basis of most computer codes for ion-scattering simulation, such as, MARLOWE [1], TRIM [2], ARGUS [3], EDI [4], TAVERN [5], and the code by Tromp and van der Veen [6]. Simulation results obtained with such codes have been found to compare well with experimental data (see, e.g., [7–10]). In section 2.2 the BCA model and its validity are discussed.

An important issue in ion-scattering simulation is the choice of the interaction potential, since it describes all quantum-mechanical details of the interaction between an ion and an atom. Several interaction potentials are discussed in section 2.3.

Within a solid, an ion interacts not only with the atomic nuclei but also with the electrons. This interaction causes two types of electronic processes to occur: inelastic energy loss and charge exchange (neutralization and reionization). These are treated separately in the BCA model. In contrast to the scattering process, the electronic processes do require a quantum-mechanical description. Especially charge-exchange processes have a major impact on the spectra measured with low-energy ion-scattering equipment. This, because most commonly used detectors are based on electrostatic deflection and, as a result, are only able to detect ions. Although charge-exchange processes complicate the interpretation of the spectra, it also offers an advantage: the high neutralization rate of noble gas ions is used to make LEIS a highly surface-sensitive technique. Models for the inelastic energy loss are discussed in the section 2.4 and for charge-exchange processes in section 2.5.

Some knowledge of the equipment used in LEIS experiments is needed in order to



obtain simulation results that can be compared with experimental data. Therefore, a few experimental setups for LEIS experiments are discussed in the last section of this chapter.

Note that in this chapter the physics required to implement an ion-scattering simulation code is only summarized. More extensive reviews of both the physics and the numerical techniques needed to implement such a code can be found in the literature [11–14].

## 2.2 The binary-collision approximation

As was mentioned above, the interaction of an ion with the atoms in a solid requires a quantum-mechanical description. In order to obtain a model that is suited for simulation purposes a number of approximations is used. First, a classical description is used. This approximation is valid when diffraction effects can be neglected. This is the case for LEIS since the de-Broglie wavelength of the incident ion is much smaller than the inter-atomic distances in the solid [12]. Second, the interaction of the ion with the atoms is approximated by a sequence of binary collisions. In order for this approximation to be valid, two conditions have to be satisfied: (i) the atoms have to be almost non-interacting, and (ii) the ions have to interact with one atom at a time. The first condition is satisfied if the time per collision is much smaller than the phonon interaction time. From figure 2.1a, where the kinetic energy of a  $\text{Ne}^+$  ion with an initial energy of 1 keV is shown as a function of the time, it can be seen that the major changes in the kinetic energy take place within a time interval of  $10^{-15}$  s. On the other hand, the phonon frequency  $\nu$  in a solid is found to be typically  $10^{12}$  to  $10^{13}$  Hz [15]. Since  $1/\nu$  is much larger than the interaction time, the condition (i) is satisfied. Condition (ii) is also satisfied, since the distance at which the interaction between the ion and the atom occurs, is much smaller than the inter-atomic distances. From figure 2.1b it can be seen, that the trajectories of the ion and the recoil particle only deviate significantly from the asymptotic trajectories within a small volume around the target atom. This is due to the fact, that the interaction potential at distances comparable to the inter-atomic distances in the surface is negligible compared to the kinetic energy of the impinging ion. In the case of a Ne atom colliding with a Ni atom, the interaction potential is about 15 V at distance of about 1.5 Å. Therefore, it is allowed to approximate the exact trajectories by their asymptotes.

The classical binary collision problem can be solved using the laws of conservation of energy and momentum for a given interaction potential. In figure 2.2 the collision of an ion with an atom is shown and the relevant parameters are indicated. The masses of the ion,  $m_{ion}$ , and the target atom,  $m_{atom}$ , the initial energy of the ion,  $E_{i,1}$ , and the impact parameter,  $s$ , are initially known. From these the final asymptotic

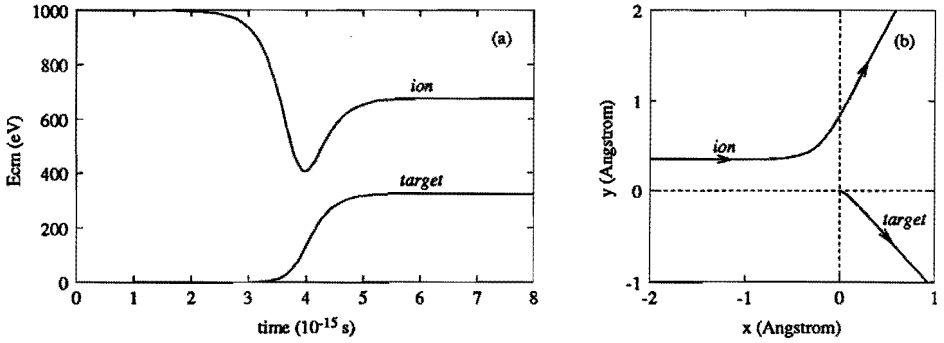


Figure 2.1: The interaction of a  $\text{Ne}^+$  ion of 1 keV with a Ni target atom for the Molière potential. In figure (a) the kinetic energies of the ion and the target are shown as a function of the time during the collision and in figure (b) the exact classical trajectories of the ion and the target atom are shown.

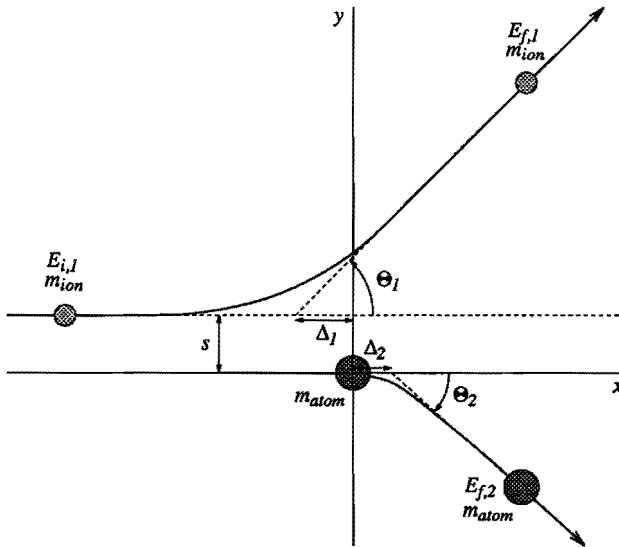


Figure 2.2: The classical binary collision in the laboratory system. The asymptotic trajectories of the projectile and the target are also shown. The parameters describing the collision of the projectile are indicated. The incoming and outgoing asymptotic trajectories of both particles are indicated by the dashed lines.

trajectories and the energies can be calculated of both the ion and the recoiled atom. The asymptotic trajectory of the ion follows directly from the scattering angle,  $\Theta_1$ , and the distance between the intersection of the asymptotes and the  $y$ -axis,  $\Delta_1$  in the laboratory system. When inelastic energy loss is not considered, these two quantities can be expressed in the scattering angle,  $\theta$ , in the center-of-mass system and the time integral,  $\tau$

$$\tan \Theta_1 = \frac{\sin \theta}{\frac{1}{\mathcal{A}} + \cos \theta} \quad (2.1)$$

$$\Delta_1 = \frac{-(\mathcal{A} - 1)s \tan(\frac{1}{2}\theta) - 2\tau}{(\mathcal{A} + 1)}, \quad (2.2)$$

where  $\mathcal{A} = m_{ion}/m_{atom}$ . The final energy of the ion  $E_{f,1}$  is given by

$$E_{f,1} = E_{i,1} - T \quad (2.3)$$

$$T = \frac{4\epsilon}{1 + \mathcal{A}} \sin^2(\frac{1}{2}\theta). \quad (2.4)$$

Here,  $T$  is the elastic energy loss during the collision and  $\epsilon$  is the center-of-mass energy. Note that similar expressions can be derived for the scattering angle,  $\Theta_2$ , the distance  $\Delta_2$ , and the final energy of the recoiled atom,  $E_{f,2}$ .

The scattering angle,  $\theta$ , in the center-of-mass system, the time integral,  $\tau$ , and the center-of-mass energy,  $\epsilon$ , are given by

$$\theta = \pi - 2s \int_{R_0}^{\infty} \frac{dr}{r^2 f(r)} \quad (2.5)$$

$$\tau = \sqrt{R_0^2 - s^2} - \int_{R_0}^{\infty} \left\{ \frac{1}{f(r)} - \frac{1}{\sqrt{1 - (\frac{s}{r})^2}} \right\} dr \quad (2.6)$$

$$\epsilon = \frac{\mathcal{A}}{1 + \mathcal{A}} E_{i,1}, \quad (2.7)$$

where

$$f(r) = \sqrt{1 - \left(\frac{s}{r}\right)^2 - \frac{V(r)}{\epsilon}}. \quad (2.8)$$

The distance of closest approach,  $R_0$ , can be calculated from  $f(R_0) = 0$ .

When the trajectories for several impact parameters are plotted, it appears that there is an area behind the target, where no ion can penetrate (see figure 2.3). This area is called the *shadow cone*. Also note, that the intensity of the ions is higher at the edge of the shadow cone due to the *focussing* effect. Both the shadow cone and the focussing effect can be used to determine the structure of a surface at an atomic scale.

With the expressions presented above, the collision of an ion with an atom is fully described. However, in order to be useful a suitable potential,  $V(r)$ , has to

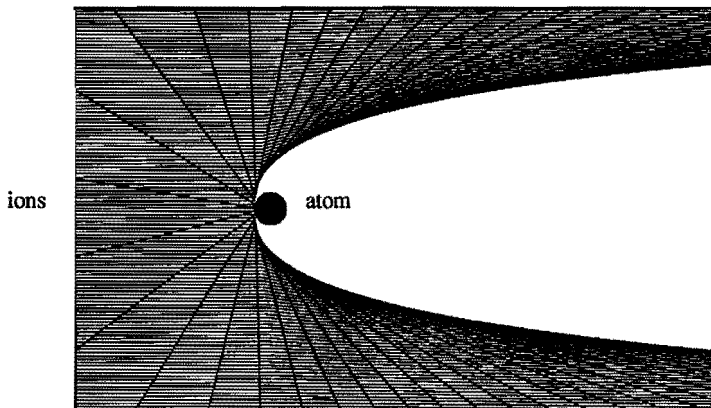


Figure 2.3: The shadow cone behind an atom, which is obtained by plotting the asymptotic trajectories of the ion for various values of the impact parameter.

be selected, that describes the interaction of the two particles. This is not an easy task, since all the details of the interaction between the two atoms is incorporated in the interaction potential. Several interaction potentials have been proposed in the literature. In the next section some of the most commonly used potentials are discussed.

## 2.3 Interaction potentials

The interaction potentials, that are generally used to describe the interaction of two atoms, depend only on the nuclear charges of the atoms and their inter-nuclear distance. Because the dependence on only these three parameters is convenient, such potentials are used in most computer codes for ion-scattering simulation. An overview of the different interaction potentials has been presented by Torrens [16].

Various interaction potentials have been proposed in the literature. Most of these are only repulsive, but some also have an attractive part. The last type of potential is required at very low energies or for grazing angles, when attractive forces may become significant. For LEIS simulations, the energy of the particles is in general sufficiently high to neglect such an attractive part in the interaction potential.

A repulsive interaction potential, that is often used in ion-scattering simulation codes based on the BCA model, is the screened Coulomb potential. This type of interaction potential has the general form

$$V(r) = \frac{Z_1 Z_2 e^2}{4\pi\epsilon_0 r} \Phi\left(\frac{r}{a}\right) = \frac{C}{r/a} \Phi\left(\frac{r}{a}\right), \quad (2.9)$$

where  $\Phi(x)$  is the screening function, which represents the screening of the nuclear

charge by the surrounding electrons. The screening length,  $a$ , is given by

$$a = \left( \frac{9\pi^2}{128} \right)^{1/3} a_B Z_{eff}^{-1/3} \quad (2.10)$$

$$Z_{eff} = (Z_1^\alpha + Z_2^\alpha)^\beta, \quad (2.11)$$

where  $a_B$  is the Bohr radius. This is analogous to the screening length in the Thomas-Fermi model of the atom [17,18], in which  $\alpha\beta = 1$ . An advantage of using this type of screening length is, that the interaction potential can be written in a universal form that does not depend on the specific combination of atoms under consideration. As a result, the integrals in the Eqs. (2.5) and (2.6) can also be written in such a form.

A well-known interaction potential of the screened-Coulomb type is the Molière potential [19], which is an analytical approximation to the Thomas-Fermi potential. In this case, the screening function is given by

$$\Phi(x) = 0.35 e^{-0.3x} + 0.55 e^{-1.2x} + 0.10 e^{-6x} \quad (2.12)$$

and usually the screening length by Firsov is used ( $\alpha = 1/2, \beta = 2$  in Eq. (2.11)). The Firsov screening length is often multiplied by an extra factor between 0.7 and 1 in order to obtain a better fit with experimental data [21]. The Molière potential is widely used for simulation purposes, since it is easy to evaluate and quite accurate [1-5].

The ZBL potential, which is similar to the Molière potential, was proposed by Ziegler, Biersack, and Littmark [22]. The screening function was determined by fitting to the interaction potential of about 500 ion-target combinations. It is given by

$$\begin{aligned} \Phi(x) = & 0.028171 e^{-0.20162x} + 0.28022 e^{-0.40290x} \\ & + 0.50986 e^{-0.94229x} + 0.18175 e^{-3.1998x}. \end{aligned} \quad (2.13)$$

The screening length is defined as in Eqs. (2.10) and (2.11), but in this case  $\alpha = 0.23$  and  $\beta = 3$  and, as a result,  $\alpha\beta = 0.69$ .

## 2.4 Inelastic energy loss

Atoms moving in a solid interact not only with the atoms but also with the electrons. Due to this interaction either or both colliding particles can be excited or ionized, which results in an additional loss of energy: the *inelastic* energy loss. The inelastic energy loss is called *localized*, when the energy loss takes place within the electronic shells of atoms. Inelastic energy loss can also be due to the interaction with the electron gas within a solid. Since, in this case, the energy loss is spread continuously

along the trajectory of the atom in the solid, it is referred to as *continuous* energy loss.

In contrast to the motion of the atomic nucleus, the inelastic energy loss requires a quantum-mechanical description. Fortunately, the mass of the electrons is much smaller than the mass of the nucleus. As a result, the electrons can be treated separate from the nucleus.

One of the first models for localized inelastic energy loss is due to Firsov [20]. In this model it is assumed that the collision lasts long enough for complete mixing of the electrons in the overlap region of the colliding atoms. The final result of the derivations shows that the inelastic energy loss  $Q_F$  depends only on the kinetic energy and the impact parameter

$$Q_F(E, s) = \frac{\alpha_{12}\sqrt{E}}{1 + \beta_{12}s^5}. \quad (2.14)$$

Here,  $\alpha_{12}$  and  $\beta_{12}$  are constants that depend only on the masses and charges of the two atoms.

The model by Firsov was derived for heavy atoms, which have many electrons. Therefore, this model may not be a good approximation for light atoms. Based on the observation that the screening function of the interaction potential decays exponentially, Oen and Robinson [23] proposed a model similar to the one by Firsov, that is more appropriate for light atoms

$$Q_{OR}(E, s) = \frac{d_1^2 K \sqrt{E}}{2 \pi a^2} \exp[-d_1 R_0(E, s)/a]. \quad (2.15)$$

Here,  $d_1$  depends on the screening function in the interaction potential,  $a$  is the screening length, and  $R_0$  is the distance of closest approach. The factor  $K$  is that proposed by Lindhard and Scharff in their model for continuous inelastic energy loss [24]. Thus, at high energies the stopping cross-section in the Oen-Robinson model,  $S_{OR}$ , given by

$$S_{OR}(E) = 2\pi \int_0^{s_{max}} s Q_{OR}(E, s) ds, \quad (2.16)$$

is approximately equal to the one in the Lindhard-Scharff,  $S_{LS}$ , at high energies.

From the assumption that the electron gas in a solid behaves like a viscous medium for the moving ion, an inelastic stopping cross-section is found, that is proportional to the velocity of the ion. In the Lindhard-Scharff model, the stopping cross-section for the continuous inelastic energy loss is given by

$$S_{LS}(E) = 8\pi\sqrt{2} a_B \hbar \frac{Z_1^{7/6} Z_2}{(Z_1^{2/3} + Z_2^{2/3})^{3/2}} \sqrt{\frac{E}{M_1}} = K\sqrt{E}. \quad (2.17)$$

In order to incorporate the oscillations in the inelastic stopping as function of  $Z_2$ , one often introduces an extra fitting parameter.

For computer simulations, simple fitted curves offer an advantage in speed. Such curves have been tabulated for helium in all elements by Ziegler [25]. A similar work for hydrogen has been presented by Andersen and Ziegler [26].

The models discussed above, describe the experimental data on electronic stopping obtained at high energies well. However, at low energies such data is not available. Theoretically, the electronic stopping should also be proportional to the velocity in this energy range. Due to the specific electronic structure, large deviations of this dependence can occur [27]. In practice, one usually relies on the Lindhard-Scharff model for heavy ions and the Oen-Robinson model for light ions.

## 2.5 Charge exchange

The inelastic energy loss is not the only process resulting from the interaction of a moving atom with the electrons. It is also possible for the atom to exchange an electron with the solid. Thus, a moving ion may be neutralized by capturing an electron, and a moving neutral atom may be ionized by losing an electron.

An ion can be neutralized by either of two processes: Auger and resonant neutralization (see figure 2.4a). In the case of Auger neutralization, two electrons are involved: one moves from the conduction band to an inner shell of the ion. The energy released by this transition is used to free the second electron from the conduction band. In the case of resonant neutralization a single electron in the conduction band is transferred to a shell of the ion, which is lead to an excited state. Quasi-resonant neutralization is a similar process, but in this case, the energy levels of the ion and surface, that are involved, do not match perfectly. Note that the kinetic energy of the ion is not changed by these neutralization processes.

Reionization of an atom occurs by a process that is similar to resonant neutralization, but here the electron moves from the atom to the conduction band of the solid (see figure 2.4b). Note that reionization does result in an extra loss of kinetic energy of the atom.

It was shown by Hagstrum [28], that the survival probability  $P^+$  of an ion at low energies ( $< 100$  eV) can be expressed as

$$P^+ = \exp \left( \int_{-\infty}^{+\infty} R(\vec{r}(t)) dt \right), \quad (2.18)$$

where  $R(\vec{r})$  is the transition probability and  $\vec{r}(t)$  is the trajectory of the ion. Hagstrum supposed that the transition probability only depends on the perpendicular distance,  $z(t)$ , between the ion and the surface

$$R(\vec{r}) = Ae^{-az(t)}. \quad (2.19)$$

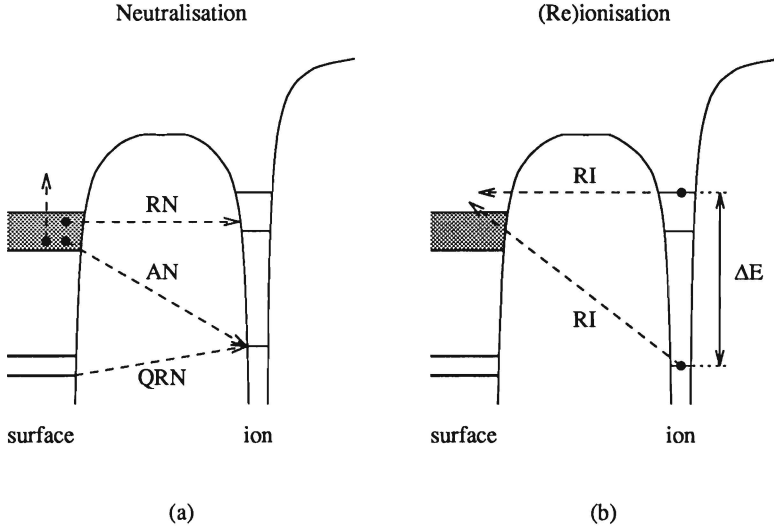


Figure 2.4: The charge exchange processes. In figure (a) the neutralization processes and in figure (b) the reionization processes are shown schematically. The following processes are indicated: Auger neutralization (AN), resonant neutralization (RN), quasi-resonant neutralization (QRN), and resonant ionization (RI).

Here,  $A$  and  $a$  are the neutralization constants. The values of these constants depend on the kind of transition that is considered. If the change in the velocity of the ion is neglected Eq. (2.18) can be written as

$$P^+ = \exp\left(-v_c \left(\frac{1}{v_{in\perp}} + \frac{1}{v_{out\perp}}\right)\right), \quad (2.20)$$

where  $v_{in\perp}$  and  $v_{out,\perp}$  are the velocities on the incoming and outgoing trajectories perpendicular to the surface. The characteristic velocity  $v_c$  is given by

$$v_c = \int_{R_0}^{\infty} R(z) dz = \frac{A}{a} e^{-aR_0}. \quad (2.21)$$

The model by Hagstrum is only valid for low energy ions approaching a metal surface. However, in other, non-metal cases a localized transition probability, although it is still an approximation, is better suited

$$R(r) = A e^{-ar}. \quad (2.22)$$

Here,  $r$  is the distance between the ion and the atom in the solid. For a few simple trajectories, the ion fraction can be calculated analytically for a localized transition



probability. Godfrey and Woodruff approximated the trajectory of the ion by the incoming asymptote and obtained the following [29]

$$P^+ = \exp\left(-\frac{2A}{av}(as)K_1(as)\right), \quad (2.23)$$

where  $s$  is the impact parameter. The velocity,  $v$ , of the ion is presumed to be constant. Richard and Eschenbacher derived a similar expression, while taking into account the curvature of the ion trajectory by incorporating an extra parameter [30]. This parameter is fitted to the interaction potential.

A general model that incorporates both the model by Hagstrum and the localized model as its limiting cases, has been proposed by Verbist *et al.* [31]. This model considers the neutralization of the ion by a number of atoms.

## 2.6 Experimental equipment

A setup for an ion-scattering experiment consists of a combination of an ion source and mass filter, which is used to generate a mono-atomic ion beam, a manipulator to hold and manipulate the target, and a detector. One can distinguish two main types of detectors: those, that determine the speed of the scattered particles by measuring the time these particles take to travel a given distance (time-of-flight, TOF), and those, that measure the energy of the scattered particles by means of electrostatic deflection. With the TOF-type of detector it is possible to detect both charged and neutral atoms, but with the electrostatic analyzers only ions can be detected. Since LEIS is a very surface-sensitive technique, a slight contamination of the sample surface may strongly influence the experimental results. In order to maintain a clean surface all parts of the experimental setup should be placed in ultra high vacuum (UHV).

In order to measure the time needed by the scattered particles to travel the distance from the sample to the detector, a reference point in time is needed. Such a point is obtained by chopping the primary ion beam in ion pulses with a small time width using a set of deflection plates and a diaphragm. A typical setup for a time-of-flight experiment is shown schematically in figure 2.5.

A special application of the TOF technique is impact-collision ion-scattering spectroscopy (ICISS) [32]. Here, one uses the shadow cones to determine the structure of the surface on an atomic scale. In this case, the total scattering angle,  $\Theta$ , is kept fixed at almost  $180^\circ$ , while the angle  $\alpha$  between the primary ion beam and the sample surface is varied. The measured intensity of the backscattered ions is outlined in figure 2.6. For small values of  $\alpha$  all ions are scattered forward and, as a result, no backscattered ions can be detected. When the edge of the shadow cone touches the neighbouring atoms, the intensity of the backscattered ions increases quickly and reaches a maximum due to focusing. For larger values of  $\alpha$ , focusing at

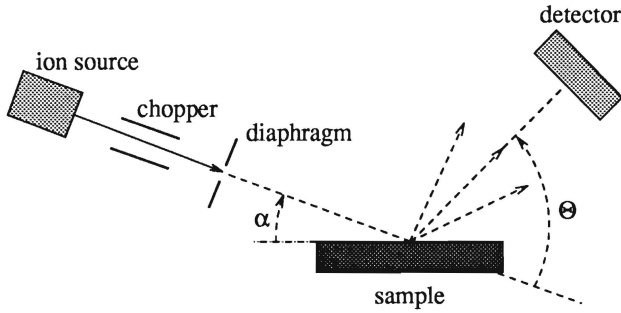


Figure 2.5: A typical setup for a time-of-flight experiment. The main parts are shown. The total scattering angle  $\Theta$  and the angle  $\alpha$  between the primary ion beam and the sample surface are also indicated.

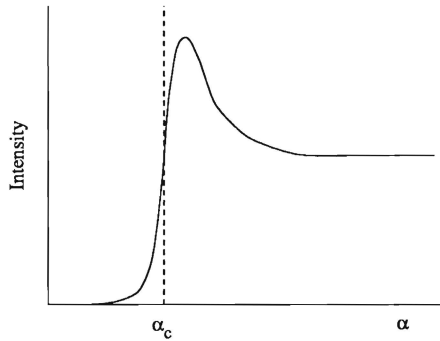


Figure 2.6: The measured ion intensity in an ICISS experiment. The critical angle,  $\alpha_c$ , corresponds roughly with the angle at which the edge of the shadow cone reaches the neighbouring atom.

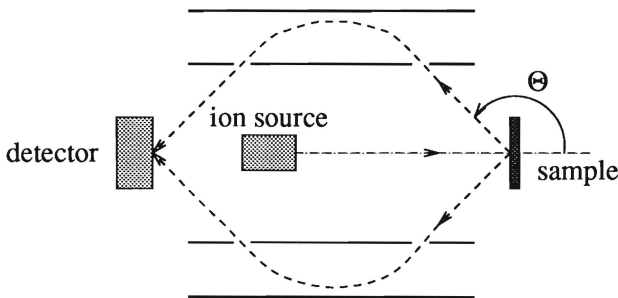


Figure 2.7: The cylindrical mirror analyzer. The electric field between the two cylinders determines the energy of the ions that can pass through the two slits in the inner cylinder.

the neighbouring atom does not occur and, as a result, the intensity is independent of  $\alpha$ .

It is also possible to measure recoiled particles with TOF. In order to achieve this, a small total scattering angle,  $\Theta$ , is chosen. In this manner light atoms, such as hydrogen, recoiled from the surface can also be detected. An example of this technique is time-of-flight scattering and recoiling spectrometry (TOF-SARS) [33].

An example of an electrostatic analyzer is the cylindrical mirror analyzer (CMA) (see figure 2.7). It consists of two cylinders which are kept on a different potential. Only ions with a specific energy can pass the two slits in the inner cylinder. Thus, the energy of the ions can be selected by varying the voltage difference between the two cylinders. In the CMA the intensity of the backscattered ions is integrated over the azimuthal angle for a fixed value of the total scattering angle,  $\Theta$ .

In order to measure the azimuthal distribution and the energy of the ions simultaneously, Hellings *et al.* have developed a double toroidal electrostatic analyzer [34]. This analyzer preserves the azimuthal distribution of the ions and images their energy in the radial direction. A two-dimensional position sensitive detector is used to determine the radius and azimuthal angle of each ion that leaves the analyzer [35,36]. This detection system is used in the energy and angle resolved ion spectroscopy (EARISS) apparatus.

## References

- [1] M.T. Robinson, I.M. Torrens, Phys. Rev. B **9** (1974) 5008
- [2] J.P. Biersack, L.G. Hagmark, Nucl. Instr. Meth. **174** (1980) 257
- [3] H.F. Helbig, M.W. Linder, G.A. Morris, S.A. Steward, Surf. Sci. **114** (1982) 251
- [4] E. Preuss, Rad. Eff. **38** (1978) 151
- [5] D.P. Jackson, J. of Nucl. Mat. **93 & 94** (1980) 507
- [6] R.M. Tromp and J.F. van der Veen, Surf. Sci. **133** (1983) 159
- [7] T. von dem Hagen, M. Hou, E. Bauer, Surf. Sci. **117** (1982) 134
- [8] H. Niehus, E. Preuss, Surf. Sci. **119** (1982) 349
- [9] J.H. Huang, R.S. Daley, D.K. Shuh, Surf. Sci. **186** (1987) 115
- [10] E. Pierson, J.-M. Beuken, P. Bertrand, Surf. Sci. **214** (1989) 560

- [11] C. Lehmann, *Interaction of Radiation with Solids and Elementary Defect Production*, North-Holland, Amsterdam 1965
- [12] G. Liebfried, *Bestrahlungseffekte in Festkörpern*, Teubner, Stuttgart 1965
- [13] E.S. Mashkova, V.A. Molchanov, *Medium-Energy Ion Reflection from Solids*, Modern Problems in Condensed Matter Sciences, vol. 11, North-Holland, Amsterdam 1985
- [14] W. Eckstein, *Computer Simulation of Ion-Solid Interactions*, Springer Series in Materials Science 10, 1991
- [15] J.R. Hook, H.E. Hall, *Solid State Physics*, 2-nd ed., The Manchester Physics Series, Wiley, 1991
- [16] I.M. Torrens, *Inter-atomic potentials*, Academic Press, London 1972
- [17] L.H. Thomas, Proc. Cambridge Philos. Soc. 23 (1927) 542
- [18] E. Fermi, Z. Phys. 48 (1928) 73
- [19] G. Molière, Z. Naturforsch. 2a (1947) 133
- [20] O.B. Firsov, Sov. Phys. JETP 6 (1958) 534
- [21] See, e.g., Th. Fauster, M.H. Metzner, Surf. Sc. 166 (1986) 29
- [22] J.F. Ziegler, J.P. Biersack, U. Littmark, *The Stopping and Range of Ions in Solids*, The Stopping and Range of Ions in Matter, Vol. 1, ed. by J.F. Ziegler, Pergamon, New York 1985
- [23] O.S. Oen, M.T. Robinson, Nucl. Instr. and Meth. 132 (1976) 647
- [24] J. Lindhard, M. Scharff, Phys. Rev. 124 (1961) 128
- [25] J.F. Ziegler, *Helium Stopping Powers and Ranges in All Elements*, The Stopping and Range of Ions in Matter, Vol. 4, ed. by J.F. Ziegler, Pergamon, New York 1977
- [26] H.H. Andersen, J.F. Ziegler, *Hydrogen Stopping Powers and Ranges in All Elements*, The Stopping and Range of Ions in Matter, Vol. 3, ed. by J.F. Ziegler, Pergamon, New York 1977
- [27] Y. Muda, D.M. Newns, Phys. Rev. B 37 (1988) 7048
- [28] H.D. Hagstrum, Phys. Rev. 96 (1954) 338
- [29] D.J. Godfrey, D.P. Woodruff, Surf. Sci. 105 (1981) 438

- [30] A. Richard, H. Eschenbacher, Nucl. Instr. Meth. B2 (1984) 444
- [31] G. Verbist, J.T. Devreese, H.H. Brongersma, Surf. Sci. 233 (1990) 201
- [32] M. Aono, Nucl. Instr. Meth. B2 (1984) 374
- [33] O. Grizzi, M. Shi, H. Bu, J.W. Rabalais, Rev. Sci. Instrum. 61 (1990) 740
- [34] G.J.A. Hellings, H. Ottevanger, S.W. Boelens, C.L.C.M. Knibbeler, H.H. Brongersma, Surf. Sci. 162 (1985) 913
- [35] C.L.C.M. Knibbeler, G.J.A. Hellings, H.J. Maaskamp, H. Ottevanger, H.H. Brongersma, Rev. Sci. Instr. 58 (1987) 125
- [36] P.A.J. Ackermans, P.H.F.M. van der Meulen, H. Ottevanger, F.E. van Straten, H.H. Brongersma, Nucl. Instr. Meth. B35 (1988) 541

# Chapter 3

## The Simulation Code

### 3.1 Introduction

In this chapter an overview of the SISS-92 code is presented. The main goal during the development of this code was to obtain maximum flexibility and modularity of the code, while a simple and comprehensible interface to the application code is provided. The latter was achieved by structuring the code similar to the experimental setup. It appeared that an object-oriented approach was best-suited for this purposes. A well-known object-oriented programming language is the C++ language [1]. It combines an object-oriented grammar with static type checking. As a result of the latter, a very efficient machine code can be generated by a compiler. This is advantageously for the development of an ion-scattering simulation code, since, in general, such simulations require a large amount of computer time and, as a result, efficiency considerations are of great importance.

Since C++ is a relative new programming language, it is useful to introduce it briefly. The most important concept is the *class*. This is the basic building block in every C++ program. Every class contains one or more *members*. Each member can be either a function or a datum. In addition, a mechanism is provided to control the access to the members of a class. They can be either *public*, *private*, or *protected*. Public members can be accessed by any function, but private and protected members only by member functions of the class. Protected data members can also be accessed by member functions in derived classes and, as a result, the access to these members is less restricted.

A class, that inherits all members from a *base* class, and adds new members to them, is called a *derived* class. Derivation is a very useful mechanism, since it allows one to extend the functionality of an existing class. It can, e.g., be used to implement general concepts, such as lists and arrays, independent of the actual type of the data.

Certain operations cannot be implemented elegantly in a single class or as a member function. Therefore, a class can permit access to its private and protected data

members to specific functions and classes. These are called *friends* of the class.

All this makes the C++ language very suitable to implement a flexible, efficient, and easy to maintain and extend simulation code. This will be further illustrated in the discussion of the structure of the SISS-92 simulation in the remainder of this chapter. In section 3.2 an overall view of the structure of the code is given. A number of classes, such as lists of various types of objects, is derived from a small number of basic classes. Other classes are used only internally in the SISS-92 code. These classes are discussed in section 3.3. Finally, as an illustration of how the code can be used and extended, three sample applications are discussed in section 3.4.

## 3.2 The global structure

The structure of the code is shown schematically in figure 3.1. The main classes shown in this figure are the **Collision**, **Cascade**, and **Simulation** classes. They are indicated by printing their names in a bold face. Derivation is indicated by connecting two names by a thick line with an arrow head, which starts at the base class and ends at the derived class. Most classes need other classes for their implementation. This is indicated by listing the names of these internal classes below the class name and connecting them with a thin line. Some of the internally used classes can be controlled by or are provided by the application code. This is indicated by using a normal face. The names of the remaining classes are printed in an italic face.

As is shown in figure 3.1, the **Collision** class is a basic class. It is used to calculate a single binary collision of an ion and a target atom. The *Integral* class, which calculates the classical collision integrals, is used for this purpose. During a collision the projectile can loose energy by inelastic processes and it can be neutralized or re-ionized. The classes *Inelasticity* and *Neutralization* can be provided by the application to take these processes into account. Furthermore, the **Collision** class has been prepared to incorporate target displacement. The *TargetDisplacement* class is provided for this purpose.

The **Cascade** class calculates a sequence of binary collisions and is derived from the **Collision** class. It uses three classes for its implementation. The *Collision-EventQueue* class maintains a time-ordered queue of collision events that remain to be calculated. The *Surface* class is used to determine the target atoms visited by the ion. Two objects of the *CollisionOperatorList* class are contained in the **Cascade** class. These are provided to enable adding extra functionality to the cascade calculation, that does not require detailed information on the collision process. The objects on the (Pre)CollisionList are called before the collision, the objects on the (Post)CollisionList after the collision. These lists can, e.g., be used to provide graphical output of the ion trajectories.

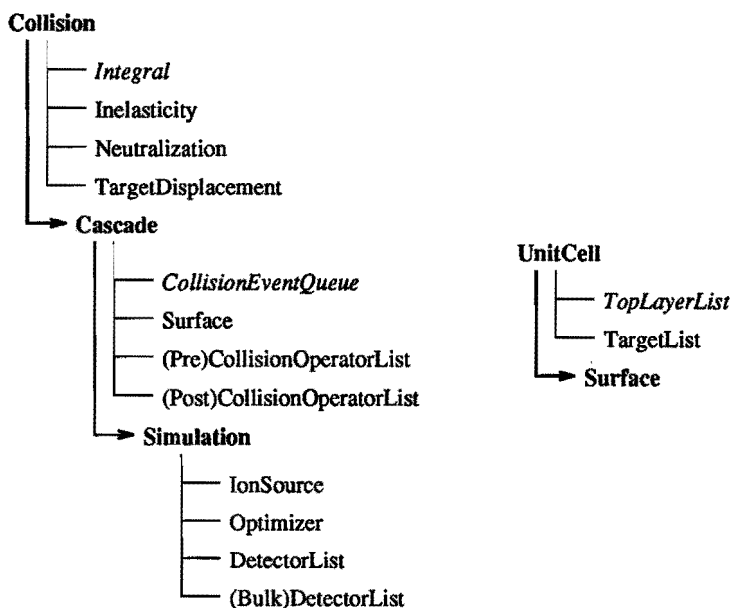


Figure 3.1: The main classes of the SISS-92 code.

The actual simulation is controlled by the **Simulation** class. This class is derived from the **Cascade** class. Three other classes are used in its implementation: the **IonSource**, **Optimizer**, and **DetectorList** classes. First the **IonSource** class is used to generate an ion. Then, when provided, the **Optimizer** class is used to check if the ion can be detected, and if it can be detected, the cascade is calculated. The **Simulation** class contains a list of detectors, which enables a number of experimental setups using the same ion source to be simulated in one run of the program. The detectors on this list are used when the ion enters the vacuum at the end of a cascade. For studying the transport of the ions through the crystal, a second list of detectors is provided. These are used when the ion disappears into the bulk. At the end of each cascade, the **Optimizer** class is informed on the fact that the ion was detected or not.

The crystal structure is implemented with two classes: the **UnitCell** and **Surface** classes. The **UnitCell** class provides facilities for searching for target atoms within a single lattice unit-cell. The targets within this unit-cell are given in the **TargetList** class. The **TopLayerList** class contains information on the atoms that are at the top of the unit-cell. This information is used to find the first target atom in a cascade. The periodicity of the surface is implemented in the **Surface** class by repeating the



unit-cell. This class also maintains information on the absolute position of the ions within the surface.

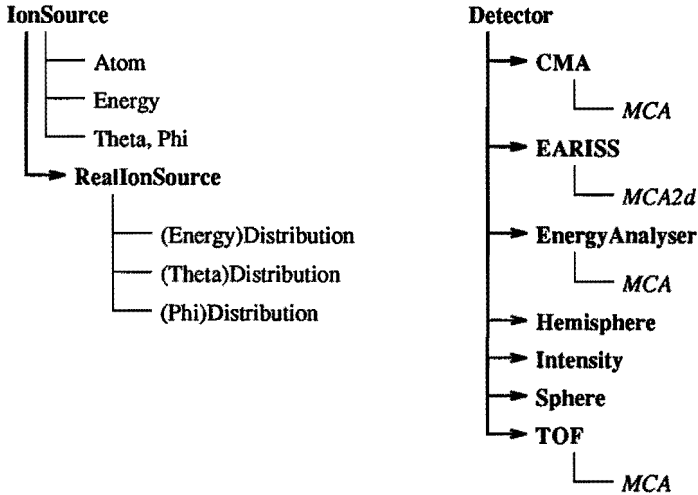


Figure 3.2: The **IonSource** and **Detector** classes and the classes derived from them. The abstract **Detector** class only provides an interface. The implementation is contained in the derived classes. Several simulated detectors are implemented, such as a cylindrical mirror analyzer (**CMA**), an energy and angle resolving analyzer (**EARISS**), an energy analyzer with a rectangular or circular shape, and a time-of-flight detector (**TOF**).

Two classes needed in every simulation are the **IonSource** and **Detector** classes (see figure 3.2). The **IonSource** class implements an idealized ion source with a mono-energetic ion beam without divergence. The internal classes are used to generate an ion. The **RealIonSource** class implements an ion source with an energy spread and a divergence in a solid angle. For this purpose three Distribution classes are used: **(Energy)Distribution**, **(Theta)Distribution**, and **(Phi)Distribution**.

The **Detector** is an *abstract* class, which means that it provides an interface without an implementation. The latter is provided by a derived class. Several detectors are implemented in the SISS-92 code: a cylindrical mirror analyzer (**CMA**), an analyzer that records both the energy and azimuth of an impinging ion (**EARISS**) [2], an energy analyzer with a rectangular or circular shape (**EnergyAnalyzer**), a detector that only counts the number of ions entering it (**Intensity**), and a time-of-flight analyzer (**TOF**). Several of these classes use the **MCA** class, that simulates a multi-channel analyzer. This type of re-use is simplified by the use of an object-oriented

programming language.

The **Hemisphere** and **Sphere** classes write the energy and direction of the ion to a file for later processing. The **Sphere** class does this for every ion, but the **Hemisphere** class only for ions that move in the positive z-direction, i.e., from the surface to the vacuum.

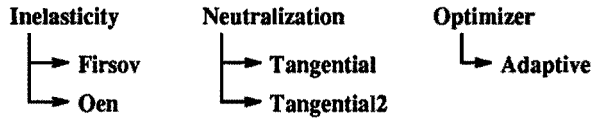


Figure 3.3: The **Inelasticity**, **Neutralization**, and **Optimizer** classes are not required for a simulation. They are abstract base classes which enable the application code to influence certain aspects of the simulation. The **Inelasticity** and **Neutralization** class influence the collision of an ion with a target atom and the **Optimizer** is used to optimize the calculation of scattering cascades.

Three classes can be optionally provided by the application. These are shown in figure 3.3. All three classes are abstract classes. The **Inelasticity** class is used to calculate inelastic energy loss. Currently, the model by Firsov [3] and the model by Oen and Robinson [4] have been implemented.

Charge exchange is calculated by the **Neutralization** class. Only the neutralization model by Richard and Eschenbacher [5] is implemented in the current version.

For certain applications, the area of the surface unit-cell on which cascades have to be calculated, can be restricted either in advance or by statistical information obtained during the simulation. For this purpose the **Optimizer** class is defined. Currently, an optimization based on an adaptive quad-tree method is implemented.

A number of classes in the figures presented above have not yet been discussed. Most of these are used only internally in the simulation code. These classes are discussed in the next section.

### 3.3 Supportive classes

The **Integral** class, shown in figure 3.4, is used to calculate the classical collision integrals as discussed in chapter 2. Since two numerical methods are provided to evaluate these integrals, this class is an abstract class, which only handles the conversion from center-of-mass energy,  $\epsilon$ , and impact parameter,  $s$ , to the scaled energy and impact parameter and visa versa.

The **Integration** class evaluates the collision integrals using the adaptive numerical integration routine QAGS from ref. [6]. This method is implemented in the

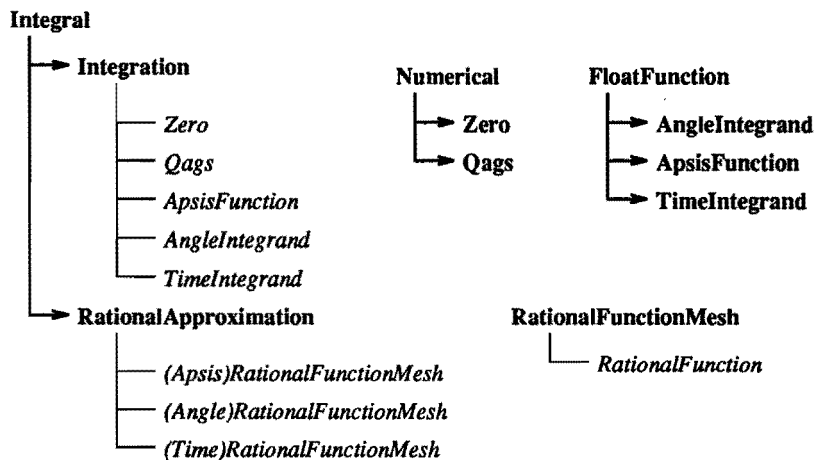


Figure 3.4: The classes implementing the numerical procedures required by the simulation code. The **Integral** class provides an interface for the implementation of the **Integration** and **RationalApproximation** classes.

**Qags** class. The distance of closest approach,  $R_0$ , is calculated with a root-finding algorithm by Bus and Dekker [7], which is implemented in the **Zero** class. The remaining three classes evaluate the integrands of the classical collision integrals and the function used to determine the distance of closest approach (i.e., the apsis).

A much faster method to evaluate the collision integrals is provided by a numerical approximation based on rational functions. This method is implemented in the **RationalApproximation** class and follows the numerical procedure discussed in chapter 4.

In many parts of the code lists and trees of a certain class are needed. An object-oriented programming language provides the possibility to implement such lists and trees in a manner, that does not require the type of the class to be known. In figure 3.5 these classes are shown. While the **List** class supports only insertion and deletion of an element, the **ListIterator** class provides the possibility to go through a list without affecting its elements. Using a separate iterator class also offers the advantage that several iterations can be done on the same list at the same time.

Up to here, we have concentrated on the structure of the simulation code. As an illustration of its use, three applications, that extend its functionality, will be discussed in the next section.

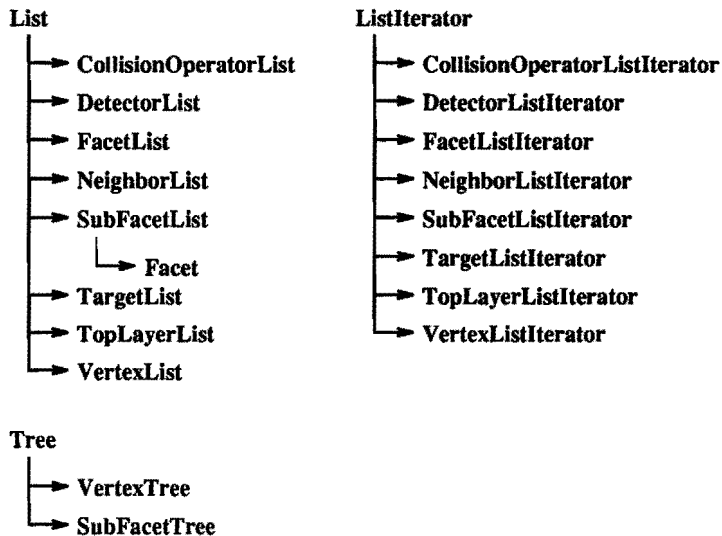


Figure 3.5: The `List`, `ListIterator`, and `Tree` classes are generic classes from which several specific classes are derived. Most of these are used only internally.

### 3.4 Three sample applications

For studying charge-exchange processes (see chapter 7) and the tails at the low-energy side of surface peaks in ion-scattering spectra (see chapter 8), three applications were developed.

The first application is used to collect information related to charge-exchange processes and to store this information in a file for later processing. The structure of this application is shown schematically in figure 3.6. The application consists of an ion source, a class collecting the information needed, and a detector, that writes the information to a file when the ion is detected. Two types of ion sources are available: an idealized and a realistic ion source. Both are implemented using the same classes, but they are derived from two different ion-source classes. The `Extension` and `ExtensionID` classes are used to attach additional data to the `Ion` class in a manner, that is transparent to the main code and allows more than one application to be used simultaneously. The `Ion` class stores the ion as generated by the ion source. Information on each collision in the cascade, is stored in the `NeutralizationDataList` class. This information is collected by the `NeutralizationFit` class. The `ExtensionID` class is used to retrieve the `NeutralizationDataList` class from the `Extension`, which is attached to the `Ion` class by the ion source. At

the end of a cascade calculation the **NeutralizationFitDetector** class is used to store the information. A **Detector** is used to check if the ion is actually detected. If this is the case the **NeutralizationFitDetector** class writes the information on the initial ion and the cascade to a file. Deriving the **NeutralizationFitDetector** class directly from the **Detector** class and using a separate **Detector** class offers the advantage, that the application does not depend on a specific detector type, which would have been the case if the **NeutralizationFitDetector** was derived from one of the detectors.

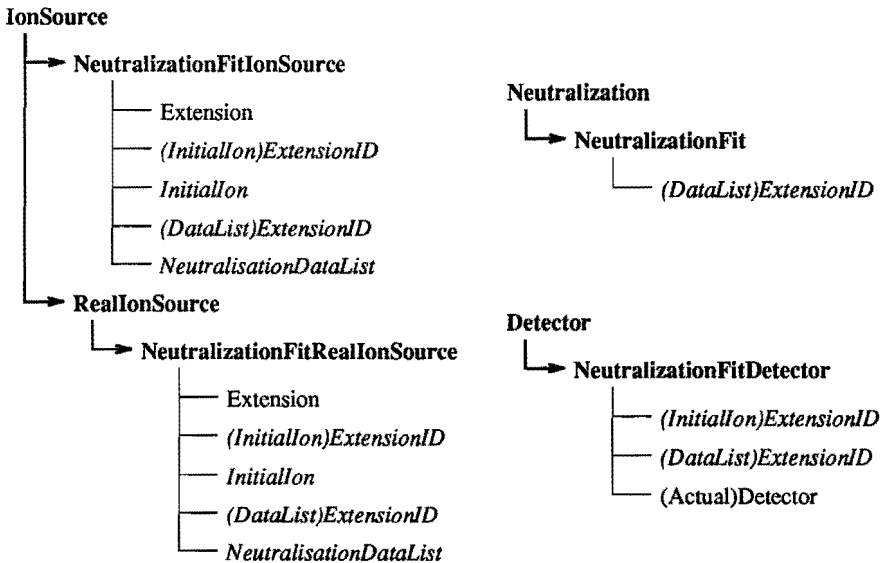


Figure 3.6: A schematic representation of the classes involved in the charge-exchange application. The application can be divided in three parts: an ion source, an class collecting the information needed, and a detector that writes the information to a file when the ion is detected.

Both other applications were developed to study the tails at the low-energy side of surface peaks in ion-scattering spectra. These applications have a structure similar to that of the charge-exchange application (see figure 3.7). One application is used to store the position where the ion hits the surface, the maximum depth reached by the ion, the energy loss of the ion at this depth, the total energy loss when the ion is detected, and the direction of the final trajectory of the ion. This application is formed by the **DepthData**, **DepthProfileIonSource**, **DepthProfileOperator**, and **DepthProfileDetector** classes.

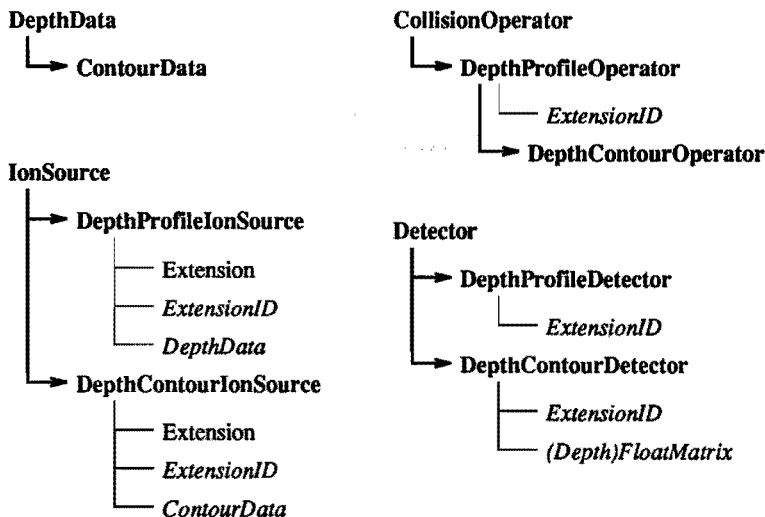


Figure 3.7: A schematic representation of the classes involved in the applications for studying the tails in ion-scattering spectra. Both applications have a structure similar to the one shown in figure 3.6.

The other application stores the maximum depth reached by the ions, which are generated on an equidistant mesh. Its structure is similar to the application discussed above and contains the **ContourData**, **DepthContourIonSource**, **DepthContourOperator**, and **DepthContourDetector** classes. The last class stores the maximum depths in a matrix, which can be stored in a file at the end of the simulation. Since part of this application is identical to the depth-profile application discussed previously, some of its classes were derived from classes from the depth-profile application.

## References

- [1] B. Stroustrup, *The C++ programming language*, 2-nd ed., Addison-Wesley, 1991, ISBN 0-201-53992-6
- [2] P.A.J. Ackermans, P.H.F.M. van der Meulen, H. Ottevanger, F.E. van Straten, H.H. Brongersma, Nucl. Instr. Meth. B35 (1988) 541

- [3] O.B. Firsov, *Sov. Phys. JETP* 6 (1958) 534
- [4] O.S. Oen, M.T. Robinson, *Nucl. Instr. and Meth.* 132 (1976) 647
- [5] A. Richard, H. Eschenbacher, *Nucl. Instr. Meth.* **B2** (1984) 444
- [6] R. Piessens, E. de Doncker-Kapenga, C. Ueberhuber, D. Kahaner, *QUADPACK, a subroutine package for automatic integration*, Springer Series in Computational Mathematics, Springer-Verlag, Berlin, 1983
- [7] J.C.P. Bus, T.J. Dekker, *ACM Trans. Math. Soft.*, 1 (1975) 330

# Chapter 4

## Differential correction algorithm for a function of two continuous variables: application to the collision integrals<sup>1</sup>

### Abstract

The differential correction algorithm is a well-known algorithm for finding a rational approximating function to a function of one discrete or continuous variable. In this work we present a modification of the differential correction algorithm using (quasi-random) Korobov points in order to apply it to functions of two continuous variables. The algorithm is applied to the low-energy ion-scattering (LEIS) collision integrals. The approximation obtained is more accurate and about one order of magnitude faster than other approximations in literature.

### 4.1 Introduction

Simulation is an important tool for the interpretation of low-energy ion-scattering (LEIS) spectra. In ion-scattering simulation, a good approximation of the interaction of the ion with the surface atoms is a sequence of classical two-particle collisions [1]. An important part of ion-scattering simulation is the evaluation of the collision integrals: the scattering angle  $\theta$  and the time integral  $\tau$ . Except for a few simple interaction potentials these integrals cannot be solved analytically.

---

<sup>1</sup>The contents of this chapter has been published in: C.A. Severijns, G. Verbist, H.H. Brongersma, and J.T. Devreese, *Comp. Phys. Comm.* 70 (1992) 459. Preliminary results have been published in: C.A. Severijns, G. Verbist, H.H. Brongersma, and J.T. Devreese, *Nucl. Instr. Meth. B64* (1992) 730



In general, ion scattering is simulated using the Monte Carlo method. To obtain statistically reliable results one has to calculate a large number of ion tracks (typically  $10^6$ ). In order to reduce the computing time, efficiency considerations are crucial. However, one also needs a high accuracy to obtain reliable results when determining the structure of a surface. Therefore, one has been looking for methods to calculate the collision integrals efficiently and accurately [1–3]. These methods are either accurate but computing time consuming, or fast but less accurate. An accurate and efficient approximation of the collision integrals can be obtained by using an approximation based on rational functions [4].

In this work we will present a method of calculating the rational function approximation of a function of two variables based on the differential correction algorithm. In the next section we will discuss the differential correction algorithm for functions of one variable and, thereafter, the modifications needed to apply this algorithm to functions of two variables. Finally, we will apply this method to calculate an approximation of the collision integrals.

## 4.2 The differential correction algorithm

The differential correction algorithm was developed for approximating a real-valued function  $f$  on a discrete point set  $X = \{x_1, x_2, \dots, x_N\}$  by a rational function (see Barrodale *et al.*, [5])

$$R(x) = P(x)/Q(x) = \frac{\sum_{i=0}^m p_i x^i}{\sum_{j=0}^n q_j x^j} \quad (4.1)$$

for given integer values of  $m$  and  $n$ . The optimal coefficients  $p_i$  and  $q_j$  will minimize the maximum error given by

$$\max_{1 \leq t \leq N} |f(x_t) - R(x_t)| = \|f - R\|_\infty \quad (4.2)$$

subject to the condition

$$Q(x_t) > 0, \quad t = 1, 2, \dots, N. \quad (4.3)$$

This last condition prevents the occurrence of poles in the approximation.

The differential correction algorithm uses an iterative scheme that minimizes — at the  $k$ -th stage— the maximum error  $\Delta_k$  of the current approximation  $R_k(x) = P_k(x)/Q_k(x)$ . Here  $\Delta_k$  is given by

$$\Delta_k = \max_t |f(x_t) - P_k(x_t)/Q_k(x_t)|, \quad (4.4)$$

and converges quadratically to the minimax error

$$\Delta^* = \inf_{P, Q} \max_t |f(x_t) - P(x_t)/Q(x_t)|. \quad (4.5)$$

From the  $k$ -th approximation,  $R_k(x)$ , the next approximation,  $R_{k+1}(x)$ , can be calculated by minimizing

$$\max_t \{|f(x_t)Q(x_t) - P(x_t)| - \Delta_k Q(x_t)\}. \quad (4.6)$$

The minimization of (4.6) yields a linear programming problem. Unless one finds  $P_k(x)$  and  $Q_k(x)$  such that  $\Delta_k = \Delta^*$ , the coefficients  $q_j$  can be negative. Technically, condition (4.3) is implemented as [5]

$$|q_j| \leq 1, \quad j = 0, 1, \dots, n \quad (4.7)$$

for  $x \in [0, 1]$ . The *linear* conditions (4.7) can be added to the linear programming problem (4.6).

Although the differential correction algorithm solves the approximation problem on a discrete point set it can be modified to approximate a real-valued function on an interval [6,7]. This is done by using the points of alternating extrema in the error of the current approximation as the set of points  $X$  to calculate the next approximation.

### 4.3 Modifications for functions of two variables

The differential correction algorithm can also be applied to rational approximating functions of a more general nature than the ratio of two polynomials. It can without modification be applied to calculate the approximation of functions of two or more variables on a *discrete* point set. For the present purpose, we need to approximate a function of two variables on a rectangular area. This requires the determination of the extrema of the error in the approximation. Finding the extrema of a function of two variables, however, is a non-trivial problem, because the set of extrema is not necessarily a finite set of points in two-dimensional space. Therefore, the algorithm was modified as follows: instead of the rectangular area we use a large set  $Y$  of sample points typically containing  $10^3$  points. The points of this set  $Y$  were calculated using a Korobov point generator [8] in order to obtain a homogeneous distribution of sample points. From the set  $Y$ , the global minimum and maximum are determined in each iteration step. These extrema are used to update the reference set  $X_{k-1}$  to  $X_k$ . In this manner the initial point set  $X_0$  is adapted during the process of iteration in order to get more points where the largest errors in the approximation occur. One problem with this algorithm remains: when the error  $\Delta_k$  approaches  $\Delta^*$  the value of  $\Delta_k$  starts to oscillate. This is due to the fact that a discrete set of points is used. Therefore, it is possible that, when the extremal error not only constitutes a single point but a curve, the error increases in one part of this curve while it is reduced in another part upon iteration. This problem is inherent to the differential correction algorithm when using it to approximate a function of two or

more continuous variables, and it makes the detection of convergence difficult when  $\Delta_k$  approaches  $\Delta^*$ . Thus, we applied an upper limit on the *absolute* value of  $\Delta_k$  instead of the original upper limit on its *relative* change.

#### 4.4 Physical problem: the LEIS collision integrals

When an ion hits a surface it will interact with the atoms of this surface. The trajectory of the ion through the surface can be approximated by the asymptotes of the initial and final trajectories in a sequence of classical binary collisions [1]. These asymptotes can be calculated for an ion with initial energy  $E_i$  and impact parameter  $s$  from the scattering angle  $\Theta$  and the distance  $\Delta$  (see figure 4.1). Both quantities can be derived from the two collision integrals: the scattering angle in the center-of-mass system

$$\theta = \pi - 2s \int_{R_0}^{\infty} \frac{dr}{r^2 f(r)} \quad (4.8)$$

and the time integral

$$\tau = \sqrt{R_0^2 - s^2} - \int_{R_0}^{\infty} \left( \frac{1}{f(r)} - \frac{1}{\sqrt{1 - \left(\frac{s}{r}\right)^2}} \right) dr \quad (4.9)$$

where  $f(r)$  is given by

$$f(r) = \sqrt{1 - \left(\frac{s}{r}\right)^2 - \frac{V(r)}{E}} \quad (4.10)$$

and the energy of the ion in the center-of-mass system is

$$E = \frac{m_{atom}}{m_{atom} + m_{ion}} E_i \quad (4.11)$$

The distance of closest approach  $R_0$  is determined from  $f(R_0) = 0$ .

The scattering angle  $\theta$  has two discontinuities. This can be shown by considering the boundaries of the energy and the impact parameter. For  $s = 0$  one has a head-on collision and in this case  $\theta = \pi$ . In the limit  $s \rightarrow \infty$  the projectile is a free particle so that  $\theta = 0$ . When  $E \rightarrow 0$  the projectile is reflected for any impact parameter, thus  $\theta = \pi$ . Finally, for  $E \rightarrow \infty$  the projectile is a free particle for any  $s > 0$ . Using these boundary values, one finds the following limits in the case  $(E, s) \rightarrow (0, \infty)$

$$\lim_{s \rightarrow \infty} \lim_{E \rightarrow 0} \theta(E, s) = 0, \quad (4.12)$$

$$\lim_{E \rightarrow 0} \lim_{s \rightarrow \infty} \theta(E, s) = \pi. \quad (4.13)$$

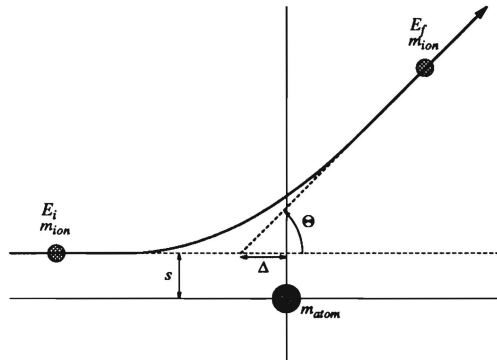


Figure 4.1: The collision of an ion with a surface atom.

Similarly one finds for  $(E, s) \rightarrow (\infty, 0)$

$$\lim_{E \rightarrow \infty} \lim_{s \rightarrow 0} \theta(E, s) = 0, \quad (4.14)$$

$$\lim_{s \rightarrow 0} \lim_{E \rightarrow \infty} \theta(E, s) = \pi. \quad (4.15)$$

These discontinuities make it difficult to find a good approximation for the scattering angle in the neighbourhood of these limiting cases.

To determine the interaction potential  $V(r)$ , one generally uses the Thomas-Fermi atom model [9] in which one universal expression describes the interaction potential between any ion and atom [10]. This is achieved by scaling the initial energy and the impact parameter

$$s^* = s/a_F \quad (4.16)$$

$$E^* = E/c_F \quad (4.17)$$

where  $a_F$  and  $c_F$  contain all dependencies on the ion and the target atom. (Because, in the remainder of this paper we are only considering the scaled energy  $E^*$  and impact parameter  $s^*$ , we will leave out the  $*$ .) The Molière potential [11] is an analytical approximation of the Thomas-Fermi potential, which is well-suited for LEIS.

## 4.5 Results and discussion

An approximation of the collision integrals for the Molière potential was obtained using the differential correction algorithm with the above mentioned modifications.

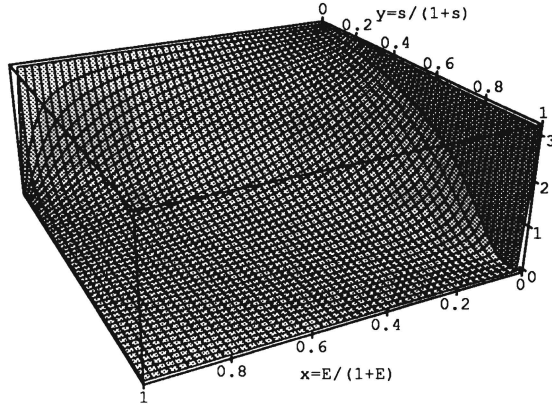
**Theta (x, y)**

Figure 4.2: The scattering angle  $\theta$  as a function of the transformed coordinates  $x$  and  $y$ . Note the discontinuities in the corners  $(1, 0)$  and  $(0, 1)$ .

As both  $E$  and  $s$  can take any positive value, it is useful to apply a transformation to map them on a finite interval, e.g. by

$$(x, y) = \left( \frac{E}{1+E}, \frac{s}{1+s} \right). \quad (4.18)$$

This transformation has the advantage that it only requires primitive operations (additions and divisions) and it does not contribute significantly to the total computing time of the approximation. Because the time integral  $\tau(x, y)$  diverges for  $x \rightarrow 0$ , we use an analogously transformed function  $f_\tau(x, y)$  defined as

$$f_\tau(x, y) = \frac{\tau(x, y)}{1 + \tau(x, y)} \quad (4.19)$$

and we approximate this function instead of  $\tau$ . The functions that are obtained by applying these transformations, are shown in figures 4.2 and 4.3.

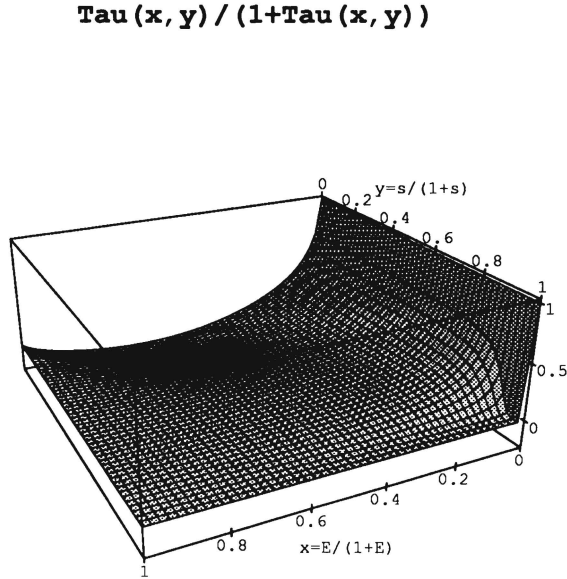


Figure 4.3: The transformed time integral  $f_\tau$  as a function of the transformed coordinates  $x$  and  $y$ . Note the discontinuity in the corner  $(0, 1)$ .

As the approximating rational function the ratio of two fourth-degree polynomials was chosen

$$R(x, y) = P(x, y)/Q(x, y) = \sum_{i=0}^4 \sum_{j=0}^{4-i} p_{ij} x^i y^j / \sum_{k=0}^4 \sum_{l=0}^{4-k} q_{kl} x^k y^l. \quad (4.20)$$

In order to obtain sufficient accuracy, the unit square was divided by an equally spaced  $8 \times 8$  mesh as shown in figure 4.4. In this figure the absolute error in the approximation is given for each sub-square. The shaded areas must be treated separately in order to get a good accuracy.

For the scattering angle  $\theta(x, y)$ , the light gray sub-square at the lower right corner in figure 4.4 has a discontinuity for  $(x, y) = (1, 0)$  (see equations (4.14) and (4.15)). In case of the Molière potential the behaviour of the scattering angle  $\theta$  in this area resembles that of the scattering angle  $\theta_C$  for the Coulomb potential, which can be

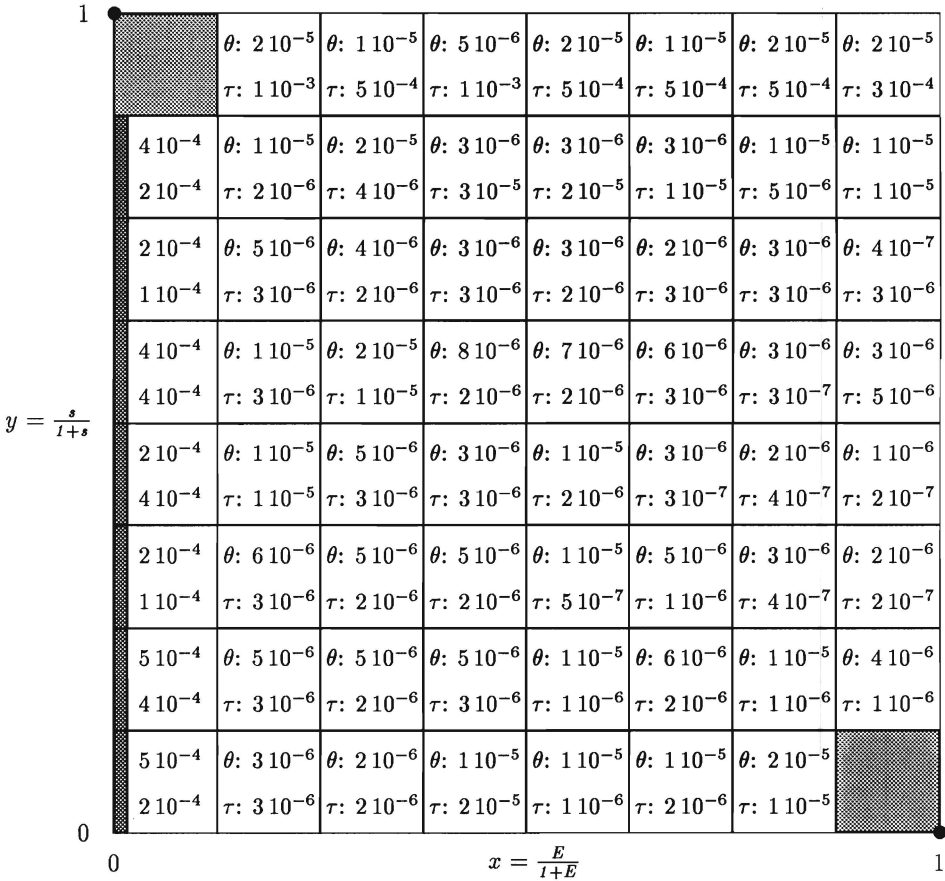


Figure 4.4: The  $8 \times 8$  mesh used to subdivide the unit square. The absolute error in the approximation of both collision integrals is given for each sub-square. The shading indicates the areas where the behaviour of the collision integrals was too bad to get a good approximation without the use of an extra coordinate transformation. The positions of the discontinuities are indicated by the black dots.

obtained analytically

$$\theta_C(E, s) = 2 \arctan\left(\frac{1}{2Es}\right). \quad (4.21)$$

The limiting value for  $(x, y) \rightarrow (1, 0)$  depends only on the first directional derivative along the path used to approach  $(1, 0)$ . Using, e.g., a straight line  $y = a(1 - x)$  one finds

$$\lim_{x \rightarrow 1} \theta_C(x, y) = 2 \arctan\left(\frac{1}{2a}\right). \quad (4.22)$$

Therefore, a transformation of the coordinates  $(x, y)$  to polar coordinates (with the origin  $(1, 0)$ ) was applied successfully to this area with a maximum error of  $5 \times 10^{-4}$  for  $\theta$ . (The time integral  $\tau$  does not present any problems on this area.)

The sub-squares at the left hand side of figure 4.4 can not be approximated with the same accuracy unless a strip with  $x \leq \frac{1}{60}$  is excluded. This problem seems to be related to a divergence of the first derivative for  $x \rightarrow 0$ . This is reminiscent of the logarithmic function. Therefore, a transformation

$$x^* = \frac{\log x}{\log \frac{1}{60} + \log x} \quad (4.23)$$

is applied for  $x < \frac{1}{60}$  to both collision integrals,  $\theta$  and  $\tau$ , and a maximum error of  $5 \times 10^{-4}$  is obtained here. (For the upper half of the strip, fifth-degree instead of fourth-degree polynomials in equation (4.20) were needed to approximate  $\theta(x^*, y)$  with this accuracy.)

The discontinuity in the upper left sub-square for  $(x, y) = (0, 1)$  can not be removed by using a transformation to polar coordinates. It appears that in the case of the Molière potential, due to the screening function, the scattering angle  $\theta(x, y)$  and the time integral  $\tau(x, y)$  behave very non-linearly in this sub-square. The part with  $x \geq \frac{1}{60}$  of this sub-square could be approximated with sufficient accuracy using a fourth degree rational function and the lower half ( $y \leq \frac{15}{16}$ ) of the dark gray part with a fifth degree rational function. The remaining part of this sub-square with  $x < \frac{1}{60}$  and  $y > \frac{15}{16}$  can not be approximated with the same accuracy using a low-degree rational function, because of the extremely bad behaviour of both collision integrals in this area. Fortunately, this area is not of great importance for LEIS simulations as is illustrated in figure 4.5, because this area corresponds to impact parameters that are greater than interatomic distances.

In literature, different approaches are used to calculate the scattering angle  $\theta$ . These approaches are compared to the rational function approximation presented in this work in table 4.1. A straightforward method of calculating the scattering angle  $\theta$  is numerical integration. In this respect, we mention the MARLOWE-code [1] where a Gauss-Mehler quadrature is used, after a Newton-Raphson search for  $R_0$ . Alternatively, approximate *analytical* formulae can be used as was done in the TRIM-code [2], where an ingenious correction to the Rutherford formula for Coulomb scattering is made. This approximation is accurate for small scattering angles  $\theta$



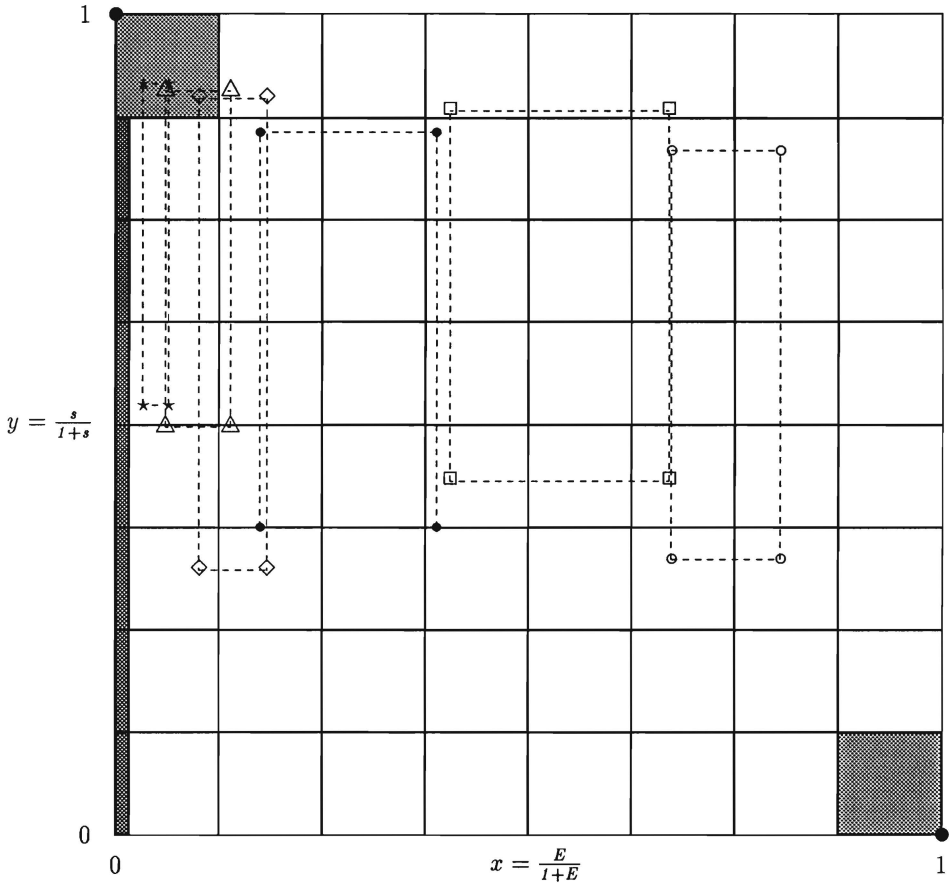


Figure 4.5: The positions of a number of typical combinations of ions and target atoms in LEIS. The lower values of  $y$  correspond with an impact parameter of  $0.1 \text{ \AA}$  and the upper values with an impact parameter of  $1 \text{ \AA}$ . The following ion and target atom combinations are plotted: 1 and 3 keV  $\text{He}^+$  with B (o), Na (●), Ni (□) and, W (△) and 4 and 8 keV  $\text{Ne}^+$  with Ni (◇) and W (★).

since it refers to the Coulomb problem. But it still requires a root-finding procedure for  $R_0$ . Finally, a direct *numerical* approximation using spline interpolation was proposed by Scanlon *et al.* [3].

Approximation	Typical acc.	Operation count	Evaluations ( $s^{-1}$ )	Range
MARLOWE	$\leq 0.1\%$	root finding 32 potentials	160 / 1.8	unlimited
TRIM	$\approx 1\%$	root finding 1 potential 1 derivative	790 / 7.5	small scattering angles
Splines	$\approx 1\%$	2 log() 2 binary searches 123 arithmetic	- / -	$[10^{-3}; 10] \times$ $[10^{-3}; 10]$
Rational fit	$\leq 0.1\%$	44 arithmetic	5900 / 60	unlimited

Table 4.1: The rational function approximation of the scattering angle  $\theta$  compared with the literature. The timing information was obtained on two computer systems: the first number was obtained on a HP 9000/370 and the second number on a HP Vectra (80286, 8 MHz, *no* co-processor). For the spline interpolation, this information could not be obtained, because the code was not available to the authors.

## 4.6 Conclusions

The differential correction algorithm with the modifications for approximating a function of two continuous variables can be used to obtain an accurate and efficient numerical approximation. It is successfully applied to the LEIS collision integrals for the whole range of energy and impact parameters that are important in LEIS.

## References

- [1] M.T. Robinson, I.M. Torrens, Phys. Rev. B **9** (1974) 5008
- [2] J.P. Biersack, L.G. Haggmark, Nucl. Instr. Meth. **174** (1980) 257
- [3] P.J. Scanlon, P.M. Boucher, B. Castel, Nucl. Instr. Meth. B **16** (1986) 301
- [4] C.A. Severijns, G. Verbist, H.H. Brongersma, T.J. Devreese, Nucl. Instr. Meth. B **64** (1992) 730

- [5] I. Barrodale, M.J.D. Powell, and F.D.K. Roberts, *SIAM J. Numer. Anal.* 9 (1972) 493
- [6] D. Belogus and N. Liron, *Numer. Math.* 31 (1978) 17
- [7] E.H. Kaufman, D.J. Leeming, and G.D. Taylor, *Math. of Comp.* 32 (1978) 233
- [8] K. Zakrzewska, J. Dudek, N. Nazarewicz, *Comp. Phys. Comm.* 14 (1987) 299
- [9] I.M. Torrens, *Inter-atomic potentials*, Academic Press, London 1972
- [10] O.B. Firsov, *Sov. Phys. JETP* 6 (1958) 534
- [11] G. Molière, *Z. Naturforsch.* 2a (1947) 133

# Chapter 5

## The SISS-92 computer code for the simulation of ion-surface scattering<sup>1</sup>

### Abstract

A new and efficient computer code for the simulation of ion scattering experiments is presented. Results of simulations with this code are compared to experimental data as well as existing simulation results from the literature. Within a simulation, it is possible to investigate separately the influence of thermal vibrations and the divergence of the primary ion beam. It is shown, that the broadening of the peaks in an angular-dependent intensity profile is mostly due to imperfections in the ion source and detector.

### 5.1 Introduction

Low-energy ion scattering (LEIS) is a suitable technique for surface analysis [1,2]. It can be used to determine not only the composition, but also the structure of the outermost layers of atoms. Because the interaction of ions with the atoms in the surface is in many respects a complicated process, simulation is often used as a tool for interpreting results from ion scattering experiments. A well-known computer code for the simulation of ion scattering is MARLOWE [3]. This code was initially developed for ion implantation purposes, which require the implementation of atomic-displacement cascades. This results in a considerable overhead in computer time for the simulation of light ion scattering [4] and makes this code less suited for this purpose. Therefore, other computer codes were developed such as ARGUS [5], EDI [6] and TAVERN [7]. However, these programs are still computer-time intensive and each has its disadvantages. In the case of ARGUS, the collision

---

<sup>1</sup>The contents of this chapter is accepted for publication in Surf. Sci..

integrals are evaluated using a complicated combination of numerical and analytical approximations and in EDI numerical integration is applied. Furthermore, the time integral is neglected in both EDI and TAVERN. TAVERN also uses an expensive method for finding collision partners. For the specific case of impact-collision ion-scattering spectroscopy (ICISS) [2] a much more efficient method of simulation can be applied, the reason being that the interaction of the ion with the surface atoms is restricted to a single backscattering event and one or two grazing angle collisions by the experimental conditions [8]. In this case a semi-analytical solution can be obtained for the ion trajectories [8]. This code is fast but application specific. For medium-energy ion scattering (MEIS), an efficient simulation method can be used based on the nuclear encounter concept [9]. This method cannot be applied to LEIS simulation, because for low-energy ions the width of the shadow cones is comparable to the inter-atomic distances. The simulation of the scattering of ions with an energy between 10 and 100 eV requires a more elaborate physical model [10]. As a result, a simulation code for ion scattering in this energy range has a large overhead compared to simulation codes for ion scattering at higher energies.

Here, we present a new, fully three-dimensional simulation code for ion scattering called SISS-92 (Simulation of Ion-Surface Scattering 1992). The paper is organised as follows: in section 5.2 we will discuss the physical model implemented in the code, the algorithms used and the structure of the code. In section 5.3 we present simulation results obtained with the code and compare these with experimental data and existing results of simulation from the literature. Finally, in section 5.4 the conclusions of this work are summarized.

## 5.2 The simulation code

A generally accepted model describing the interaction of an ion with the atoms in the surface, is the classical single binary collision (SBC) approximation (see e.g. [3–5]). The SISS-92 code is based on this model also. The Molière approximation to the Thomas-Fermi potential is used for the interaction potential between the ion and the target atom [11]. Inelastic energy loss can be taken into account using either the model by Firsov [12] or the model by Oen-Robinson [13]. Finally, uncorrelated thermal vibrations have been implemented. Because the characteristic thermal-vibration periods of the atoms in solids are much larger than the interaction time between the ion and the surface [3], this is done by randomly changing the position of the atoms around their equilibrium positions. For this purpose, an anisotropic distribution function can be specified for each individual atom.

In order to obtain statistically significant results a large number (typically  $10^6$ ) of ion trajectories has to be calculated. Therefore, the efficiency of the code is of great interest. When using the SBC-model, two problems have to be solved: for each

collision the classical collision integrals (i.e. the angle and time integral) have to be calculated, and after each collision a new target atom has to be found. Because these are the main operations, a large amount of computer time can be saved by implementing them efficiently. In the SISS-92 code, the classical collision integrals are calculated using a fast numerical approximation based on rational functions which is more accurate than the method used in the ARGUS code [14].

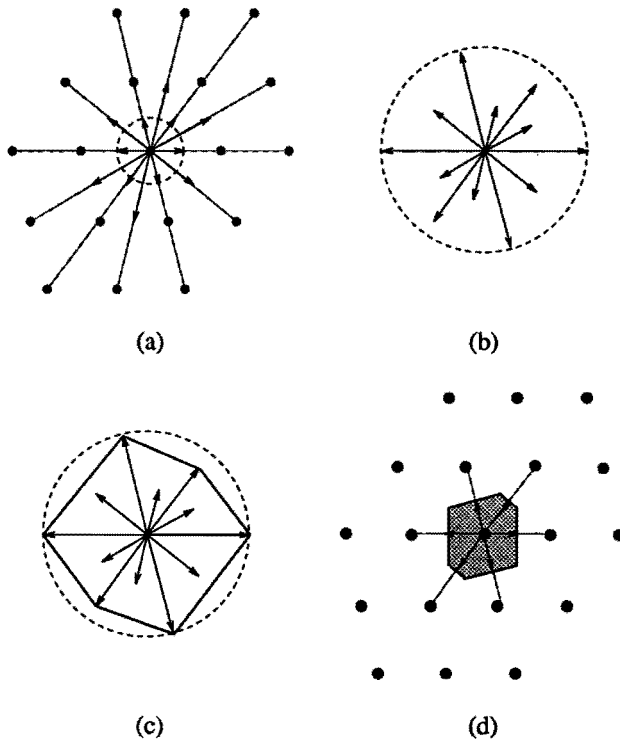


Figure 5.1: The calculation of a cell for a selected atom. For ease of illustration a two-dimensional lattice is used. Figure (a) shows a part of the lattice in normal space including the vectors from the central atom halfway to the other atoms. Figure (b) shows these vectors after the transformation to the dual space. In figure (c) the convex hull of these vectors is shown. Finally, figure (d) shows the cell (the shaded area) after transforming the convex hull to normal space. In figures (a) to (c), the unit circle is also shown.

A new target can be found using a searching algorithm such as the one by Landuijt *et al.* [15], which we will briefly describe here. The surface is divided into cells with in each cell exactly one atom. Such a cell is a convex polyhedron with its facets positioned halfway the nearest neighbor atoms. Thus, the lattice is divided into

a Wigner-Seitz-like structure. Positioning the facets halfway the neighbor atoms is reasonable, even for a lattice consisting of different types of atoms, because the scattering angles are small at these distances. E.g., for a 4 keV  $\text{Ne}^+$  ion scattering from a Ni atom at an impact parameter of 1.5 Å one finds a scattering angle of 0.7°. After colliding with a target atom, the next target is determined by intersecting the final ion trajectory with the cell. The facet that is intersected, determines the next target atom. Besides its efficiency, this method also has the advantage that large, periodic surfaces can be stored in little memory. Our implementation uses algorithms from computational geometry for calculating the data needed in the searching process, as follows: first, the vectors halfway to the positions of all atoms relative to a selected atom are calculated (see figure 5.1a). Then, these vectors (in normal space) are transformed into a corresponding set of vectors in dual space (figure 5.1b). The convex hull of this point set can be determined with the “gift-wrapping” algorithm (figure 5.1c). Transformation of this convex hull back into normal space, gives the cell for the selected atom (figure 5.1d). The algorithms and transformations referred to here have been explained in detail by, e.g., Preparata and Shamos [16].

The efficiency of the simulations is further improved by applying the quasi-Monte Carlo method, which has a higher order of convergence compared to the normal Monte Carlo method [17,18]. In our code we used a point generator based on Halton’s sequence [19]. An efficient implementation of such a generator is given by Berblinger and Schlier [20]. Optionally, an adaptive optimization strategy based on a quad-tree can be applied to further improve the performance, as follows: initially, the surface area of interest is divided into a rectangular grid and for each rectangle of this grid a number of ions to pass and a minimum number of ions that has to be detected, is given. When the given number of ions has passed a rectangle, the number of ions that was detected is compared to the minimum number required. If more ions were detected than required, the rectangle is subdivided into four equal rectangles. Otherwise, the ions hitting the surface in this rectangle will be discarded in the remainder of the simulation.

An important aspect of any simulation code is its flexibility. In the SISS-92 code, this was realized by using object-oriented design and programming techniques. This approach offers several advantages. Firstly, it makes the reuse of existing code easy resulting in a reduction of the time needed to develop and add new features. Secondly, the *implementation* of an object and its *interface* are strictly separated. Therefore, the code implementing an object can be modified freely, because the remainder of the code only knows the interface. This appeared to be especially useful for implementing the various models for inelastic energy loss and charge exchange.

Very useful is the derivation mechanism provided by an object-oriented programming language. This mechanism allows one to extend the capabilities of existing objects without having to adapt the main simulation code. As an illustration, con-

sider the ion source object. Initially, only one type was implemented: an idealised ion source, which generates a mono-energetic ion beam without an angular spread. However, for certain applications a more realistic ion source, e.g. one that generates an ion beam with a normal distribution in both the energy and the angles, is better suited. Noting, that such an ion source is in fact an idealised ion source with some extra properties, it was implemented by adding these properties to the idealised ion source.

The object-oriented approach also offers an advantage concerning the structure of the code. This is illustrated in figure 5.2, where the structure of the code is compared to a typical set-up for a LEIS experiment. Both the code and the experiment have a similar structure. The main parts are the ion source, the surface, the cascade, and the detector. We will discuss the structure of the code in some detail now.

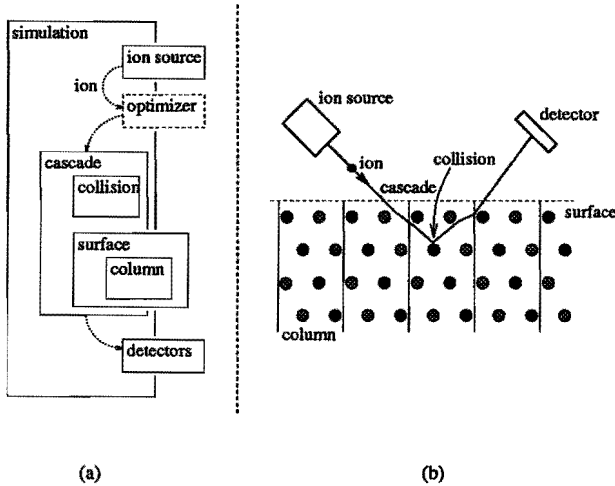


Figure 5.2: The structure of the simulation code compared with a typical LEIS experiment. Indicated in the figure are the main parts: the ion source, the surface, which is constructed by repeating a single column, the cascade, which is a sequence of binary collisions in the current version of the code, and the detector.

The main part of the code is the simulation object, which task it is to calculate a number of cascades as follows: first an ion is generated by the ion source. If optimization is enabled, this ion is passed to the optimizer, which returns a value indicating if the ion might reach the detector or not. In the latter case, a new ion is requested from the ion source repeatedly until the optimizer indicates that the ion might reach the detector. Then, a cascade is calculated for the ion, which requires calculating single binary collisions. In the current version recoil particles are not



taken into account but the code has been prepared for its implementation. Therefore, in the following, we will use “cascade” to indicate both a collision sequence and a cascade. The surface is used to find the target atoms that interact with the ion. The calculation of a cascade is aborted when either one of the following conditions is satisfied: (1) the ion exits the surface either to the vacuum or the bulk, (2) the energy of the ion gets below a given minimum value, or (3) a given maximum number of collisions is reached. The latter condition ensures that the simulation will take a finite amount of computer time. When the ion exits the surface to the vacuum, it is passed to a set of detectors. Using a set of detectors gives the possibility to simulate more than one experiment in a single run of the code. When the ion exits the surface to the bulk, it can optionally be passed to a set of detectors. This is useful, e.g. when studying the transport of ions through the bulk. Both sets of detectors return a value indicating if the ion was detected by any of them. If optimization is enabled, this information is passed to the optimizer, where it can be used to improve the efficiency.

Five of the objects shown in figure 5.2 can be controlled from outside the simulation code: the ion source, the detectors, the surface, the simulation, and the optimizer. With these objects, every LEIS experiment can be simulated: the ion source, the detectors, and the surface define the experimental set-up. Physical aspects of the collision process, such as inelastic energy loss, can be taken into account by passing a corresponding object to the simulation object. The remaining three objects are for internal use by other objects only: (1) the cascade object, which is needed by the simulation object to calculate a cascade, (2) the collision object, which is needed by the cascade object to calculate a single binary collision, and (3) the column object, which is used by the surface object to build the surface. This is indicated in figure 5.2 by completely enclosing these by the other object.

### 5.3 Comparison with experiments

Using the SISS-92 code, the measurements of Buck *et al.* [21], who used the time-of-flight technique to determine the combined energy spectrum of the ions and the neutrals of  $E_0 = 2.4$  keV  $\text{Ne}^+$  ions scattering from the (100) surface of a nickel single crystal, were simulated. In these measurements the ion beam was directed along the  $\langle 110 \rangle$  direction and both the ion beam and the detector were positioned at an angle of  $45^\circ$  with the surface, resulting in a total scattering angle of  $90^\circ$ . In figure 5.3a the experimental spectrum is shown. For the simulation, a realistic ion source was used with an angular spread of about  $2^\circ$  and an energy spread of 20 eV. The detector was implemented according to the one used in the experiment. The effects of both inelastic energy loss and thermal vibrations were neglected. The data on the Ni(100) surface by Frenken *et al.* [23,22] were used here. The surface was taken 8 atomic

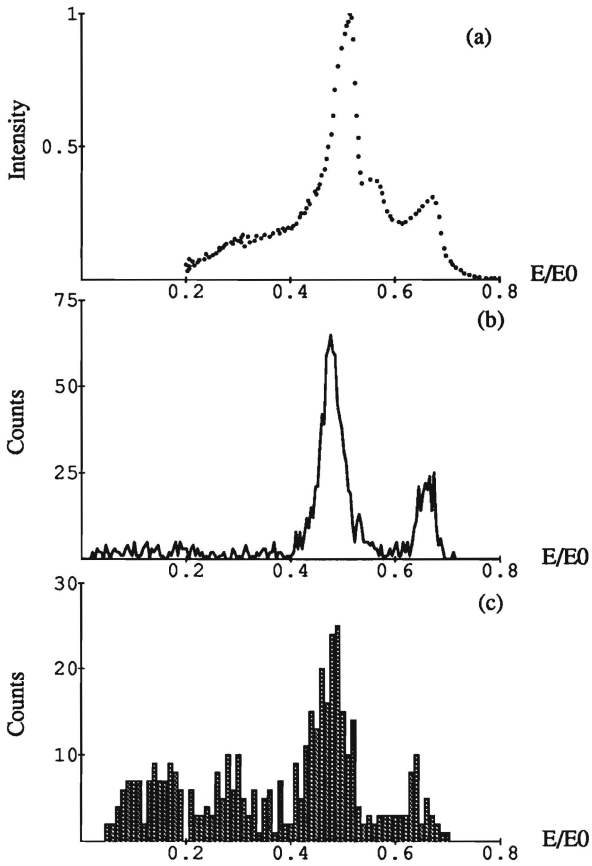


Figure 5.3: In figure (a) the experimental spectrum by Buck *et al.* [21] of 2.4 keV ionic and neutral neon scattering from the Ni(100) surface in the  $\langle 110 \rangle$  direction at a scattering angle of  $90^\circ$  is shown. The result of a simulation of this spectrum with the SISS-92 code is shown in figure (b). For comparison, the simulated spectrum by Helbig *et al.* [5] obtained with the ARGUS code for a primary energy  $E_0$  of 3.2 keV, is shown in figure (c).

layers thick, which corresponds to about 15 Å. During the simulation adaptive optimization was used starting from a subdivision in 64 rectangles. Each of these rectangles was bombarded with 2000 ions and, if at least one of these was detected, the rectangle was subdivided. Thus, from a total of  $4 \times 10^6$  collision sequences only about  $1.9 \times 10^5$  were actually calculated. The remaining collision sequences were not calculated due to the adaptive optimization. The total number of collisions calculated was  $2.7 \times 10^6$  which gives a mean number of collisions per sequence of about 14.5. A total number of  $2.4 \times 10^3$  ions were detected and the computer time required was about 2 hours on a HP 9000/425 workstation. The result of this simulation is shown in figure 5.3b. To test the influence of the adaptive optimization, the same spectrum was calculated subdividing a rectangle when at least one out of 4000 ions was detected. Both simulated spectra were identical.

The same experimental spectrum was compared to a simulated spectrum calculated with the ARGUS code by Helbig *et al.* [5]. Since the experimental spectra obtained at 2.4 and 5 keV showed no significant differences, they used a primary energy of  $E_0 = 3.2$  keV in their simulation. Their result is shown in figure 5.3c. There is a reasonable correspondence between the experimental and the simulated spectra. Besides the single scattering peak at  $E/E_0 \approx 0.48$  and the double scattering peak at  $E/E_0 \approx 0.65$ , a small peak at  $E/E_0 \approx 0.52$  is visible, although not as clearly as in the experimental spectrum. Both simulated spectra show an almost constant intensity below  $E/E_0 \approx 0.4$  with possibly a small maximum around  $E/E_0 \approx 0.1$ .

Recently, Hsu and Rabalais presented measurements for  $\text{Ne}^+$  ions scattering from the Ni(100) surface [24], which were obtained with the time-of-flight scattering and recoiling spectrometry (TOF-SARS) technique [25]. With this technique, both neutrals plus ions and neutrals only can be collected. As a result ion fractions can be determined. The measurements concerning the dependency of the combined intensity of neutrals and ions on the angle  $\alpha$  between the ion beam and the sample surface are well suited for simulation purposes, because charge exchange processes do not influence the results. Two of these measurements in the  $\langle 100 \rangle$  and  $\langle 110 \rangle$  directions were simulated using the SISS-92 code. For these measurements, the primary energy of the ions was set to 8 keV and the total scattering angle was fixed at  $166^\circ$ . Both intensity profiles clearly show the effects of focusing and shadowing. These intensity profiles were simulated with the SISS-92 code with an idealised ion source for a bulk-terminated surface of four atomic layers thick [26,22]. The results are shown in the figures 5.4a and 5.5a. The idealised ion source causes all peaks to be very sharp. In order to account for imperfections in the ion source and detector (as used in the experiment) and for the thermal vibrations of the atoms in the surface, the simulated intensity profiles were convoluted with a gaussian. The results are shown in the figures 5.4b and 5.5b. The widths of the gaussians correspond reasonably with the width of the angular distribution of the ions emerging from the ion source [27]. The peaks are reproduced rather well in this manner. Therefore, the divergence of

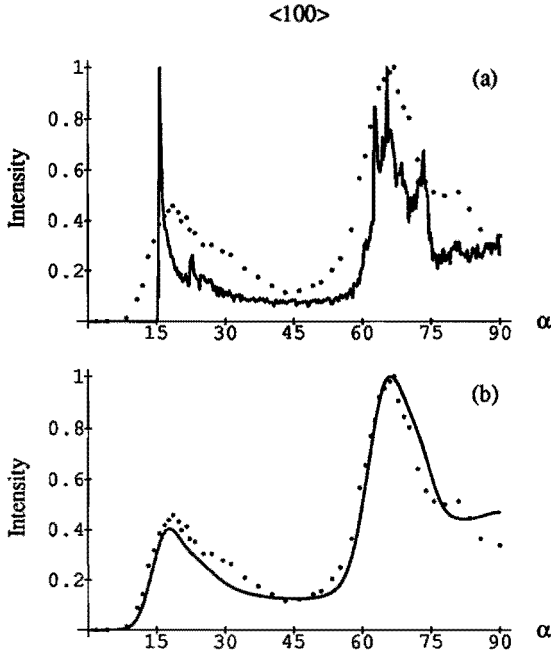


Figure 5.4: The intensity profiles of 8 keV  $\text{Ne}^+$  ions scattering from the Ni(100) surface in the  $\langle 100 \rangle$  direction. The measurements are indicated by the dots. In figure (a) the simulated profile is shown before convolution and in figure (b) and after convolution with a gaussian.

the primary ion beam is one of the main causes of the broadening of peaks. The low intensity parts are reproduced less good especially at larger values of  $\alpha$ . This is probably due to the fact, that here a significant amount of the detected particles is scattered from the fifth to ninth atomic layer [24]. In order to investigate the influence of thermal vibrations and a realistic ion source, two simulations were done for the  $\langle 100 \rangle$  direction.

The result of a simulation with thermally vibrating atoms, is shown in figure 5.6a. The same bulk-terminated Ni(100) surface was used as before. The rms amplitude of the thermal vibrations in the bulk of  $0.042 \text{ \AA}$  was obtained from Ref. [28]. The atoms near the surface have an increased amplitude. Here, the data from ref. [29] were used. The sharp peaks from figure 5.4a have broadened and their intensity ratio has changed. Since the amplitude is largest for the top layer, the left peak is broadened most. Furthermore, a broad peak appears at  $\alpha \approx 30^\circ$ . This peak corresponds with a slight increase in the intensity in the experimental data. This

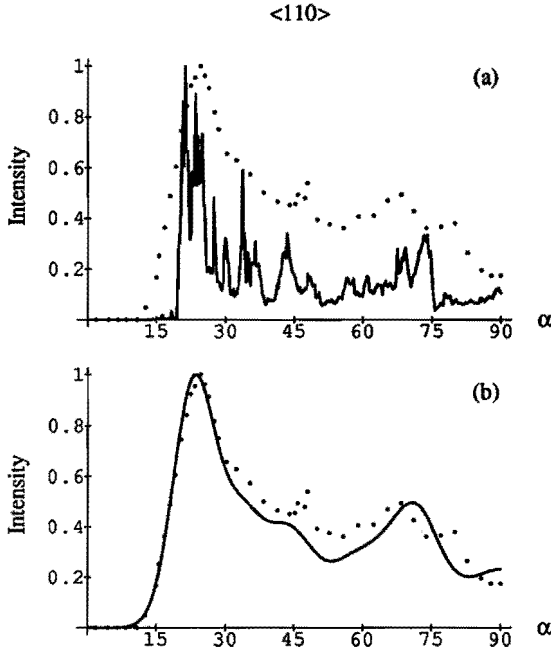


Figure 5.5: The intensity profiles of 8 keV  $\text{Ne}^+$  ions scattering from the Ni(100) surface in the  $\langle 110 \rangle$  direction. The measurements are indicated by the dots. In figure (a) the simulated profile is shown before convolution and figure (b) after convolution with a gaussian.

can be seen in figure 5.6b, where the simulation result is shown after applying a convolution with a gaussian in order to take into account the divergence of the primary ion beam. A good agreement with the experimental results is obtained in this manner. Note, that the fact, that the height of the left peak is somewhat too low, suggests that the amplitude of the top atoms should be smaller.

In figure 5.7 the result of a simulation with a realistic ion source is shown. For this simulation the width of the angular distribution of the ions was set to  $4^\circ$ , which is the same value as used for the convoluted intensity profile of figure 5.4b. The width of the distribution in the energy was taken 20 eV. Note, that the statistics has decreased in comparison with figure 5.4a. This is due to the fact, that the number of ions reaching the detector has decreased by using of a realistic ion source. The shape of the intensity profile is similar to the convoluted profile from figure 5.6b.

Comparing the effect of thermal vibrations to the introduction of a more realistic ion source, it appears that the broadening in the intensity profile is mostly due to

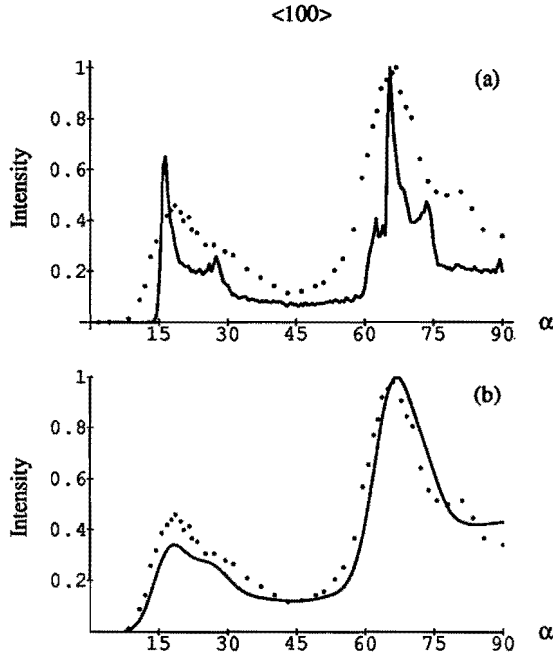


Figure 5.6: The simulated intensity profile using an idealised ion source of 8 keV  $\text{Ne}^+$  ions scattering from the Ni(100) surface in the  $\langle 100 \rangle$  direction. Thermal vibrations of the surface atoms were taken into account. In figure (a) the simulated profile is shown before convolution and figure (b) after convolution with a gaussian.

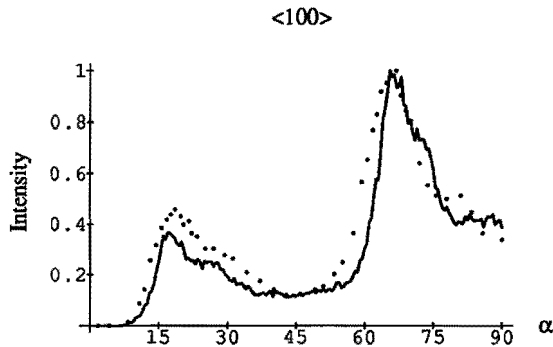


Figure 5.7: The simulated intensity profile using a realistic ion source of 8 keV  $\text{Ne}^+$  ions scattering from the Ni(100) surface in the  $\langle 100 \rangle$  direction. The width of the angular distribution of the primary ions was  $4^\circ$  and the width of the energy distribution was 20 eV.

the divergence in the primary ion beam and the imperfections in the detector used in the experiment.

## 5.4 Conclusions

A fast ion scattering simulation code was developed. The results of this code were shown to match experimental results well. It was used to study the influence of thermal vibrations and a realistic ion source on the intensity profiles of 8 keV Ne<sup>+</sup> ions scattering from the Ni(100) surface. It appears, that, in order to compare experimental with simulated intensity profiles in more detail, thermal vibrations and the imperfections in the ion source and detector have to be incorporated in the simulations. Furthermore, scattering from more than the first four atomic layers has to be considered, when the primary ion beam makes a large angle with the surface.

Future plans are to implement various models accounting for charge-exchange processes.

## References

- [1] T.M. Buck, G.H. Wheatly, D.P. Jackson, Nucl. Instr. and Meth. 218 (1983) 257
- [2] M. Aono, Y. Hou, C. Oshima, Y. Ishizawa, Phys. Rev. Lett. 49 (1982) 567
- [3] M.T. Robinson, I.M. Torrens, Phys. Rev. B 9 (1974) 5008
- [4] D.P. Jackson, W. Heiland, E. Taglauer, Phys. Rev. B 24 (1981) 4198
- [5] H.F. Helbig, M.W. Linder, G.A. Morris, S.A. Steward, Surf. Sci. 114 (1982) 251
- [6] E. Preuss, Rad. Eff. 38 (1978) 151
- [7] D.P. Jackson, J. of Nucl. Mat. 93 & 94 (1980) 507
- [8] R.S. Daley, J.H. Huang, R.S. Williams, Surf. Sci. 215 (1989) 281
- [9] R.M. Tromp and J.F. van der Veen, Surf. Sci. 133 (1983) 159
- [10] D.M. Goodstein, S.A. Langer, B.H. Cooper, J. Vac. Sci. Technol. A6 (1988) 703
- [11] G. Molière, Z. Naturforsch. 2a (1947) 133

- [12] O.B. Firsov, Zh. Eksp. Teor. Fiz. 36 (1959) 1517 [Sov. Phys.-JETP 36 (1959) 1076]
- [13] O.S. Oen, M.T. Robinson, Nucl. Instr. and Meth. 132 (1976) 647
- [14] C.A. Severijns, G. Verbist, H.H. Brongersma, J.T. Devreese, Comp. Phys. Comm. 70 (1992) 459 (Chapter 4 of this thesis.)
- [15] J.P. Landuijt, R. de Grijse, L. van der Elstraeten, J. Vennik, Surf. Sci. 152/153 (1985) 114
- [16] F.P. Preparata, M.I. Shamos, *Computational geometry : an introduction*, Springer Verlag, Berlin 1988, ISBN 3-540-96131-3
- [17] F. James, Rep. Prog. Phys. 43 (1980) 1147
- [18] K. Zakrzewska, J. Dudek, N. Nazarewicz, Comp. Phys. Comm. 14 (1978) 299
- [19] J.H. Halton, Num. Math. 2 (1960) 84
- [20] M. Berblinger, Ch. Schlier, Comp. Phys. Comm. 66 (1991) 157
- [21] T.M. Buck, G.H. Wheatly, L.K. Verheij, Surf. Sci. 90 (1979) 635
- [22] J.M. MacLaren, J.B. Pendry, P.J. Rous, D.K. Saldin, G.A. Somorjai, M.A. van Hove, D.D. Vvedensky, *Surface Crystallographic Information Service: A Handbook of Surface Structures*, D. Reidel Publishing Company, Dordrecht, The Netherlands 1987, ISBN 90-277-2503-9
- [23] J.W.M. Frenken, J.F. van der Veen, G. Allah, Phys. Rev. Lett 51 (1983) 1876
- [24] C.C. Hsu, J.W. Rabalais, Surf. Sci. 256 (1991) 77
- [25] O. Grizzi, M. Shi, H. Bu, J.W. Rabalais, Rev. Sci. Instrum. 61 (1990) 740
- [26] J.E. Demuth, P.M. Marcus, D.W. Jepsen, Phys. Rev. B11 (1975) 1460
- [27] J.W. Rabalais, private communications
- [28] W. Eckstein, *Computer Simulation of Ion-Solid Interactions*, Springer Series in Materials Science 10, 1991
- [29] J.B. Pendry, *Low-Energy Electron Diffraction* Academic, London & N.Y., 1974





# Chapter 6

## Analytical results for the neutralization integral in LEIS<sup>1</sup>

### Abstract

Exact analytical results are presented for the neutralization integral in low-energy ion scattering (LEIS). These results generalize the results of Godfrey-Woodruff and Richard-Eschenbacher by (i) considering a Coulomb trajectory as well as the usual asymptotic, i.e. free-particle, trajectory, and, (ii) introducing new forms for the neutralization rate. These forms might be relevant parameterizations for reionization as well as neutralization. The analytical results for several ion trajectories are compared to numerical results for the Thomas-Fermi-Molière trajectory. In conclusion, the implementation of these results in simulation codes is discussed.

### 6.1 Introduction

The description of the neutralization in low-energy ion scattering (LEIS) was originally parameterized by Hagstrum [1] as

$$P^+ = \exp \left[ - \int_{-\infty}^{+\infty} R(\vec{r}(t)) dt \right], \quad (6.1)$$

where  $P^+$  denotes the survival probability of the incident ions (i.e. the ion fraction),  $R$  is the so-called neutralization rate, which depends parametrically on the time  $t$  via the ion trajectory  $\vec{r}(t)$ . Note that Eq. (6.1) describes Auger neutralization only, since (quasi-)resonant neutralization gives rise to oscillations in the ion fraction and, therefore, the neutralization rate  $R$  cannot be real. As the resonant neutralization mechanism [2] requires that an unoccupied energy level of the incident ion

---

<sup>1</sup>The contents of this chapter is submitted to Nucl. Instr. Meth. B.

is approximately equal to an occupied level of the solid (atom), this is by no means the general picture. Throughout the present paper, we shall only deal with real functions  $R$ , i.e. Auger neutralization.

In the original work of Hagstrum [1] the neutralization at a metallic surface was considered. In view of the homogeneous electron density at the surface, it was assumed that the neutralization rate  $R$  would only depend on the perpendicular distance  $z(t)$  of the ion to the surface. Hagstrum proposed the explicit form

$$R(t) = A e^{-a z(t)}, \quad (6.2)$$

which can be made plausible by realizing that the overlap integral of two hydrogenic wave functions –centered at different nuclei– is an exponential function of the inter-nuclear separation at large distances. The parameters  $A$  and  $a$  are the so-called neutralization constants.

Godfrey and Woodruff [3] described the neutralization at an individual surface (or adsorbed) atom by means of

$$R(t) = A e^{-a |\vec{r}(t) - \vec{r}_{\text{at}}|}, \quad (6.3)$$

where  $\vec{r}_{\text{at}}$  denotes the position of the atom. The analogy between Eqs. (6.2) and (6.3) was examined in Ref. [4]. It was shown that the continuum limit of the Godfrey-Woodruff rate coincides approximately with the Hagstrum rate. Full correspondence is obtained only for straight-line trajectories. Souda *et al.* [5] have remarked that the neutralization constant  $a$  in the Godfrey-Woodruff picture can be related to the (inverse) ionic radius of the atom considered.

In order to discuss the integration in Eq. (6.1), one has to have an idea of the trajectory and the velocity of the ion. It has been shown that the trajectory of the ion can be obtained by considering its scattering at the solid surface as a sequence of binary collisions with individual surface atoms [6]. During each collision, the surface atom can be taken to be a free particle and the ion-atom potential is a screened Coulomb potential

$$V(r) = \frac{Z_{\text{at}} Z_{\text{ion}} e^2}{4\pi\epsilon_0 r} \Phi\left(\frac{r}{C a_{TF}}\right), \quad (6.4)$$

where  $\Phi(x)$  is the Molière approximation [7] to the Thomas-Fermi screening function,  $a_{TF}$  is the Thomas-Fermi screening length as given by Firsov [8], and  $C$  is a parameter of order unity. As the neutralization rate of Eq. (6.3) only refers to the ion-atom distance it is convenient to transform the two-particle system to center-of-mass and relative coordinates. Applying the conservation laws for angular momentum and energy, it is easily found that the motion is planar and the following explicit formula can be derived for the radial velocity  $v_{rad}$  as a function of the ion-atom distance  $r$

$$v_{rad}(r) = \frac{dr}{dt}(r) = v_{in} \sqrt{1 - \left(\frac{s}{r}\right)^2 - \frac{V(r)}{E}}, \quad (6.5)$$

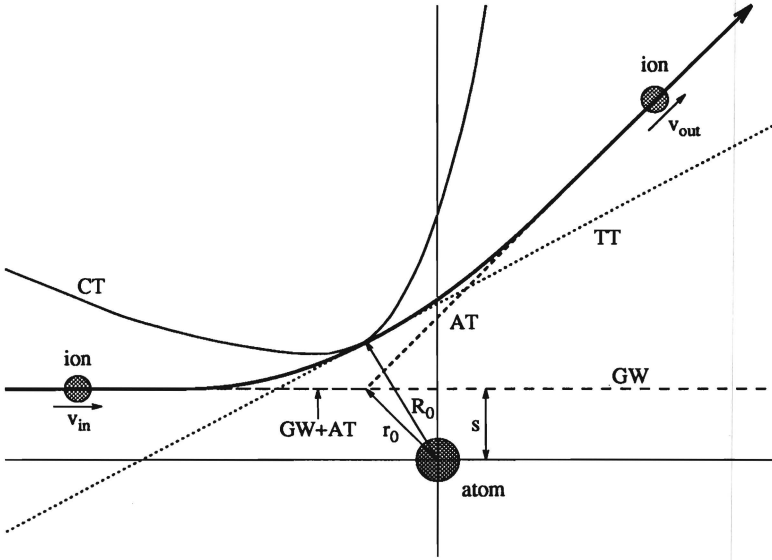


Figure 6.1: The trajectories used in calculating the neutralization integral and their parameters. The trajectory GW is the asymptote of the incoming trajectory used by Godfrey and Woodruff and AT is the asymptotic trajectory of Eq. (6.8). The tangent of the exact trajectory in the point of closest approach is indicated by TT and the Coulomb trajectory in the point of closest approach is indicated by CT.

where  $s$  is the impact parameter. The initial velocity  $v_{in}$  is connected to the relative energy  $E = \frac{1}{2}\mu v_{in}^2$ , where  $\mu$  is the reduced mass of the ion-atom system. In terms of the total energy one has  $E = \frac{\mathcal{A}}{1+\mathcal{A}}E_{tot}$ , where  $\mathcal{A} = m_{at}/m_{ion}$  is the mass ratio. The radial velocity  $v_{rad}$  is zero at the distance of closest approach  $R_0$ , which is the root of the equation

$$1 - \left(\frac{s}{r}\right)^2 - \frac{V(r)}{E} = 0. \quad (6.6)$$

It is well known, that apart from Eq. (6.5), one can obtain the asymptotic velocities ( $v_{in}$  and  $v_{out}$ ) in the laboratory system by invoking merely the conservation laws for total energy and momentum under the condition that the total scattering angle  $\Theta$  is known

$$\frac{v_{out}}{v_{in}} = \frac{\cos \Theta + \sqrt{\mathcal{A}^2 - \sin^2 \Theta}}{1 + \mathcal{A}}. \quad (6.7)$$

This gives rise to the so-called asymptotic trajectory (see figure 6.1)

$$\vec{r}(t) = \begin{cases} \vec{r}_0 + \vec{v}_{in}t & (t < 0) \\ \vec{r}_0 + \vec{v}_{out}t & (t > 0) \end{cases}, \quad (6.8)$$

where  $\vec{r}_0$  is the intersection of the asymptotes. Using this trajectory the ion fraction  $P^+$  can be calculated analytically for the neutralization rate of Eq. (6.2) [9], but not for the one of Eq. (6.3). However, it was shown by Godfrey and Woodruff [3], that the latter can be used in combination with a straight-line trajectory  $\vec{r}(t) = \vec{s} + \vec{v}_{in}t$  in which case the ion fraction  $P^+$  is given by

$$P_{GW}^+ = \exp \left[ -\frac{2A}{va} as K_1(as) \right], \quad (6.9)$$

where  $K_1$  is a modified Bessel function of the second kind.

Richard and Eschenbacher [10] used a matching potential of the form

$$V(r) = \frac{\alpha}{2} \left[ \left( \frac{\beta}{r} \right)^2 - 1 \right] \quad (6.10)$$

to obtain an approximation to the exact classical ion trajectory. The constants  $\alpha$  and  $\beta$  were determined by adjusting Eq. (6.10) to the Thomas-Fermi-Molière (TFM) potential. Using this matching potential, all relevant quantities of the scattering can be calculated analytically resulting in

$$P_{RE}^+ = \exp \left[ -\frac{2A}{a} \sqrt{\frac{\mu}{2E + \alpha}} aR_0 K_1(aR_0) \right]. \quad (6.11)$$

In general, the constant  $\alpha$  is small compared to  $2E$  and can therefore be neglected [11]. In this case, Eq. (6.9) is similar to Eq. (6.11) with  $R_0$  replacing  $s$  and the trajectory is approximated by the tangent in the point of closest approach  $R_0$ . Since the neutralization rate of Eq. (6.3) decreases exponentially, this tangential trajectory is a better approximation to the exact trajectory than the asymptotic straight-line trajectory used by Godfrey and Woodruff.

In the remainder of this paper we present some analytical results for the neutralization integral. In section 6.2, an exact analytical result is presented for the neutralization integral using a Coulomb trajectory. In section 6.3 new analytical forms of the neutralization rate are proposed, that can incorporate ionization. A comparison of the models is given in section 6.4. Finally the conclusions of this work are summarized in section 6.5.

## 6.2 The ion fraction for a Coulomb trajectory

In the case of the Coulomb trajectory, a potential  $V(r) = V/r$  must be used in Eq. (6.5). It is useful to introduce the parameter  $U = V/E$  which has the dimensions of a length. Starting from the integral, Eq. (6.1), we first make a change of integration variable  $t \rightarrow r$  and Eq. (6.5) is used for the corresponding Jacobian. This leads to the following form for the ion fraction

$$P_C^+ = \exp \left[ -\frac{A}{v_{in}} F \right], \quad (6.12)$$

where the non-trivial part  $F$  is given by

$$\begin{aligned} F &= \int_{R_0}^{\infty} e^{-ar} \frac{1}{\sqrt{1 - \left(\frac{s}{r}\right)^2 - \frac{U}{r}}} dr \\ &= \int_{R_0}^{\infty} e^{-ar} \frac{r}{\sqrt{r^2 - Ur - s^2}} dr, \end{aligned} \quad (6.13)$$

where the distance of closest approach  $R_0$ , Eq. (6.6), is explicitly given by

$$R_0 = \frac{1}{2} \left( U + \sqrt{U^2 + 4s^2} \right). \quad (6.14)$$

Completing the square under the root sign in Eq. (6.13) suggests the introduction of a new variable  $x$  by

$$r = \frac{U}{2} + \sqrt{s^2 + \frac{U^2}{4}} \cosh x, \quad (6.15)$$

to cast Eq. (6.13) in the form

$$F = e^{-aU/2} \int_0^{\infty} \left[ \frac{U}{2} + \sqrt{s^2 + \frac{U^2}{4}} \cosh x \right] \exp \left( -a \sqrt{s^2 + \frac{U^2}{4}} \cosh x \right) dx. \quad (6.16)$$

The resulting integral is easily recognized as a (linear combination of) modified Bessel function(s) of the second kind  $K_\nu$ , and we arrive at the result

$$F = e^{-aU/2} \left[ \frac{U}{2} K_0 \left( a \sqrt{s^2 + \frac{U^2}{4}} \right) + \sqrt{s^2 + \frac{U^2}{4}} K_1 \left( a \sqrt{s^2 + \frac{U^2}{4}} \right) \right]. \quad (6.17)$$

For the discussion in section 6.4, our main interest lies in the distance of closest approach  $R_0$ . Therefore, we eliminate  $U$  in favor of  $R_0$ , by introducing a dimensionless parameter  $\eta$

$$\eta = \frac{1}{2} \left( \frac{R_0}{s} - \frac{s}{R_0} \right) = \frac{U}{2s}, \quad (6.18)$$

which is confined to  $\eta \in [0, 1]$  as  $R_0 \geq s$ . The final result of this section is

$$F = s e^{-as\eta} \left[ \eta K_0 \left( as \sqrt{1 + \eta^2} \right) + \sqrt{1 + \eta^2} K_1 \left( as \sqrt{1 + \eta^2} \right) \right]. \quad (6.19)$$

Note that for vanishing Coulomb repulsion  $\eta \rightarrow 0$  the result of Godfrey-Woodruff for the asymptotic trajectory is re-obtained from Eq. (6.19).

### 6.3 Generalization of the neutralization rate

So far, only an exponentially decreasing neutralization rate has been considered. However, in certain cases an extra contribution to the neutralization rate is needed for small ion-atom distances [11]. Furthermore, as the neutralization rates – considered above – are positive definite functions of the ion-atom distance  $r$ , the ion

fraction  $P^+$  is always smaller than unity, i.e., it describes *only* neutralization. Experimentally, Aono and Souda [12] have demonstrated that above a so-called threshold energy reionization occurs for certain ion-atom combinations. The occurrence of such (re-)ionization is mostly incorporated in an “ad hoc” manner during simulations. As a first approximation, one can neglect the neutralization on the incoming trajectory [4] which is only valid for almost complete reionization by the atom. Pierson *et al.* [13] assume that ionization occurs when the ion gets closer to the target atom than a given critical distance. In this case, they use the Landau-Zener formula by Tsuneyuki and Tsukada [14] to calculate the ionization probability.

The approaches discussed above make it cumbersome to determine whether or not ionization occurs only by making the fit to the experimental data. Indeed, the (re-)ionization effects are already put in the simulation before the fitting of the neutralization constants starts. Although this might be the appropriate procedure if the ion-surface combination under consideration is well understood, it is of interest to devise a form for the neutralization rate which is applicable to both neutralization and (re-)ionization. In that case, the fitting procedure would tell us whether or not we are dealing with an ion-surface combination in which (re-)ionization is of importance. Inspection of Eq. (6.1) shows that for (re-)ionization the neutralization rate has to become negative. The experiments of Aono and Souda [12] show that the reionization is only expected at small distances.

The most simple modification of the Godfrey-Woodruff neutralization rate is the insertion of an extra linear term before the exponential

$$R_l(r) = [A_0 + A_1 ar] e^{-ar} . \quad (6.20)$$

Note, however, that the asymptotic behavior  $R \sim r e^{-ar}$  is no longer purely exponential. Therefore, we propose the addition of a hyperbolic term

$$R_h(r) = \left[ A_0 + \frac{A_1}{ar} \right] e^{-ar} . \quad (6.21)$$

This form has the advantage that the reionization effects, which behave as  $1/r$ , occur at small atom-ion distances without spoiling the asymptotic behavior. This neutralization rate, Eq. (6.21), diverges for small values of  $r$ . However, the value  $r = 0$  is included only in the integration domain for  $R_0 \rightarrow 0$ , i.e. under the condition that both (i)  $s = 0$ , and, (ii)  $E \rightarrow \infty$ .

The ion fractions for both neutralization rates, Eqs. (6.20) and (6.21), can in principle be calculated using a hyperbolic substitution as was done in section 6.2. In order to avoid this tedious calculation, we propose the more elegant way of “*differentiation and integration under the integral*” with respect to the neutralization constant  $a$ . Let us start by the elementary observation

$$r^n e^{-ar} = \left( -\frac{\partial}{\partial a} \right)^n e^{-ar}$$

$$\frac{1}{r^n} e^{-ar} = \left( \prod_{j=1}^n \int_{a_{j-1}}^{\infty} da_j \right) e^{-a_n r}, \quad (6.22)$$

where  $a_0 = a$  has to be taken in the last equation. Using these results, Eqs. (6.21) and (6.20) can also be written as

$$R_l(r) = \left[ A_0 - A_1 a \frac{\partial}{\partial a} \right] e^{-ar}. \quad (6.23)$$

and

$$R_h(r) = \left[ A_0 - \frac{A_1}{a} \int_a^{\infty} da' \right] e^{-a'r} \quad (6.24)$$

Substituting these in Eq. (6.1) and moving the factors between the square brackets outside the integral, the ion fractions are now given by

$$P_l^+ = \exp \left( - \left[ A_0 - A_1 a \frac{\partial}{\partial a} \right] \int_{-\infty}^{+\infty} e^{-ar(t)} dt \right), \quad (6.25)$$

$$P_h^+ = \exp \left( - \left[ A_0 - \frac{A_1}{a} \int_a^{\infty} da' \right] \int_{-\infty}^{+\infty} e^{-a'r(t)} dt \right). \quad (6.26)$$

The integration with respect to the time can be performed analytically for a straight-line, as well as a Coulomb trajectory. Here, we use the tangent to the exact trajectory in the point of closest approach  $R_0$ , since this is a better approximation than the straight-line trajectory used by Godfrey and Woodruff (see section 6.4). As in the Richard-Eschenbacher model, the integration results in the function  $R_0 K_1(aR_0)$ . After applying the square bracket factors to this function and using the properties of the Bessel functions  $K_\nu$ , one finally obtains

$$P_l^+ = \exp \left( - \frac{2}{v} \left[ \frac{A_0 + A_1}{a} aR_0 K_1(aR_0) + \frac{A_1}{a} (aR_0)^2 K_0(aR_0) \right] \right), \quad (6.27)$$

$$P_h^+ = \exp \left( - \frac{2}{v} \left[ \frac{A_0}{a} aR_0 K_1(aR_0) + \frac{A_1}{a} K_0(aR_0) \right] \right). \quad (6.28)$$

We note that a similar derivation can be applied to an even more general form of the neutralization rate

$$R(r) = \left[ \sum_{i=-M}^N A_i (ar)^i \right] e^{-ar}. \quad (6.29)$$

Furthermore, the differentiation (integration) with respect to  $a$ , Eq. (6.22), is easily performed using the recurrence relations for the modified Bessel functions. Moreover, this job can be left to symbolic algebra programs, such as Mathematica [15].



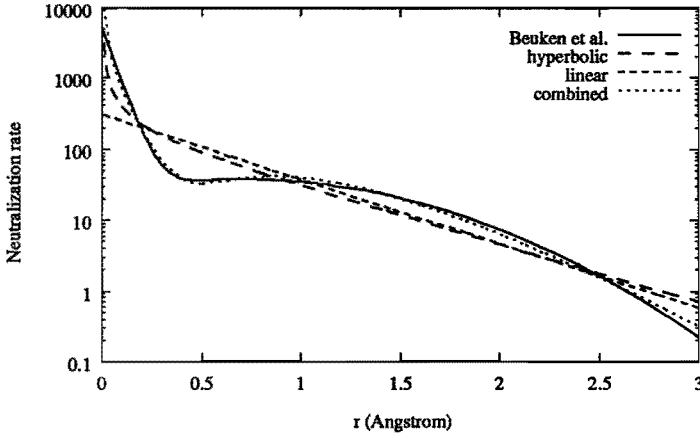


Figure 6.2: Illustration of the use of the generalized neutralization rates. Both were fitted to the neutralization rate for the  $\text{Cl}^-$  ion in the  $\text{NaCl}(001)$  surface as determined by Beuken *et al.* [11]. The curves marked “linear” is the results for fitting Eq. (6.20), the one marked “hyperbolic” for Eq. (6.21). The “combined” curve is the result of fitting Eq. (6.29) with only  $A_i \neq 0$  for  $i \in \{-1, 0, 4\}$ .

With this program, we successfully computed the explicit result of Eq. (6.29) for different values of  $M$  and  $N$ .

As an illustration of the application of the generalized neutralization rates, we have fitted the neutralization rates of Eqs. (6.20), (6.21), and (6.29) with only  $A_i \neq 0$  for  $i \in \{-1, 0, 4\}$  to the neutralization rate for the chlorine atom of the  $\text{NaCl}(001)$  surface as determined by Beuken *et al.* [11]. Their neutralization rate is given by

$$R_i(r) = R_1(A_1, a_1) + R_2(A_2, a_2), \quad (6.30)$$

where  $R_1$  is identical to Eq. (6.3) and  $R_2$  is given by

$$R_2(A_2, a_2) = A_2 \exp\left(-[a_2(r - r_M)]^2\right). \quad (6.31)$$

This gaussian contribution to the neutralization rate is used to simulate the shape of the M layer in the electronic radial distribution of the  $\text{Cl}^-$  ion. The maximum density in this layer is positioned at  $r_M$  and can be fixed at  $0.72 \text{ \AA}$ . The results of the fitting are shown in figure 6.2. The neutralization rates of Eqs. (6.20) and (6.21) fit reasonably well. However, an excellent fit is obtained with Eq. (6.29). This is not surprising when one considers, that the behaviour of the electronic radial distribution of the M layer is dominated by a term of the form  $r^4 e^{-r}$ .

## 6.4 Comparison of analytical and numerical results

Since the neutralization rate Eq. (6.3) depends exponentially on the distance  $r$  between the nuclei of the ion and atom, the (approximating) trajectory is weighted much more heavily for small ion-distances in the integral for the ion fraction. In order to investigate this effect the neutralization constants  $A$  and  $a$  are fixed, while several trajectories are used: (i) the incoming asymptote as used by Godfrey and Woodruff, (ii) the asymptotic trajectory of Eq. (6.8), (iii) the tangent to the ion trajectory at the distance of closest approach (Richard-Eschenbacher with  $\alpha = 0$ ), and, (iv) the Coulomb trajectory with equal distance of closest approach  $R_0$ . The parameters of the actual collision are calculated using the TFM potential.

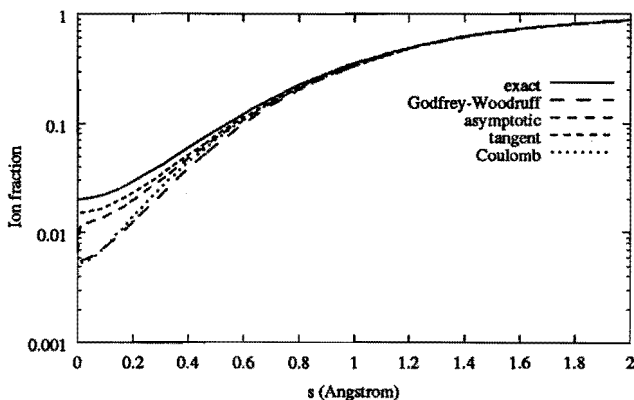


Figure 6.3: Comparison of the ion fraction results calculated for the ion trajectories discussed in the text. The ion fractions were calculated for 4 keV  $\text{Ne}^+$  ions colliding with a nickel atom as a function of the impact parameter  $s$ . The value of the neutralization constants used here are  $A = 1.2 \cdot 10^{16} \text{ s}^{-1}$  and  $a = 2.35 \text{ \AA}^{-1}$ .

The analytical ion fractions, calculated for the approximating trajectories, are compared to the numerically integrated ion fraction of the exact TFM trajectory in figure 6.3. The following observations can be made. The ion fraction according to the Godfrey-Woodruff model is much too low in comparison to the exact TFM trajectory. This is due to the fact, that the minimum ion-atom distance is equal to the impact parameter  $s$  for the incoming asymptote while the actual distance of closest approach  $R_0$  is much larger, especially for small impact parameters. A similar argument is valid for the asymptotic trajectory. Comparing the results for the Godfrey-Woodruff and tangential trajectory, it appears that the smallest ion-atom

distance reached on the approximating trajectory has to be equal to the distance of closest approach  $R_0$  on the exact trajectory. Therefore, an asymptotic trajectory through the point of closest approach as is used by Engelmann and Taglauer [16], might be a better choice.

Although in the case of the Coulomb trajectory, the ion is more distant from the atom than in the case of the exact TFM trajectory, the ion is slowed down at much larger distances. This can be concluded from the formula for the radial velocity, Eq. (6.5), if one realizes that the Coulomb potential has a much longer range than the TFM potential which includes a screening function. As a result, the ion remains longer in the neighbourhood of the atom, where most neutralization occurs, and the ion fraction is lower. The same can be said for the matching potential used by Richard and Eschenbacher, but in this case the deviation is smaller, since the matching potential ( $\sim r^{-2}$ ) decreases faster than the Coulomb potential ( $\sim r^{-1}$ ). From this, we conclude that  $v_{rad}(r)$  is a second important parameter in the neutralization integral next to  $R_0$ .

As a final remark to this section, we note that all the analytical results for the neutralization integral presented here can be implemented efficiently in a code for ion-scattering simulation. The distance of closest approach  $R_0$  can be calculated efficiently without root finding using an accurate numerical approximation based on rational functions, which we developed previously for other LEIS integrals [17]. It is amusing to note, that the same method of approximation is often used in the literature to evaluate transcendental functions, such as the Bessel functions needed here [18].

## 6.5 Conclusions

We have analytically integrated the neutralization rate of the Godfrey-Woodruff form for the Coulomb problem. Furthermore, new expressions for the neutralization rate were proposed. These can be used to determine whether or not (re-)ionization occurs. This is done by fitting to experimental data without any prior knowledge to the fact that ionization occurs. These forms are easily generalized to higher orders in which case the explicit forms for the integrated neutralization rates can easily be obtained in terms of the modified Bessel functions of the second kind  $K_\nu$  by means of symbolic algebra programs following the proposed recipe. We also compared the analytical neutralization integrals with the numerical result for the TFM potential. It appears that the ion trajectory used in calculating the neutralization integral has a strong influence through the dependence on (i) the distance of closest approach  $R_0$ , and, (ii) the radial velocity. The Richard-Eschenbacher form is found to give the best analytical approximation.

Future plans are to use the results for the neutralization integral presented in this

paper for studying charge exchange.

## References

- [1] H.D. Hagstrum, *Phys. Rev.* 96 (1954) 338
- [2] For a review see: J. Los, J.J.C. Geerlings, *Phys. Rep.* 3 (1990) 133
- [3] D.J. Godfrey, D.P. Woodruff, *Surf. Sci.* 105 (1981) 438
- [4] G. Verbist, J.T. Devreese, H.H. Brongersma, *Surf. Sci.* 233 (1990) 323
- [5] R. Souda, M. Aono, C. Oshima, S. Otani, Y. Ishizawa, *Nucl. Instr. Meth. B15* (1986) 138
- [6] See, e.g., W. Eckstein, *Computer Simulation of Ion-Solid Interactions*, Springer Series in Materials Science 10, 1991
- [7] G. Molière, *Z. Naturforsch.* 2a (1947) 133
- [8] O.B. Firsov, *Sov. Phys. JETP* 6 (1958) 534
- [9] D.P. Woodruff, *Nucl. Instr. Meth.* 194 (1982) 639
- [10] A. Richard, H. Eschenbacher, *Nucl. Instr. Meth. B2* (1984) 444
- [11] J.-M. Beuken, E. Pierson, P. Bertrand, *Surf. Sci.* 223 (1989) 201
- [12] M. Aono, R. Souda, *Nucl. Instr. Meth. Phys. Res. B27* (1987) 55
- [13] E. Pierson, J.-M. Beuken, P. Bertrand, *Surf. Sci.* 214 (1990) 374
- [14] S. Tsuneyuki, M. Tsukada, *Phys. Rev. B34* (1986) 5758
- [15] S. Wolfram, *Mathematica, A System for Doing Mathematics by Computer*, Wolfram Research, Inc. and Addison-Wesley 1988
- [16] G. Engelmann, E. Taglauer, *Nucl. Instr. Meth. B13* (1986) 240
- [17] C.A. Severijns, G. Verbist, H.H. Brongersma, J.T. Devreese, *Comp. Phys. Comm.* 70 (1992) 459 (Chapter 4 of this thesis.)
- [18] See, e.g., W.H. Press, B.R. Flannery, S.A. Teukolsky, W.T. Vetterling, *Numerical Recipes in C: The Art of Scientific Computing*, Cambridge University Press 1988



# Chapter 7

## A computer study of charge exchange in low-energy ion scattering

### Abstract

The charge-exchange processes in low-energy ion scattering (LEIS) are studied by means of simulations. For  $\text{Ne}^+$  ions scattering from the Ni(100) surface no indications are found for reionization for energies up to 8 keV. The ion fractions are equally well described by core as valence neutralization. This can be explained by the correlation between the number of collisions,  $N$ , and the interaction time,  $t$ , along the ion trajectory. It is concluded, that the neutralization/ionization needs to be calculated along all relevant trajectories. Future experiments are suggested to examine the  $(N, t)$  correlation in more detail.

### 7.1 Introduction

Charge exchange (i.e., neutralization and ionization) is an important issue in low-energy ion scattering (LEIS). On the one hand, it makes LEIS a very surface-sensitive analysis technique. On the other hand, it complicates the interpretation of the LEIS spectra, since only the charged particles that are backscattered from the sample surface are detected in a LEIS experiment.

Recently, it has become possible to do time-of-flight (TOF) experiments with sufficient statistics. An attractive feature of the TOF technique is, that one can collect neutrals and ions combined or separately. Therefore, the charge-exchange processes can be studied. In this paper, we focus on the experimental results by Rabalais [1] and Hsu and Rabalais [2], where  $\text{Ne}^+$  ions scattering from the Ni(100)

surface are studied at 4 and 8 keV by TOF. Furthermore, energy-dependent data with a conventional (charge-detecting) LEIS apparatus, MINIMOBIS [3], are used.

In a LEIS experiment, ions with an energy in the keV range are used. The motion of such an ion can be studied within the framework of classical mechanics by approximating it as a sequence of binary collision with the surface atoms. During such a trajectory, the ion can be neutralized, re-ionized, etc.. In this energy range, the charge state of the ion does not affect its (classical) trajectory. Hence, the total process can be separated in a “classical” part (the trajectory calculation) and a “quantum mechanical” part (the charge exchange).

The simulation code SISS-92 was previously validated [4] by comparison with the experimental data by Hsu and Rabalais [2]. When implementing charge exchange in a simulation code, two approaches have been proposed in the literature: (i) using a quasi ab-initio calculation or (ii) using a parameterization. The first approach results in a quantum-mechanical model, such as those by Mišković and Janev [5], Ishii [6], and Muda and Newns [7]. Owing to their detailed nature, the calculation time can become quite large. Therefore, one is limited in practice to calculating them along a representative trajectory (during which only one collision has taken place). Thus, first the trajectories are averaged and then the ion fraction is calculated for this trajectory. In an ion-scattering simulation, a large number of ion trajectories is calculated. Therefore, parameterizations are better suited for this purpose, because they can be evaluated efficiently.

In section 7.2, the charge-exchange parameterizations are discussed. The experiments, simulations and fitting procedure are described in section 7.3. The results are presented in section 7.4 and discussed in section 7.5. The conclusions of this work are summarized in section 7.6.

## 7.2 Parameterizations for charge-exchange

Hagstrum [8] was the first to write down a parameterization for the survival probability of an ion,  $P^+$ , after the interaction with a surface

$$P^+ = \exp \left( - \int_{-\infty}^{+\infty} R(\vec{r}(t)) dt \right). \quad (7.1)$$

Here,  $R(\vec{r})$  is the neutralization rate and  $\vec{r}(t)$  is the trajectory of the ion. Note that Eq. (7.1) cannot describe resonant neutralization, because  $R$  is real. Fortunately, this is sufficient when  $\text{Ne}^+$  ions scatter from a nickel surface, because resonant neutralization does not occur. Two types of parameterizations can be distinguished: (i) local and (ii) global parameterizations. In a local parameterization the neutralization rate  $R$  depends on the ion-atom distance, while in a global parameterization

this is not the case. This reflects the difference between the localized wave functions of the core electrons and the extended wave functions of the valence electrons.

Hagstrum considered very low energy ions scattering from a metal surface. Such ions do not penetrate the surface. Therefore, Hagstrum assumed that the neutralization rate depends only on the distance of the ion above the surface. In the case of LEIS, the ions do penetrate the surface and, as a result, the electrons within the surface have to be considered too. Since the electron distribution within the surface is approximately homogeneous, the neutralization rate can be described by

$$R(z) = \begin{cases} A & (z \leq h) \\ A e^{-a(z-h)} & (z > h) \end{cases}, \quad (7.2)$$

where  $A$  and  $a$  are the neutralization constants. We note that this neutralization rate describes the charge exchange of the ion with an homogeneous electron gas in the jellium approximation and resembles the one used in Ref. [9]. Alternatively, one can assume that the ion fraction depends only on the time during which it remains within the solid surface. In this case, the ion fraction is given by [10,11]

$$P^+ = \exp(-t_h/\tau), \quad (7.3)$$

Here,  $t_h$  is the time spent by the ion below a reference plane, which is at a distance  $h$  above the top most atom layer, and  $\tau$  is a characteristic time. We note, that the neutralization rate for the parameterization, Eq. (7.3), changes discontinuously, when the ion passes the reference plane. As a result, it lacks a Hagstrum-like behaviour.

In the local parameterization by Godfrey and Woodruff [12] it is assumed that the neutralization decreases exponentially with increasing ion-atom distance

$$R(r) = A e^{-a|\bar{r}-\bar{r}_{at}|}. \quad (7.4)$$

Richard and Eschenbacher [13] integrated this neutralization rate using a matching potential, which results in

$$P^+ = \exp\left(-2\sqrt{\frac{\mu}{2E+\alpha}} AR_0 K_1(aR_0)\right). \quad (7.5)$$

Here  $\alpha$  is a potential fitting parameter,  $E$  is the energy in the center-of-mass system,  $\mu$  is the reduced mass of the ion-atom system,  $R_0$  is the distance of closest approach, and  $K_1$  is a modified Bessel function of the second kind. Usually  $\alpha$  is small in comparison to  $2E$  [14] and, therefore, can be neglected. In this case ( $\alpha = 0$ ), Eq. (7.5) gives the survival probability of an ion moving with a constant velocity along the tangent to the exact ion trajectory in the point of closest approach. In the remainder of this paper, we will refer to this model as the *tangent* model.



Experimental results indicate that (re-)ionization can occur for violent collisions above a critical energy [15]. This energy corresponds to an upper-bound for the distance of closest approach. Therefore, ionization can only be introduced in a local parameterization. This can be done by allowing the neutralization rate to have negative values. Recently, we have shown that analytical results exist for these neutralization integrals [16]. Two of the proposed rates are used in this work to investigate whether (re-)ionization occurs: the hyperbolic form

$$R_h(r) = \left( A_0 + \frac{A_1}{ar} \right) e^{-ar} , \quad (7.6)$$

and the linear form

$$R_l(r) = (A_0 + A_1 ar) e^{-ar} . \quad (7.7)$$

In both cases, the ion fraction is calculated for the same approximating trajectory as is used in the tangent model. The negativity of the rates (7.6) and (7.7) indicates the presence of reionization effects.

### 7.3 Experiments, simulations and fitting

Two sets of experimental data are used: (i) ion fraction data obtained with the TOF-SARS technique [17] and (ii) ion intensity data as a function of the primary ion beam energy. The first data set consists of the ion fraction measurements by Rabalais and Hsu [1,2]. They measured the dependence of the ion fraction on the azimuth,  $\phi$ , for 4 and 8 keV  $\text{Ne}^+$  ions scattering from the Ni(100) surface for several values of the angle,  $\alpha$ , between the primary ion beam and the sample surface. The total scattering angle was  $166^\circ$ . For these data the main experimental influence appeared to be the broadening of the peaks, which is due to the divergence of the primary ion beam, the thermal vibrations of the surface atoms, and the finite resolution of the detector. Previous simulation results show, that the main cause of this broadening is the divergence of the primary ion beam [4]. Therefore, the divergence of the primary ion beam was taken into account in the simulations, while the other experimental conditions were not considered. Fully three-dimensional simulations were used to obtain information on a large number (typically  $10^9$ ) of ion trajectories that contribute to the signal. This information was stored for later use in the fit programmes.

The second data set consists of measurements of the ion intensity as a function of the primary energy in the range from 1 to 5 keV measured with the MINIMOBIS apparatus [3]. In the experiments, the primary ion beam was incident perpendicular to the surface. The cylindrical mirror analyzer (CMA) fixed the total scattering angle at  $144^\circ$ . The spectra were corrected for the energy-dependent sensitivity of the CMA. In order to determine the intensity of the back-scattered ions, the peaks in the

spectra were fitted using the functions for the peak shapes proposed by Nelson [18] and Young *et al.* [19]. Since nickel has five isotopes, five peak functions at fixed distances from each other were used. The intensity ratios of the five peaks obtained in this manner, were in good agreement with the abundance of the isotopes. In several spectra a peak was present corresponding with  $^{22}\text{Ne}^+$  ions, which is due to a sub-optimal setting of the mass filter for the incident ions. For these spectra a second set of five peaks was used, which was chosen identical to the first set except for the height and the position. The intensities obtained were normalized on the primary ion beam current. In the simulations only the most abundant isotopes of neon and nickel were used. The divergence of the primary ion beam and the thermal vibrations of the surface atoms were not taken into account, because the CMA integrates the intensity of the back-scattered ions over the complete azimuthal range.

## 7.4 Results

The results of fitting to the ion-fraction data for 8 keV  $\text{Ne}^+$  ions scattering from the Ni(100) surface are shown in figure 7.1. The values of the neutralization constants obtained from the fits are listed in table 7.1. It is important to note, that only the values of the sum of the squared errors,  $\chi^2$ , within a single table are to be compared, because each table presents the parameter values obtained for different experimental data. All features in the experimental data are reproduced in the fits. The divergence of the primary ion beam seems to be overestimated for the data of  $35^\circ$  and  $45^\circ$  (figures 7.1b and c). We note that when each of the four azimuthal scans at 8 keV is fitted separately, no significant differences in the goodness-of-fit are found. Such differences are only found by fitting to all data simultaneously. This is due to the increased number of data points used in the latter fits.

Comparing the values of  $\chi^2$ , we see that the time-dependent neutralization parameterization, Eq. (7.3), describes the data worst. This is not surprising, since the neutralization rate contains an unphysical discontinuity. The three local neutralization parameterizations fit equally well to the data. This is illustrated in figure 7.2 where the neutralization rates of these parameterizations are shown for the neutralization constants of table 7.1. The neutralization rates are reliable only when the ion-atom distance  $r$  is larger than the distance of closest approach  $R_0$  for a head on collision ( $\approx 0.16 \text{ \AA}$ ). Furthermore, it appears that by increasing the number of fitting parameters, as is the case for the hyperbolic and linear parameterizations, the value of  $\chi^2$  is not decreased. This is not surprising since the experimental error (about 15%) is quite large. In addition, the dimension of the parameter space is increased making it more difficult for the least-squares procedure to approach the minimum value of  $\chi^2$ . The best fit is obtained with the neutralization rate for an

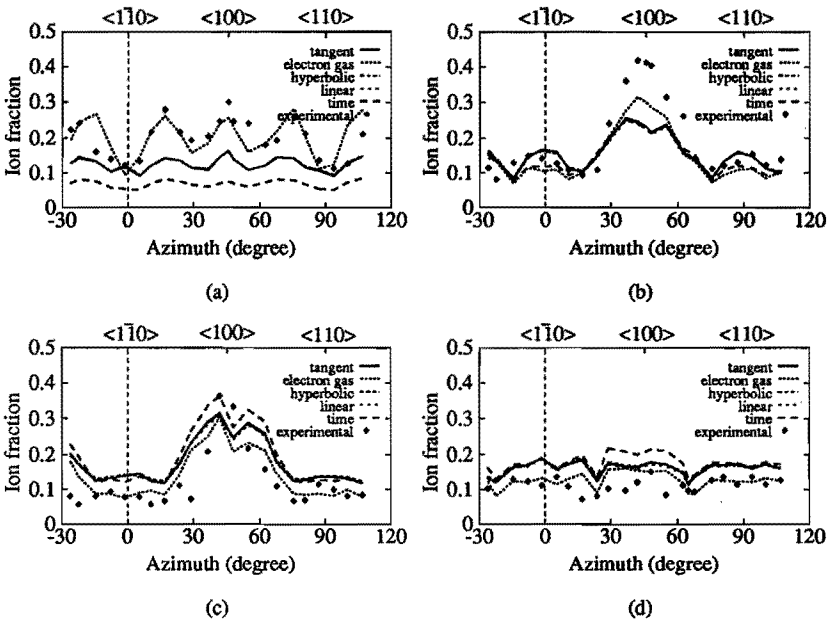


Figure 7.1: The results of fitting the charge-exchange parameterizations discussed in the text to the ion-fraction data for 8 keV  $\text{Ne}^+$  scattering from the Ni(100) surface. The angle between the primary ion beam with the surface is for the figures (a) to (d) respectively 20.5°, 35°, 45°, and 55°.

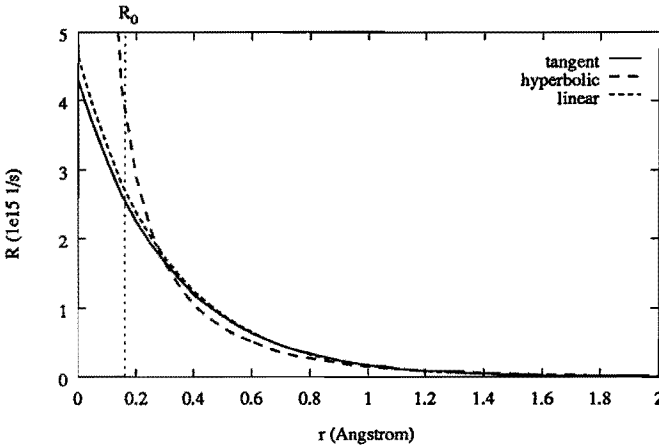


Figure 7.2: The neutralization rates of the local parameterizations as a function of the ion-atom distance for 8 keV  $\text{Ne}^+$  ions scattering from the Ni(100) surface. Note that the distance of closest approach,  $R_0$ , for a head-on collision is  $\approx 0.16$  Å at this energy.

Type	Param.	$\chi^2$	$a$ ( $\text{\AA}^{-1}$ )	$A_{(0)}$ ( $10^{15} \text{ s}^{-1}$ )	$A_1$ ( $10^{15} \text{ s}^{-1}$ )
local	tangent	0.494	3.19	4.29	–
	hyperbolic	0.509	1.77	0.081	1.45
	linear	0.494	3.39	4.64	0.129
global	electron gas	0.213	0.494	0.428	$h$ ( $\text{\AA}$ )
				$\tau$ ( $10^{-15} \text{ s}$ )	–0.14
	time	0.873	–	3.63	1.77

Table 7.1: The neutralization constants obtained by fitting the charge-exchange parameterizations discussed in the text to the ion-fraction data for 8 keV  $\text{Ne}^+$  ions scattering from the Ni(100) surface. The tangent and time parameterizations have two fit parameters and the others have three.

Type	Param.	$\chi^2$	$a$ ( $\text{\AA}^{-1}$ )	$A_{(0)}$ ( $10^{15} \text{ s}^{-1}$ )	$A_1$ ( $10^{15} \text{ s}^{-1}$ )
local	tangent	0.0741	1.40	0.495	–
	hyperbolic	0.0753	1.53	0.494	0.128
	linear	0.0791	0.983	0.116	0.092
global	electron gas	0.0941	3.39	0.244	$h$ ( $\text{\AA}$ )
				$\tau$ ( $10^{-15} \text{ s}$ )	0.277
	time	0.0896	–	6.80	0.022

Table 7.2: The neutralization constants obtained by fitting the charge-exchange parameterizations discussed in the text to the ion-fraction data for 4 keV  $\text{Ne}^+$  ions scattering from the Ni(100) surface.

Type	Param.	$\chi^2$ ( $\times 10^6$ )	$a$ ( $\text{\AA}^{-1}$ )	$A_{(0)}$ ( $10^{15} \text{ s}^{-1}$ )	$A_1$ ( $10^{15} \text{ s}^{-1}$ )
local	tangent	48.8	1.53	9.36	–
	hyperbolic	51.4	1.32	7.42	0.626
	linear	50.9	1.89	4.17	4.77
global	electron gas	48.6	1.02	4.09	$h$ ( $\text{\AA}$ )
				$\tau$ ( $10^{-15} \text{ s}$ )	1.51
	time	59.1	–	2.77	6.09

Table 7.3: The neutralization constants obtained by fitting the charge-exchange parameterizations discussed in the text to the ion intensity data for 1 to 5 keV  $\text{Ne}^+$  ions scattering from the Ni(100) surface. The normalization parameter is not listed.

homogeneous electron gas in the jellium approximation, Eq. (7.2). Most of the data is fitted within the experimental error with this neutralization rate.

In order to investigate the dependence on the primary energy, the parameterizations were also fitted to ion fraction data for 4 keV Ne<sup>+</sup> ions scattering from the Ni(100) surface. The result of this is shown in figure 7.3 and the values of the neutralization constants are summarized in table 7.2. As was the case for the 8 keV data, all fits reproduce the mean features in the experimental data. The variation in the value of  $\chi^2$  is rather small. Note that in this case the ratio of the number of parameters (3 to 4) and the number of data points (32) is rather low.

As can be seen in figure 7.3, the largest difference between the experimental and fitted data is found in the  $\langle 100 \rangle$  direction for all parameterizations. (The same can also be observed in figure 7.1a, although less clearly.) In this case the divergence of the primary ion beam seems to be estimated quite well. Therefore, the difference between the fitted and experimental data must be due to experimental circumstances, which were not considered in the simulation. Firstly, experiments indicate that neutrals scattering from up to the ninth layer contribute to the total intensity [2], while only the first four layers were considered in our simulations. Secondly, the thermal vibrations of the surface atoms were neglected. These have a significant influence on the scattering cross sections under special scattering conditions [4], which is the case in the  $\langle 100 \rangle$  direction. The neutralization rates of the local parameterizations for the 4 keV ion fraction data are shown in figure 7.4. The tangent and hyperbolic parameterizations are in reasonable agreement: the linear parameterization deviates significantly. Comparing the values of  $\chi^2$  in table 7.2, it appears that the linear parameterization does not fit as well to the data as the other two. However, given the relative small amount of experimental data and the small differences in  $\chi^2$ , we conclude that also at 4 keV none of the local parameterizations is to be preferred above the others.

Comparing the figures 7.2 and 7.4, we see that there is a reasonable agreement between the neutralization rates for 8 and 4 keV. In order to investigate whether the energy dependence is reproduced by our simulations, the models were also fitted to energy-dependent ion-intensity data. The results of these fits are shown in figure 7.5 and table 7.3. In order to fit the simulation data to the experimental data, an extra parameter was added in order to normalize the simulated intensities to the measured ones. Again, all parameterizations fit to the data equally well. This can be apprehended when one realizes, that all parameterizations have the same dependence on the velocity ( $\sim 1/\sqrt{E}$ ). Unfortunately, the experimental error is rather large. Despite this, the neutralization rates for the local parameterizations, which are shown in figure 7.6, are in reasonable agreement with those obtained before. Therefore, we conclude that the combination of the energy dependence of the parameterizations and the cross sections obtained from the simulations, accounts for the observed energy-dependent behaviour of the ion-intensity data.

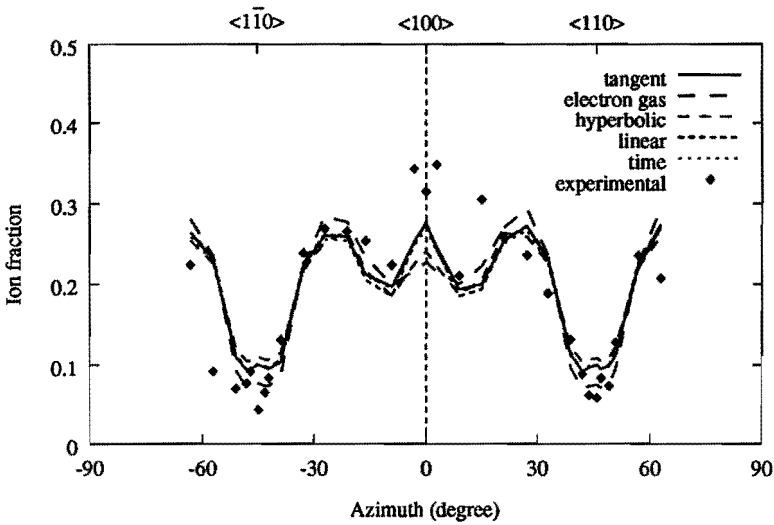


Figure 7.3: The results of fitting the charge-exchange parameterizations discussed in the text to the ion-fraction data for 4 keV  $\text{Ne}^+$  scattering from the Ni(100) surface. The angle between the primary ion beam with the surface is  $21^\circ$ .

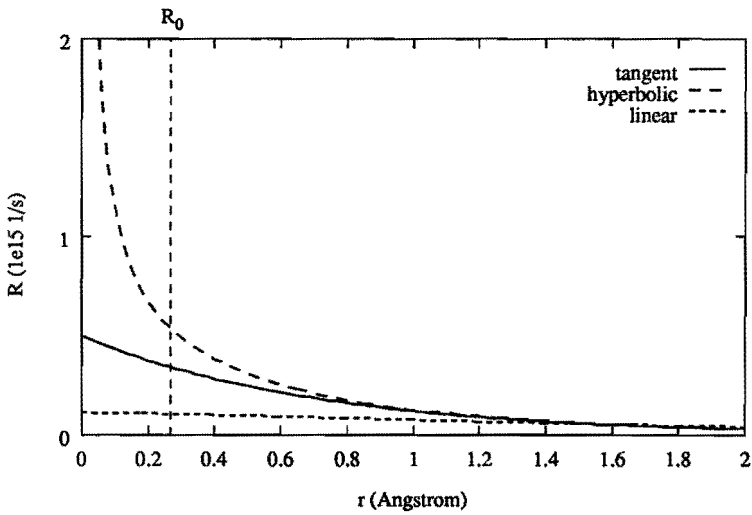


Figure 7.4: The neutralization rates of the local parameterizations as a function of the ion-atom distance for 4 keV  $\text{Ne}^+$  ions scattering from the Ni(100) surface. Note that the distance of closest approach,  $R_0$ , for a head-on collision is  $\approx 0.27 \text{ \AA}$  at this energy.

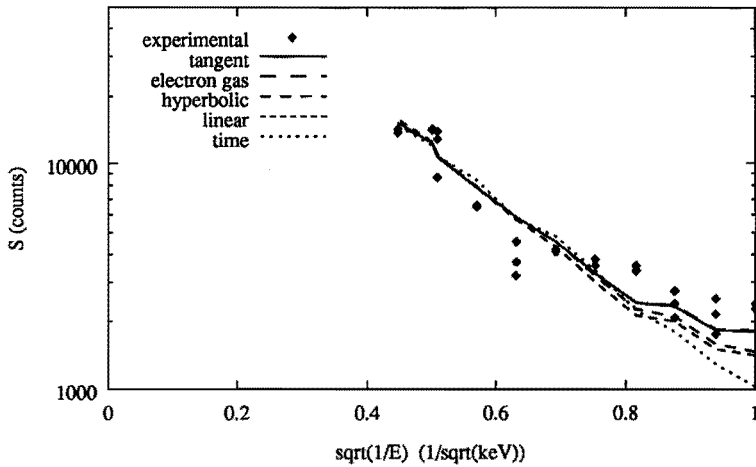


Figure 7.5: The results of fitting the charge-exchange parameterizations discussed in the text to the ion intensity data for 1 to 5 keV  $\text{Ne}^+$  scattering from the Ni(100) surface. Note that the noise in the simulation results (the curves) is due to the statistics.

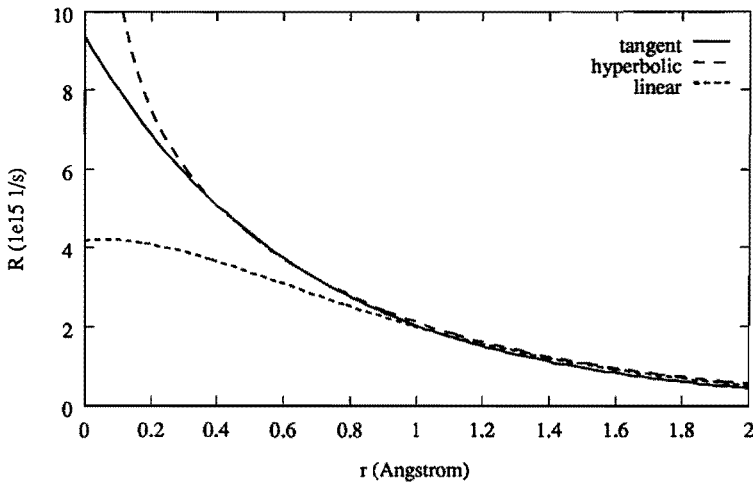


Figure 7.6: The neutralization rates of the local parameterizations as a function of the ion-atom distance for 1 to 5 keV  $\text{Ne}^+$  ions scattering from the Ni(100) surface.

## 7.5 Discussion

Comparing all the results from section 7.4, it is surprising that the fits with both local and global parameterizations reproduce the experimental data equally well. As a consequence, one cannot determine from the goodness-of-fit, whether the neutralization is due to the core or the valence electrons. However, the range of the neutralization rate for the (local) tangent parameterization can also be used for this purpose using the following argument. In the case that the neutralization is only due to the core electrons, the neutralization rate of the local parameterizations must be negligible at distances comparable to half the lattice constant of the Ni(100) surface,  $d = 1.25 \text{ \AA}$ . Thus, the neutralization is local when

$$e^{-ad} \ll 1, \quad (7.8)$$

and global when

$$e^{-ad} \approx 1, \quad (7.9)$$

However, none of these regimes stands out clearly ( $e^{-ad} \approx 0.16$ ).

An ion can be neutralized by the core electrons only during a violent collision. The survival probability of the ion due to the neutralization by the valence electrons is determined by the time the ion spends in the solid. Put to its extreme, local (core) neutralization is a function of the number of collisions, and global (valence) neutralization of the time. Therefore, it is interesting to plot the mean time-of-interaction,  $t$ , versus the average number of violent collisions per trajectory,  $N$ , as is done in figure 7.7. It appears, that there is a relation between these two quantities, which is approximately linear within the error. We note, that using a different distance,  $h$ , results in a shift of  $t = 0$ , and that by decreasing the maximum value,  $R_{max}$ , the slope of the line is increased. Hence, the fitting optimizes the parameters in the correlation  $N \approx C(t - t_0)$ :  $C$  is equivalent to  $1/\tau$  in Eq. (7.3) and  $t_0$  is determined by  $h$ . This is the reason, that similar results are obtained by fitting the local and global parameterizations.

It appears, that it is not sufficient to consider only one representative ion trajectory, when comparing experimental and theoretical (simulation) results. This is due to the fact, that the relation found here can only be incorporated by using a large number of ion trajectories. As a consequence, the multitude of the ion trajectories is relevant, when comparing experimental and theoretical results for charge exchange. Therefore, a comparison between quantum-mechanical calculations and experimental data is only useful, when either a large number of trajectories is considered in the calculations or the experimental data on a single trajectory is used. We note that our results were obtained a nickel surface. Different results might be found for other ions and surfaces containing other elements or two or more elements. However, no high-quality data on the ion fractions is presently available on such surfaces. In



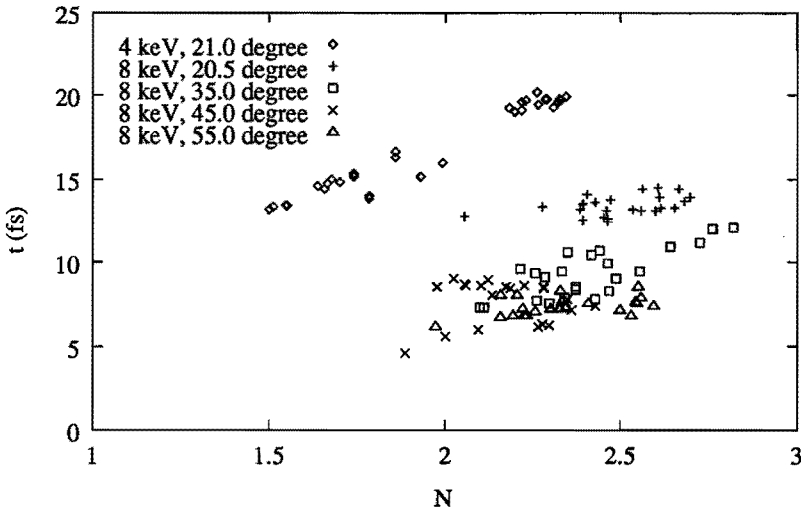


Figure 7.7: The mean time-of-interaction between the ions and the surface,  $t$ , plotted as a function of the average number of collisions per trajectory,  $N$ . The mean time of interaction was determined using a plane of reference at a distance,  $h = 0.25 \text{ \AA}$ , above the top atom layer. Only the violent collisions with a distance of closest approach  $R_0 \leq R_{max} = 0.5 \text{ \AA}$  were counted.

addition, the quantum-mechanical calculations are much more complicated in the case of two or more elements.

To conclude this section, we note that Fauster and Metzner [20] have suggested, that in the case of nickel reionization might occur, when an ion penetrates into the L-shell. For  $\text{Ne}^+$  ions a kinetic energy of about 3 keV is required. The distance of closest approach for a head-on collision at this energy is  $\approx 0.30 \text{ \AA}$ . However, none of the neutralization rates for the local parameterizations obtained from the fits become negative below this critical distance. Therefore, it appears that reionization does not occur when  $\text{Ne}^+$  ions scatter from a nickel surface up to an energy of 8 keV.

## 7.6 Conclusions

We have studied the charge exchange, the neutralization as well as the ionization, for  $\text{Ne}^+$  ions scattering from the Ni(100) surface using local and global parameterizations. In contrast to earlier suggestions, no indications were found that reionization occurs up to a primary energy of 8 keV. It was shown, that in the case of  $\text{Ne}^+$  ions scattering from a nickel surface one cannot distinguish, whether the neutralization

is due to the core or the valence electrons. This is the result of a dependence between the mean time-of-interaction, which is related to the neutralization by the valence electrons, and the average number of violent collisions per trajectory, which determines the neutralization due to the core electrons. The multitude of relevant trajectories appeared to be the dominant effect involved. In order to verify this, additional experimental data on the ion fractions similar to those measured by Rabalais and Hsu is required both on single and multiple element surfaces. These could be combined with quantum-mechanical calculations for many trajectories. Seemingly, computational physics has reached a state-of-the-art level at which it can challenge TOF experiments and charge-exchange theory in order to shed new light on the issues posed in this paper.

## References

- [1] J.W. Rabalais, *Fundamental Aspects of Heterogeneous Catalysis Studied by Particle Beams*, H.H. Brongersma, R.A. van Santen, Eds., Plenum Press, New York, 1991
- [2] C.C. Hsu, J.W. Rabalais, *Surf. Sci.* 256 (1991) 77
- [3] P.A.J. Ackermans, G.C.R. Krutzen, H.H. Brongersma, *Nucl. Instr. Meth. B45* (1990) 384
- [4] C.A. Severijns, G. Verbist, H.H. Brongersma, accepted for publication in *Surf. Sci.* (Chapter 5 of this thesis.)
- [5] Z.L. Mišković, R.K. Janev, *Surf. Sci.* 166 (1986) 480
- [6] A. Ishii, *Surf. Sci.* 192 (1987) 172
- [7] Y. Muda, D.M. Newns, *Phys. Rev. B.* 37 (1988) 7048
- [8] H.D. Hagstrum, *Phys. Rev.* 96 (1954) 336
- [9] G. Engelmann, E. Taglauer, *Nucl. Instr. Meth.* B13 (1986) 240
- [10] B.J. Garrison, *Surf. Sci.* 87 (1979) 683
- [11] G. Bracco, M. Canepa, P. Cantini, F. Fossa, L. Mattera, S. Terreni, D. Truffelli, *Surf. Sci.* 269/270 (1992) 61
- [12] D.J. Godfrey, D.P. Woodruff, *Surf. Sc.* 105 (1981) 438

- [13] A. Richard, H. Eschenbacher, Nucl. Instr. Meth. B2 (1984) 444
- [14] J.-M. Beuken, E. Pierson, P. Bertrand, Surf. Sci. 223 (1989) 201
- [15] M. Aono, R. Souda, Nucl. Instr. Meth. B27 (1987) 55
- [16] G. Verbist, C.A. Severijns, H.H. Brongersma, J.T. Devreese, to be published (Chapter 6 of this thesis.)
- [17] O. Grizzi, M. Shi, H. Bu, J.W. Rabalais, Rev. Sci. Instrum. 61 (1990) 740
- [18] G.C. Nelson, J. Vac. Sci. Technol. A4(3) (1986) 156
- [19] V.Y. Young, G.B. Hoflund, A.C. Miller, Surf. Sci. 235 (1990) 60
- [20] Th. Fauster, M.H. Metzner, Surf. Sc. 166 (1986) 29

# Chapter 8

## A preliminary study of the tails in low-energy ion-scattering spectra

### 8.1 Introduction

Low-energy ion scattering (LEIS) is a very surface-sensitive analysis technique. In a typical LEIS experiment, a mono-energetic ion beam is incident at a sample surface. The backscattered ions are used to obtain information on the outermost atomic layers. The composition of these layers can be derived from the positions and intensities of the surface peaks in the energy spectrum. In many spectra a tail, which extends to the low-energy side from the surface peaks, is observed, similar to those shown in figure 8.1. The ions contributing to the intensity of such a tail, have collided with two or more atoms and, as result, have loosed more kinetic energy. Sometimes a tail extending to the high energy side is also present. In this case, the ions contributing to the tail have also collided with more than one surface atom, but they have loosed less energy. The tails are most prominent when ions with a low neutralization probability, such as hydrogen, are used. They can, however, also be observed for ions with a high neutralization probability, such as noble gas ions. Experiments show that in this case, reionization occurs [1]. The threshold energy for ionization can be obtained from the height ratio of the peak and the tail as a function of the primary energy [2] or by using a beam of neutrals instead of ions [3].

Although tails are observed for both crystalline and amorphous materials, there exists experimental evidence, that the shape of the tail is influenced by the structure of the surface. Such experiments were done by, e.g., Donnelly *et al.* [4]. They used a sputter beam to damage a nickel mono-crystal and a  $H_2^+$  beam to measure the spectra. We note that using a  $H_2^+$  instead of noble gas ions offers the advantage, that the charge exchange has a far smaller influence on the spectra. The spectra show, that the peak-tail ratio depends on the amount of ions applied per surface area during the sputtering (see figure 8.1). Furthermore, a difference is found between

the spectra obtained with the primary  $H_2^+$  beam directed in the  $\langle 011 \rangle$  and  $\langle 01\bar{1} \rangle$  directions.

The tails have also been studied using computer simulations, e.g., by Pierson *et al.* [5,6]. They obtained a reasonable agreement between experimental and simulation results by considering charge exchange only. The relation between the structure of the surface and the energy spectrum was not considered in their work. However, the amount of disorder does influence the intensity of the tail. As a result, the values obtained for the neutralization constants also depend on the disorder within the surface.

In this chapter a preliminary study of the tails in the LEIS spectra is presented. The SISS-92 computer code [7] is used for this purpose. The use of a simulation code offers the advantage, that the influence of the various parameters can be studied separately. The charge exchange, although important when noble gas ions are used, is not considered here, because it makes the interpretation of the simulation results more complicated. The relation between the LEIS spectra and the degree of disorder in the crystal is investigated. The influence of two factors on the tail is studied: (i) inelastic processes and (ii) structural effects. The first cause a loss of energy and, as a result, determine the electronic stopping of the particles. Structural effects are related to the geometry of the crystal and contain those effects, that determine the amount of disorder in the crystal: interstitial atoms, defects, amorphousness, and thermal vibrations.

The contents of this chapter is as follows: in section 8.2 the results of simulations of He atoms scattering from a tungsten surface are presented. The influence of inelastic energy loss, thermal vibrations, and the amount of disorder on the spectra is investigated separately. The results for a crystalline and an amorphous surface are compared and contrasted. In section 8.3 the relation between the amount of disorder in the surface and the LEIS spectrum is studied for the same surface. Tungsten is much heavier than helium. Since the mass ratio of the projectile and the target determines the elastic stopping of the projectiles, similar simulations were done for a silicon surface. The silicon atom is lighter than the tungsten atom and, as a result, the elastic stopping is larger. The results of these simulations are presented in section 8.4. Finally, the conclusions of this work are summarized in section 8.5.

## 8.2 The motion of helium through the bulk

The energy spectra resulting from the simulations for 1 keV He atoms scattering from the bulk-terminated W(100) surface are shown in figure 8.2. The data on this surface were obtained from Ref. [10]. The primary beam was directed perpendicular to the surface and information on all particles leaving the surface was collected. In each simulation, 20000 trajectories were calculated. The number of collisions per

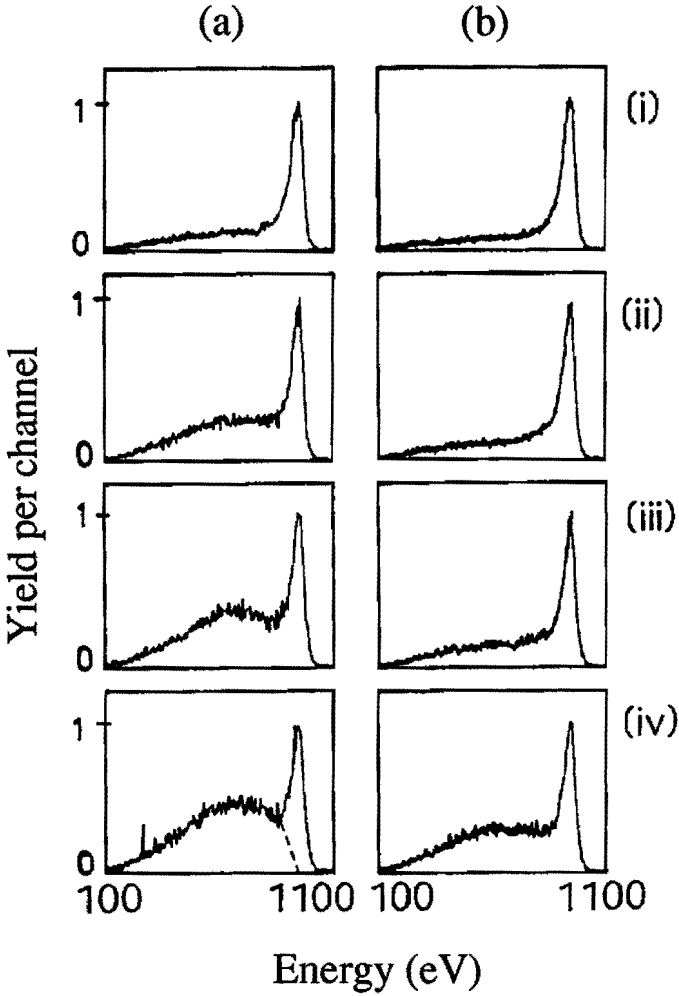


Figure 8.1: Low energy hydrogen scattering spectra from a Ni(110) mono crystal damaged by irradiation with 2 keV  $\text{Ne}^+$  ions along the  $\langle 011 \rangle$  axis by Donnelly *et al.* [4]. Analysis was performed with 2 keV  $\text{H}_2^+$  along (a) the  $\langle 011 \rangle$  immediately following Ne bombardment and (b) along the  $\langle 01\bar{1} \rangle$  direction. The spectra were collected following thermal annealing and irradiation with (i) 0, (ii)  $3 \times 10^{15}$ , (iii)  $6 \times 10^{15}$ , and (iv)  $12 \times 10^{15}$  Ne ions  $\text{cm}^{-2}$ . The spectra have been normalized to the surface peak height by multiplying with the following factors: (a) (i) 1.0, (ii) 0.83, (iii) 0.74, (iv) 0.79, (b) (i) 1.19, (ii) 1.03, (iii) 1.05, (iv) 1.12.

trajectory was limited to at most 1280 in order to ensure a limited time per simulation. Furthermore, the calculation of a trajectory was aborted, when the kinetic energy of the projectile dropped below 50 eV, because below this energy many-particle interactions can no longer be neglected [11]. The optimization implemented in the SISS-92 code was not used, because a large fraction (between 10 and 60%) of the particles was detected. Although the results presented here were obtained for 1 keV He atoms, similar results are obtained at (primary) energies in the range from 1 to 5 keV.

Four models were studied. In the first model, model A, a crystalline surface was used. In the energy spectrum (figure 8.2a) a broad peak is observed between 800 and 900 eV, which extends to lower energies. The surface peak is the small peak superimposed on this broad peak at about 900 eV. Inelastic energy loss was added in model B. The inelastic energy loss was calculated using the model by Oen and Robinson [8]. The energy spectrum is shown in figure 8.2b. The surface peak is shifted only a negligible amount due to the inelastic energy loss, but the broad peak is shifted significantly. In model C, thermal vibrations were incorporated. This was implemented by randomly displacing the atoms from their equilibrium position according to a normal distribution. The width of this distribution was derived from the bulk Debeye temperature and was 0.04 Å using the information from Ref. [9]. In figure 8.2c, the simulated spectrum is shown. The broad peak has been replaced by a tail, which extends from the surface peak to lower energies. The spectrum resembles some of the experimental spectra by Donnelly *et al.* [4] (see figure 8.1). In the last model (model D), both the inelastic energy loss and the thermal vibrations were incorporated. The spectrum shown in figure 8.2d is obtained. The intensity of the tail is distributed more homogeneous than is the case for model C. The faster decrease below 100 eV is due to the criteria used to limit the calculation time per trajectory.

In order to investigate the cause of the broad peak in the spectra of the models A and B, we have plotted the total energy loss of the particles leaving the surface versus the maximum depth reached by them (see figure 8.3). In the case of the models A and B (figures 8.3a and b), two branches in the distribution of the data points can be seen: the first with an almost linear relation between the depth and the total energy loss, and the second for which the energy loss does not depend on the maximum depth reached. These branches are most clearly seen in figure 8.3b, where the horizontal branch is shifted upward due to the inelastic energy loss. When thermal vibrations are introduced in the simulations (models C and D), the horizontal branch disappears, while the remaining branch extends to the maximum total energy loss of 1000 eV. The amount of backscattered particles as a function of the maximum depth is shown in figure 8.4. No significant differences are present between the models. The only difference is, that in the case of model D slightly less particles are backscattered from greater depths.

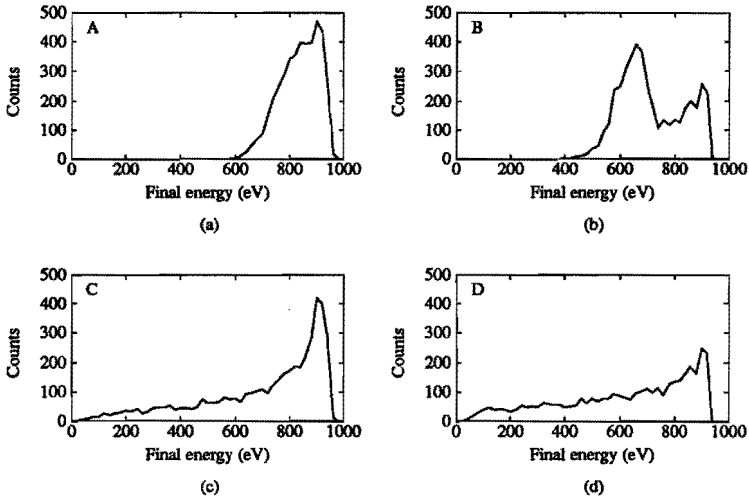


Figure 8.2: The simulated energy spectra for 1 keV He atoms scattering from the W(100) surface. In figure (a) a static crystal was used. Inelastic energy loss was added in figure (b). Figure (c) shows the spectrum in the case that thermal vibrations are incorporated. When both inelastic energy and thermal vibrations are considered, the spectrum of figure (d) is obtained.

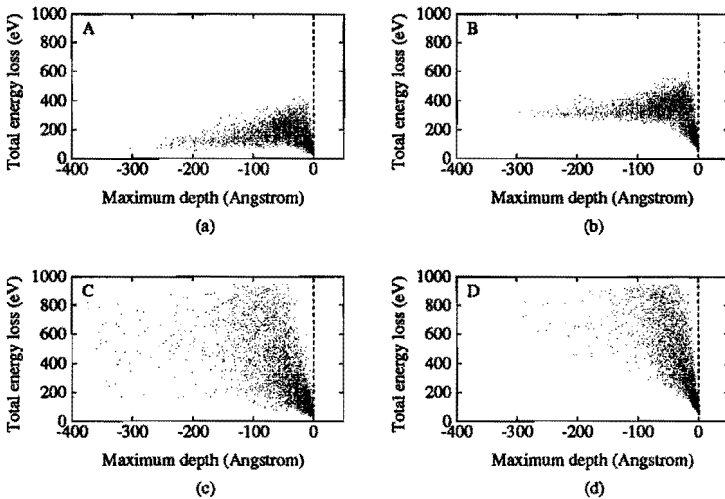


Figure 8.3: The total energy-loss versus the maximum depth reached for 1 keV He atoms scattering from the W(100) surface. The same models as in figure 8.2 were used.



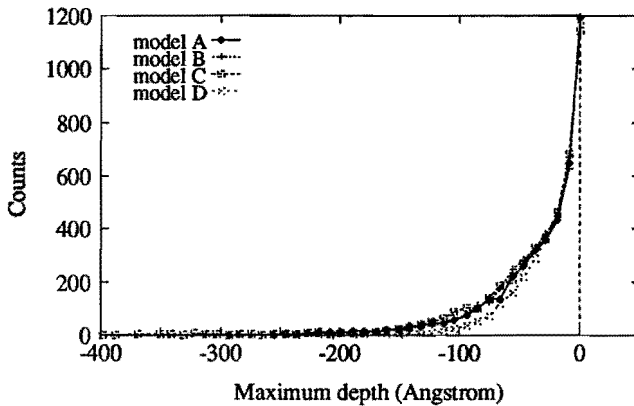


Figure 8.4: The number of ions leaving the surface versus the maximum depth reached for 1 keV He atoms scattering from the W(100) surface. The same models as in figures 8.2 and 8.3 were used. No significant differences can be seen, except that, in the case that both inelastic energy loss and thermal vibrations are considered (model D), the number of ions scattered from greater depths is slightly less.

From figures 8.3a and b, it appears that the particles contributing to the broad peak penetrate more than approximately  $50 \text{ \AA}$  into the crystal. By studying the trajectories of these particles in detail, the cause of the broad peak becomes apparent: on large parts of their trajectories the projectiles contributing to this peak have had only a few collisions. This is the result of a short-coming in the current implementation of the SISS-92 simulation code. The search algorithm applied in this code, uses a subdivision of the surface in cells Ref. [7]. Each cell contains exactly one atom. The facets of the cells are positioned halfway between the atoms. When an projectile collides with a target, the impact parameter has to be within the cell of the target. When this is not the case, a neighbouring atom is closer to the trajectory than the target and the projectile collides with the neighbouring atom instead. The same situation can occur for this neighbouring atom and, as a result, the projectile can move a large distance through the crystal without losing kinetic energy. Fortunately, this short-coming of the code is only important for surfaces thicker than about  $50 \text{ \AA}$ , as can be seen in figure 8.3. In this figure one can also observe, that adding thermal vibrations decreases the probability that this problem occurs. Without thermal vibrations the atoms are positioned in the center of the cells. The thermal vibrations move the atoms out of the center of the cells and, as a result, the process described above is less likely to occur.

Up to here, only a crystalline surface was considered. For comparison, similar simulations as presented above were done for an amorphous surface (indicated re-

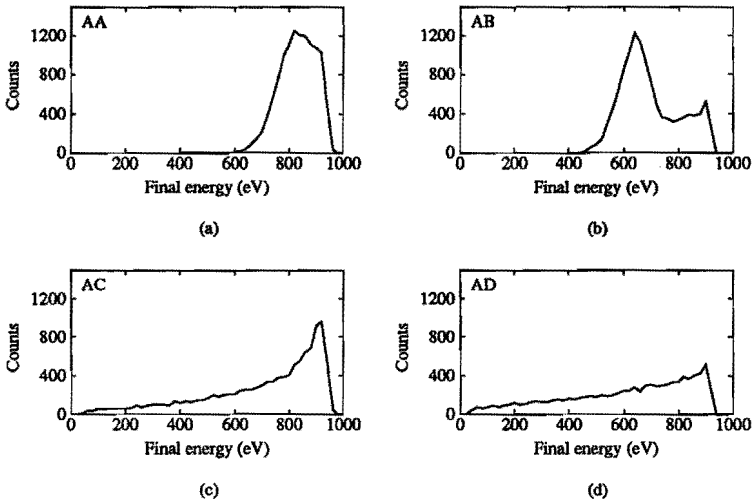


Figure 8.5: The simulated energy spectra for 1 keV He atoms scattering from an amorphous tungsten surface. In figure (a) a static crystal was used. Inelastic energy loss was added in figure (b). Figure (c) shows the spectrum in the case that thermal vibrations are incorporated. When both inelastic energy and thermal vibrations are considered, the spectrum of figure (d) is obtained.

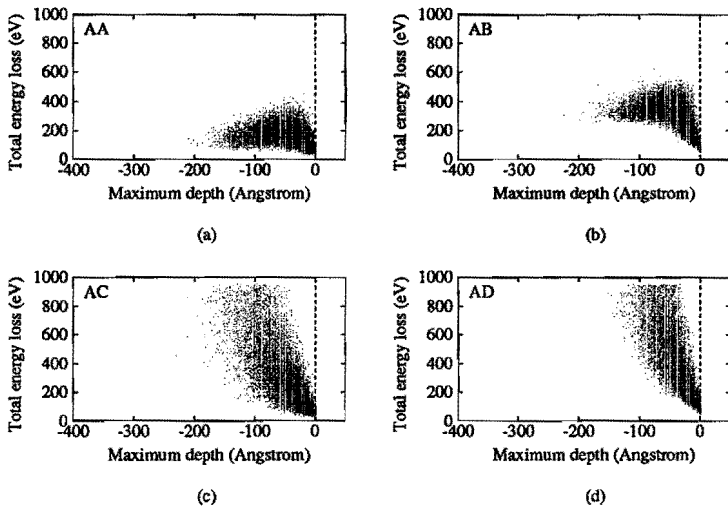


Figure 8.6: The total energy-loss versus the maximum depth reached for 1 keV He atoms scattering from an amorphous tungsten surface. The same models as in figure 8.5 were used.

spectively by models AA, AB, AC, and AD). The amorphous surface was simulated in the following manner: the total surface was constructed by repeating a column with an area of  $2 \times 2$  surface unit cells. In this column, the atoms were randomly displaced from their equilibrium position according to a normal distribution with a rms amplitude of  $0.7 \text{ \AA}$ . During the simulations, the positions of the atoms were fixed. Note that in this manner the atomic density of the amorphous and the crystalline surface are the same. All other parameters were not changed. The resulting energy spectra are shown in figure 8.5. The shapes of the spectra are similar to the spectra obtained for a crystalline surface. However, the number of backscattered ions has doubled. Furthermore, the intensity of the surface peak has decreased somewhat in comparison to the intensity of the tail.

Plots of the total energy loss as a function of the maximum depth reached in the case of an amorphous surface are shown in figure 8.6. In all models, the ions penetrate less deep into the amorphous surface than into the crystalline surface. A horizontal branch is present when thermal vibrations are not considered (models AA and AB). However, it does not extend as far as for the crystalline surface. The horizontal branch disappears when thermal vibrations are added.

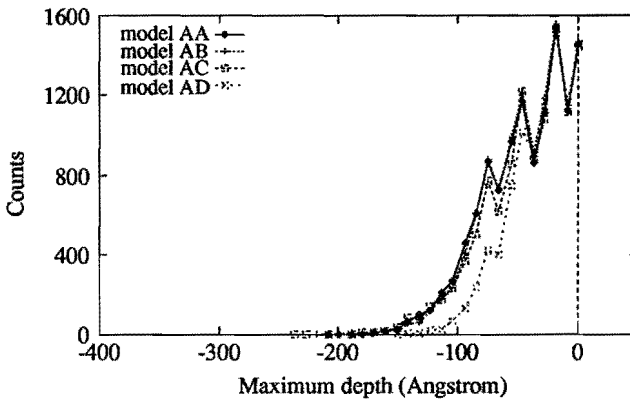


Figure 8.7: The number of ions leaving the surface versus the maximum depth reached for 1 keV He atoms scattering from an amorphous tungsten surface. The same models as in figures 8.5 and 8.6 were used. In the case that both inelastic energy loss and thermal vibrations are considered (model AD), the number of ions scattered from greater depths, is less than for the other models. Note that the peaks are due to the limited size of the column used to construct the surface.

In figure 8.7 the number of scattered ions is shown as a function of the maximum depth. The results for models AA, AB, and AC are nearly identical. Analogous to the case of a crystalline surface, the ions penetrate the surface less deeply in case

of model AD, but here the difference is much larger. The peaks in the first 100 Å are due to the manner in which the surface was constructed. Since a column of only  $2 \times 2$  surface unit cells was used, every atomic layer was distributed over four random layers only. The peaks disappear smoother when a larger column is used. The variation in the density of the data points in figure 8.6 is also the result of the small column size.

To conclude this section, we compare the results for the crystalline and amorphous surface. The most important difference is, that the intensity in the energy spectra for the models AC and AD in figure 8.5 is about twice the intensity in the energy spectra for the models C and D in figure 8.2. Due to the low energy resolution, it is not clear whether the surface peak increases in intensity. Comparison of the figures 8.3 and 8.6 shows us, that the extra intensity for the amorphous surface is due to the fact, that more particles are backscattered from greater depth.

### 8.3 Helium scattering from a tungsten surface

In the simulations discussed in section 8.2, the energy resolution is rather low, because the information on all particles backscattering from the surface is collected. To investigate the influence of the degree of disorder in the surface on the energy spectra in more detail, several simulations were done for different degrees of disorder. In these simulations, a rotational symmetric energy analyzer was simulated for the detection of the backscattered particles. This analyzer is equivalent to a cylindrical mirror analyzer without the energy-dependent resolution. The surface was taken 50 Å thick to ensure, that the short-coming of the simulation code discussed in section 8.2 had no influence on the spectra. Thermal vibrations were not taken into account. A total of  $10^6$  ion trajectories was calculated in each simulation. The amorphous surfaces were constructed by randomly displacing the atoms from their equilibrium positions within a cube. A homogeneous distribution was used for this purpose in order to simplify the analysis. Four amorphous surfaces were constructed in this manner for different values of the maximum displacement: (i)  $d = 0.125$ , (ii)  $d = 0.250$ , (iii)  $d = 0.375$  Å, and (iv)  $d = 0.500$  Å. The results, which are shown in figure 8.8. indicate that the intensity of the tail increases with increasing maximum displacement. The peak intensity, however, remains constant. This is not surprising, because the atomic density at the surface (and in the bulk) is the same for all surfaces.

The increase of the intensity in the tail can be apprehended in the following manner: consider a chain of atoms. For backscattering the effective cross section of a single perfectly aligned chain is approximately equal to the cross section of a single atom,  $\sigma$ . When the amount of disorder in the surface increases, the atoms are randomly distributed on an projected displacement area,  $A = 4d^2$ . When the

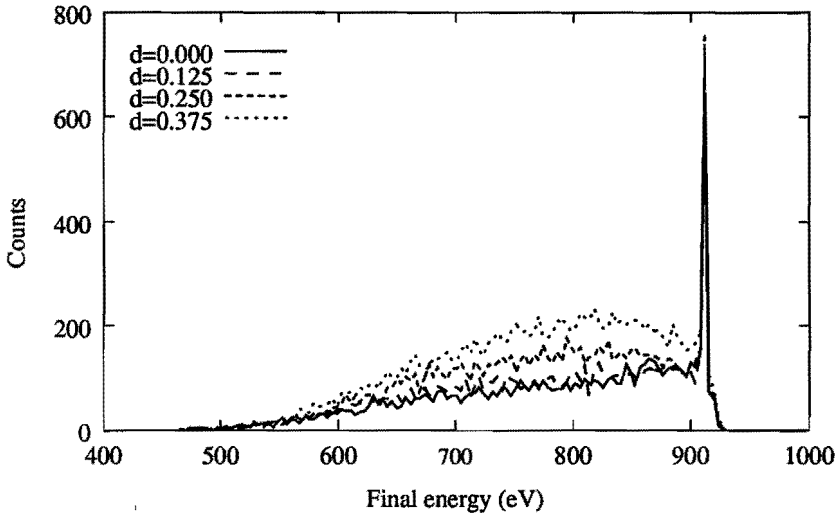


Figure 8.8: The energy spectra for four degrees of disorder in the surface for 1 keV He atoms scattering from a tungsten surface.

atoms are distributed homogeneously and  $A > \sigma$ , the total area,  $A_{n+1}$ , occupied by  $n + 1$  atoms is given by

$$\frac{A_{n+1}}{A} = \frac{A_n}{A} + \left(1 - \frac{A_n}{A}\right) \frac{\sigma}{A}. \quad (8.1)$$

In section 8.2 it was shown that the penetration depth of the backscattered projectiles is finite. Therefore, we suppose that the chain contains  $N$  atoms. Then, the ratio of the intensities can be written as

$$\frac{I_A}{I} \propto \frac{A_N}{\sigma}. \quad (8.2)$$

Here,  $I_A$  is the intensity for the disordered chain (amorphous surface) and  $I_c$  for the perfectly aligned chain (crystalline surface). In figure 8.9 the normalized intensity,  $I_A/I_c$ , is plotted as function of the normalized displacement area,  $A/\sigma$ .

In deriving Eq. (8.2) it was assumed that atom contributes only by single-scattering to the total intensity: shadowing and blocking have been neglected. The influence from neighbouring chains was also neglected. Despite this, a qualitative agreement can be obtained with the simulated data. Using the values of the displacement areas,  $A$ , in each simulation and a chain length  $N = 4$ , the curve shown in figure 8.9 was fitted.

When studying the shape of the tails, it appears that there are no details except statistical noise. This is the case for both the crystalline and the amorphous surfaces.

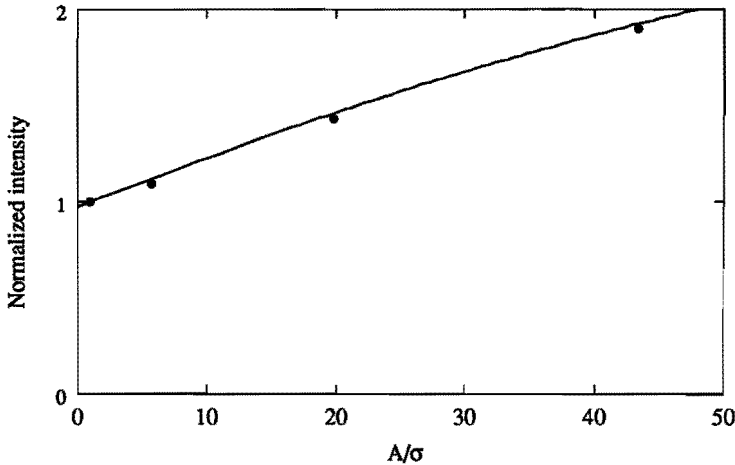


Figure 8.9: The normalized tail intensity,  $I_A/I_c$ , plotted versus the displacement area,  $A$ , normalized on the total single-scattering cross section,  $\sigma$ . The results from the simulations are indicated by the diamonds. The curve is the result obtained by adjusting Eq. (8.2) with  $N = 4$  to the simulation results.

Oscillations, similar to those found by Pierson *et al.* [5,6] and Orvek [12], are obtained after applying a convolution with a gaussian in order to account for the experimental broadening. However, the amplitude of these oscillations is smaller due to the improved statistics in our simulations. Furthermore, the oscillations are also present in the spectra for the amorphous surfaces. Therefore, we conclude, that these oscillations are the result of statistical noise and are not related to the crystal surface as suggested by Orvek [12].

Two simulations were done for layered surfaces: both surfaces are 16 bulk unit-cells thick, which corresponds to approximately 50 Å. The first consists of a crystalline layer of 25 Å on top of an amorphous layer. In the second surface the amorphous layer is on top. The amorphous layer is constructed by displacing the atoms homogeneously with a maximum displacement of  $d = 0.25$  Å. Both the simulated spectra are compared to the spectrum obtained for a crystalline surface in figure 8.10. The increase in the intensity of the tail is less than in the case of a completely amorphous surface. Furthermore, it seems, that in the case of the crystalline-amorphous surface, the tail deviates at a lower energy from the tail of the crystalline surface than in the case of the amorphous-crystalline surface. However, better statistics is required to obtain better information on this.

From the simulated spectra presented in this section it appears, that the intensity of the tail is related to the total amount of disorder in the solid. The results obtained

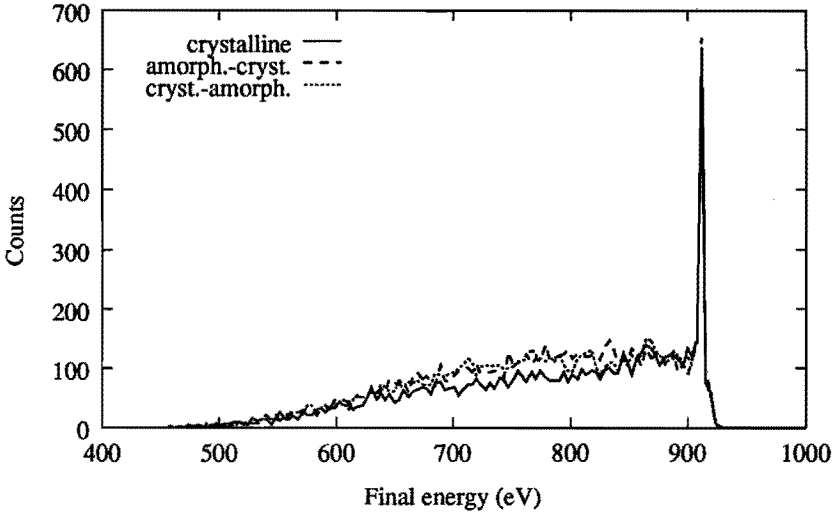


Figure 8.10: The energy spectra for 1 keV He scattering from a layered tungsten surface. The first spectrum was obtained for a surface consisting of a 25 Å thick crystalline layer on top of an equal thick amorphous layer. The second spectrum is the result for a similar surface with the amorphous layer on top of the crystalline. For comparison the spectrum for the crystalline surface from figure 8.8 is shown also.

for the layered surfaces suggest, that the shape of the tail in experimental spectra is not only determined by charge-exchange, but can also be due to a change of the amount of disorder as a function of the depth. As a result, detailed knowledge of the structure of the solid (and its surface) might be required when comparing the spectra obtained from simulations incorporating charge exchange with experimental spectra. As a final remark to this section we note, that other LEIS techniques, such as coaxial impact-collision ion-scattering spectroscopy (CAICISS) [13], are more sensitive to the structure of the surface. In CAICISS the total scattering angle is 180°. As a result, this technique is very sensitive for the alignment of the atoms.

## 8.4 Helium scattering from a silicon surface

In order to verify the validity of the results of section 8.3, simulations were done for 1 keV He atoms scattering from a silicon surface. In each simulation  $10^7$  trajectories were calculated and the inelastic energy loss was taken into account. A cylindrical-symmetric energy analyzer with an acceptance angle of 10°, which fixed the total scattering at 141.2°, was used as the detector. The following surfaces were

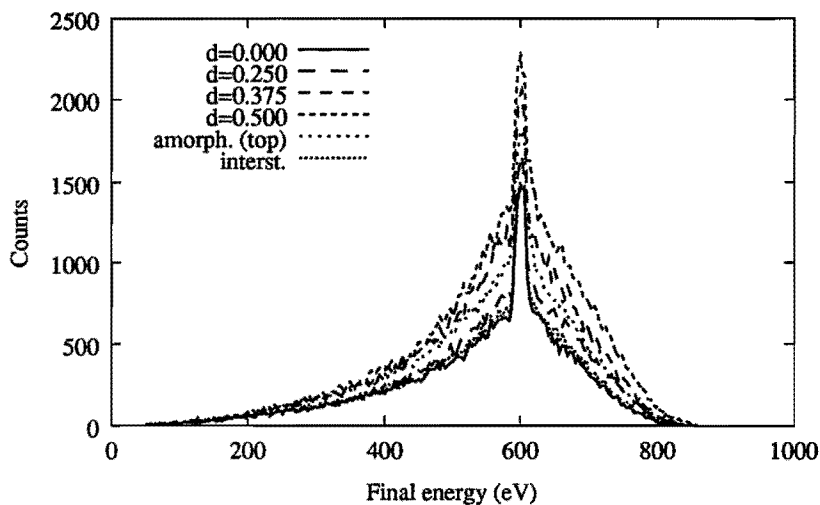


Figure 8.11: The energy spectra for 1 keV He scattering from seven types of silicon surfaces: a crystalline surface, three fully amorphous surfaces with an increasing degree of disorder, a surface with an 20 Å thick amorphous top layer on a crystalline substrate, a similar surface but with a crystalline layer on top of an amorphous substrate, and a crystalline surface with an displaced atom at a depth of 20 Å.

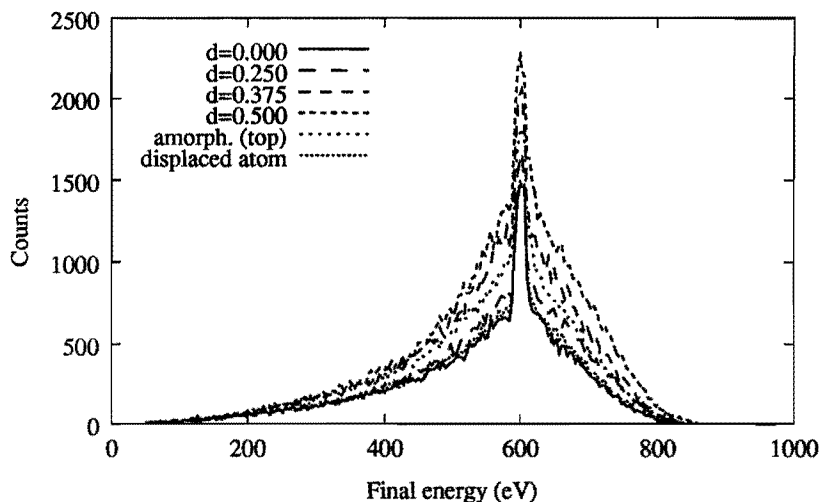


Figure 8.12: The energy spectra shown in figure 8.11 after subtraction of the spectrum for the crystalline Si(100) surface. Note that the surface peak is removed by the subtraction. In order to decrease the noise, the counts of four subsequent points in figure 8.11 were averaged.



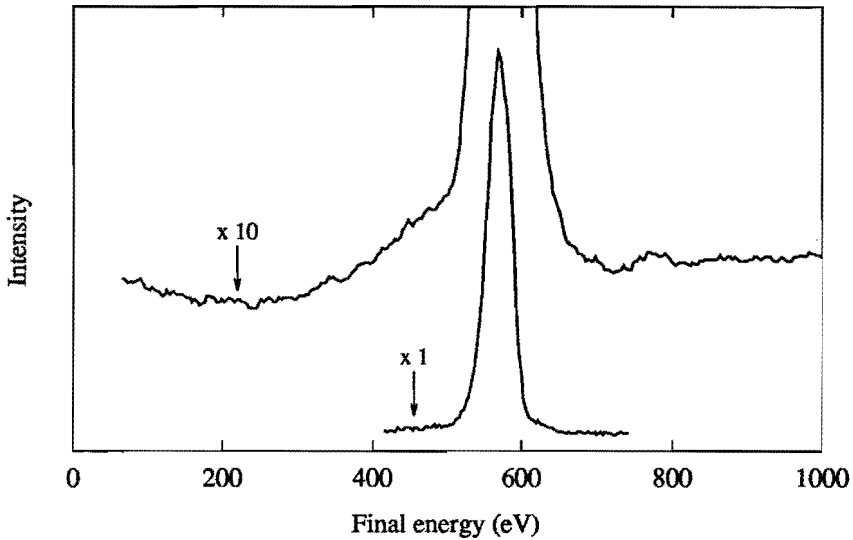


Figure 8.13: The energy spectra for 1 keV  $\text{He}^+$  ions scattering from the Si(110) surface. Both a tail at the low-energy and high-energy side of the peak is present. However, due to the neutralization the intensity of the tails is strongly reduced in comparison to the surface peak.

used in the simulations: firstly, a reconstructed crystalline Si(100)-(2 $\times$ 1) surface. The data on this surface were obtained from Ref. [14]. Secondly, three amorphous silicon surfaces, which were constructed from this Si(100)-(2 $\times$ 1) surface by randomly displacing the atoms from their equilibrium position within a square area with a maximum displacement of respectively 0.25 Å, 0.375 Å, and 0.5 Å. Thirdly, two layered surfaces: the one with a 20 Å thick amorphous layer on top of a crystalline substrate, and the other with a 20 Å thick crystalline layer on top of an amorphous substrate. Finally, a crystalline surface with a displaced atom at a depth of 20 Å was used. Note that in this case all atoms at this depth were displaced. All surfaces were taken 61 Å thick.

The results of the simulations are shown in figure 8.11. In each spectrum a large tail both at the low-energy and the high-energy side of the surface peak is present. Similar tails can also be observed in experimental spectra. An example is shown in figure 8.13 for 1 keV  $\text{He}^+$  ions scattering from the Si(110) surface. Due to the neutralization the tail intensity is strongly reduced in comparison to the peak intensity. We note that a smaller tail at the high-energy side is also present in the spectra of figure 8.8. Thus, it appears that the position of the tail relative to the surface peak

depends on the mass ratio of the projectile and the target.

The tail intensity increases with an increasing amount of disorder of the surface. This can be shown more clearly by subtracting the spectrum for the crystalline Si(100) surface from the other spectra (figure 8.12). We note, that also in this case the surface-peak intensity does not change, because the surface peak is not visible after the subtraction. This indicates, that the atomic density at the surface does not change. This is to be expected considering the manner in which the disordered surfaces are simulated. In general, the results are in agreement with those for the tungsten surfaces. Comparing the subtracted spectra for the layered surfaces with those for the fully amorphous surfaces, shows that the maxima in the subtracted spectra for the amorphous surface with  $d = 0.25 \text{ \AA}$  and for the surface with the displaced atom are shifted about 50 eV to higher energies. This is the result of the reconstruction, which disturbs the crystal structure up to a depth of about 8  $\text{\AA}$ . For both surfaces the displacement of the atoms due to the reconstruction is comparable to the displacement used in constructing the surface. This also explains the fact, that the curves for the surface with an amorphous top layer and with the single displaced atom have their maximum at the same energy.

Donnelly *et al.* [4] suggested several causes for the changes due to the sputtering observed in their experimental spectra: (i) the formation of interstitials and defects, (ii) the formation of solid noble gas precipitates, and (iii) the development of surface topography. From the results presented in this chapter, it appears that the latter is required in order to explain the decrease of the surface peak intensity. The increase of the tail intensity is due to the increasing amount of disorder in the solid. This intensity increase has a maximum as a function of the final energy. The simulation results suggest, that also a change in the amount of disorder as a function of the depth might cause a maximum in the tail intensity. However, it is not possible to distinguish the various types of disorder in the solid.

## 8.5 Conclusions

The scattering of helium from a tungsten and silicon surface was studied in order to investigate the correlation between the structure of the solid and the tails observed in LEIS spectra. The charge exchange was neglected. It was shown that the amount of disorder determines the penetration depth of the particles and the intensity of the tails in the spectra. The surface peak is not affected provided, that the atomic density of the surface is not changed. This suggests, that the decrease of the surface peak intensity in the experimental spectra by Donnelly *et al.* indicate, that the surface is roughened. The increase of the tail intensity is related to the increase of the disorder in the solid due to the sputtering. However, it is not possible to determine the exact type of disorder. In order to explain the different result obtained

for different directions of the primary ion beam, the influence of the direction of incidence of the primary ion beam has to be investigated. Furthermore, other types of disorder have to be studied, such as interstitial atoms in various atom rows of the solid.

## References

- [1] M. Aono, R. Souda, Nucl. Instr. Meth. B27 (1987) 55
- [2] G.C. van Leerdam, K.-M.H. Lenssen, H.H. Brongersma, Nucl. Instr. Meth. B45 (1990) 390
- [3] R. Souda, M. Aono, Nucl. Instr. Meth. B15 (1986) 114
- [4] S.E. Donnelly, R.G. Elliman, D.J. O'Conner, R.J. MacDonald, Nucl. Instr. Meth. B15 (1986) 130
- [5] E. Pierson, J.-M. Beuken, P. Bertrand, Surf. Sci. 214 (1989) 560
- [6] E. Pierson, J.-M. Beuken, P. Bertrand, Nucl. Instr. Meth. B45 (1990) 374
- [7] C.A. Severijns, G. Verbist, H.H. Brongersma, to be published (Chapter 5 of this thesis.)
- [8] O.S. Oen, M.T. Robinson, Nucl. Instr. and Meth. 132 (1976) 647
- [9] W. Eckstein, *Computer Simulation of Ion-Solid Interactions*, Springer Series in Materials Science 10, 1991
- [10] F.S. Marsh, M.K. Debe, D.A. King, J. Phys. C 13 (1980) 2799
- [11] D.M. Goodstein, S.A. Langer, B.H. Cooper, J. Vac. Sci. Technol. A6 (1988) 703
- [12] K.J. Orvek, Ph.D. thesis, Clarkson College of Technology 1983
- [13] M. Aono, M. Katayama, E. Nomura, T. Chassé, D. Choi, M. Kato, Nucl. Instr. Meth. B37/38 (1989) 264
- [14] R.M. Tromp, R.G. Smeenk, F.W. Saris, D.J. Chadi, Surf. Sci. 133 (1983) 137

# Summary

In this thesis, two aspects that are relevant for the interpretation of data obtained with the surface analysis technique low-energy ion scattering (LEIS) are studied: neutralization and the tail at the low-energy side of the surface peak in energy spectra. For this purpose, a new simulation code was developed called SISS-92 (Simulation of Ion-Surface Scattering 1992).

With LEIS both the chemical composition and the structure of a surface can be determined. In chapter 1, the differences that can appear between the surface and the bulk, are pointed out. Furthermore, an overview is given of the computer models in the literature, that are applied to ion-scattering simulation.

In chapter 2 the theory on LEIS is summarized, which is required for understanding the remainder of this thesis and which is implemented in the simulation code. An often-used model is the binary collision approximation (BCA). In this model, the interaction of the ion with the surface is described by a sequence of two-particle collisions. The binary collisions are described using classical mechanics, while the quantum-mechanical details of the collision are incorporated in the interaction potential of the two particles. In each collision, the ion loses a part of its kinetic energy to the target atom. The interaction of the ion with the electrons in the surface results in an inelastic loss of energy. The interaction with the electrons can also result in charge exchange between the ion and the surface. As a result, the ions can be neutralized and neutral particles can be (re-)ionized. Since in LEIS only the ionized particles, which are backscattered from the surface, are detected, a good understanding of the processes resulting in charge exchange, is important.

The usefulness of a code for ion-scattering simulation is not only determined by the physics modeled in it, but also by the amount of computer time it requires. This time can be reduced by a well-designed structure of the code and by using efficient numerical techniques and algorithms. The structure of the SISS-92 code is described in chapter 3. When selecting a numerical technique, its accuracy is a major consideration. An efficient and accurate numerical approximation of the classical collision integrals is based on rational functions. An algorithm for calculating such an approximation is described in chapter 4. The searching for a target atom is also an often performed and time-consuming task in a simulation. A fast method for searching and for calculating the data needed in the searching, is given in chapter 5.

In this chapter, the results of simulations with the SISS-92 code are compared to experimental data. There is a good correspondence between simulation and experiment. Furthermore, the separate influence of thermal vibrations of the atoms in the surface and spread in energy and solid angle of the primary ion beam is also investigated in this chapter. It appears that the thermal vibrations only influence the peak-background ratio in the intensity profile, while the broadening of the peaks is mainly due to the instrumental imperfections.

In chapter 6, new analytical results are presented for the neutralization integral that generalize the results of Godfrey-Woodruff and Richard-Eschenbacher. The influence of the approximating ion trajectory is studied. It is shown that two aspects of the approximating trajectory have to be considered: firstly, the accuracy with which the distance of closest approach of the exact trajectory is reproduced. Secondly, how well the dependence of the velocity of the ion on the ion-atom distance approximated that of the exact trajectory. The new results compared with results from the literature by fitting. Furthermore, it is discussed how the new analytical results can be used in a simulation code.

Several charge-exchange models, both from the literature and chapter 6, are used in chapter 7 to study the neutralization of  $\text{Ne}^+$  ions scattering from the  $\text{Ni}(100)$  surface. Both localized and non-localized models are used. In two of the localized models, neutralization and ionization are combined. These are used to investigate the occurrence of ionization. Furthermore, the dependence of the ion fraction on the ion trajectory is investigated. Two types of experimental data are used for this purpose: ion fractions measured at various orientations of the ion-source and the detector with respect to the sample surface at 4 and 8 keV, and ion intensities as a function of the primary ion beam energy between 1 and 5 keV.

Finally, in chapter 8 the shape of the tails extending from the surface peaks in energy spectra are studied. Charge exchange is not considered, since this complicates the analysis of the simulation results. First, the influence of the surface structure on the transport of the ions through the surface is studied. Thereafter, the relation between the amount of disorder and the energy spectrum is studied. Both homogeneous and layered surface structures are used for this purpose.

# Samenvatting

In dit proefschrift worden twee aspecten die van belang zijn bij het interpreteren van meetgegevens verkregen met behulp van de oppervlakte analyse techniek lage energie ionenverstrooiing (low-energy ion scattering, LEIS) bestudeerd: de neutralisatie van de gebruikte ionen en de staarten aan de lage en hoge energie kant van de oppervlakte piek in energie spektra. Tevens wordt voor dit doel nieuw ontwikkelde simulatie programmatuur gepresenteerd genaamd SISS-92 (Simulation of Ion-Surface Scattering 1992).

Met behulp van LEIS kan zowel de chemische samenstelling als de structuur van een oppervlak bepaald worden. In hoofdstuk 1 wordt aangegeven waarin het oppervlak van de bulk kan verschillen. Verder wordt een overzicht gegeven van computer modellen die in de literatuur gebruikt worden voor de simulatie van ionenverstrooiing.

In hoofdstuk 2 wordt de theorie over LEIS samengevat, die de basis vormt voor de rest van dit proefschrift en welke in de simulatie programmatuur is geïmplementeerd. Een veel gebruikt fysisch model is de twee-deeltjes botsing benadering (binary collision approximation, BCA). In dit model wordt de interactie van het ion met het oppervlak beschreven door een reeks twee-deeltjes botsingen. De twee-deeltjes botsingen worden klassiek beschreven, waarbij de quantum-mechanische details in de interactie potentiaal van de twee deeltjes worden verwerkt. Bij iedere botsing verliest het ion een deel van zijn kinetische energie aan het atoom waarmee het botst. De interactie van het ion met de elektronen in het oppervlak, resulteert in inelastisch energieverlies. De interactie met de elektronen kan ook ladingsuitwisseling tussen het ion en het oppervlak tot gevolg hebben. Hierdoor kunnen geladen deeltjes genutraliseerd en neutrale deeltjes geïoniseerd worden. Aangezien in LEIS alleen de geladen deeltjes die van het oppervlak worden teruggestrooid, worden gedetekteerd, is een goed begrip van de processen die tot ladingsuitwisseling leiden belangrijk.

De bruikbaarheid van een programma voor ionenverstrooiingssimulatie wordt mede bepaald door de vereiste rekentijd. Deze kan bekort worden door een goed gekozen structuur van het programma en door gebruik te maken van efficiënte numerieke technieken en algorithmen. De structuur van de SISS-92 programmatuur wordt beschreven in hoofdstuk 3. Bij de keuze van numerieke technieken is ook de nauwkeurigheid van belang. Een efficiënte en nauwkeurige numerieke benadering van de

klassieke botsingsintegralen wordt verkregen met rationale funkties. In hoofdstuk 4 wordt een algoritme beschreven waarmee een dergelijke benadering kan worden berekend. Het bepalen van een botsingspartner is ook een veel voorkomende en tijdrovende handeling tijdens een simulatie. Een snelle methode voor het zoeken en voor het berekenen van de benodigde gegevens, wordt beschreven in hoofdstuk 5. In dit hoofdstuk worden de resultaten van simulaties met de SISS-92 programmatuur vergeleken met metingen. Er is een goede overeenkomst tussen simulatie en experiment. Tevens wordt afzonderlijk de invloed nagegaan van thermische vibraties van de atomen in het oppervlak en de spreiding in energie en ruimtehoek van de primaire ionenbundel. Het blijkt dat de thermische vibraties de piek-achtergrond verhouding bepalen, terwijl de verbreding van de pieken het gevolg zijn van de imperfecties in de gebruikte experimentele opstelling.

In hoofdstuk 6 worden nieuwe, analytische uitwerkingen van de neutralisatie integraal gepresenteerd, die de resultaten van Godfrey en Woodruff en van Richard en Eschenbacher generaliseren. De invloed van de in de benadering gebruikte ion baan wordt onderzocht. Voor een goede benadering van de ion baan zijn twee punten belangrijk: allereerst moet de afstand van dichtste nadering van de exacte baan zo goed mogelijk worden gereproduceerd. Ten tweede moet het verband tussen de radiële snelheid en de afstand tussen het ion en het atoom zo goed mogelijk overeenkomen. De nieuwe resultaten worden met die uit de literatuur vergeleken om hun bruikbaarheid te testen. Tot slot van dit hoofdstuk wordt aangegeven hoe de nieuwe resultaten voor de neutralisatie integraal gebruikt kunnen worden in een simulatie programma.

Met behulp van diverse modellen voor ladingsuitwisseling zowel uit de literatuur als uit hoofdstuk 6, wordt in hoofdstuk 7 de neutralisatie van  $\text{Ne}^+$  ionen die verstrooien aan het Ni(100) oppervlak bestudeerd. Modellen die zowel een gelokaliseerde als een niet-gelokaliseerde ladingsuitwisseling beschrijven worden gebruikt. In twee van de eerste soort worden neutralisatie en ionisatie gecombineerd. Deze worden gebruikt om na te gaan of ionisatie optreedt. Tevens, wordt het verband tussen de ionfractie van de door het ion gevolgde baan nagegaan. Twee soorten experimentele data worden hierbij gebruikt: ionfracties gemeten bij verschillende oriëntaties van het ionenbron-detektor systeem ten opzichte van het oppervlak bij een primaire energy van 4 en 8 keV, en intensiteitsmetingen bij verschillende energieën tussen 1 en 5 keV.

Tot besluit wordt in hoofdstuk 8 de vorming van staarten aan de oppervlakte piek in energie spektra bestudeerd. De invloed van ladingsuitwisseling wordt hierbij niet in rekening gebracht aangezien deze de interpretatie ingewikkelder maakt. Allereerst wordt bestudeerd hoe de structuur van het oppervlak het transport van de ionen door de bulk beïnvloed. Daarna wordt het effect van de mate van wanorde (amorfiteit) van het oppervlak op de vorm van de spectra bestudeerd. Hierbij worden zowel homogene als gelaagde oppervlakken gebruikt.

# Dankwoord

Zoals bij de meeste proefschriften het geval is, zijn ook bij het tot stand komen van dit proefschrift andere personen dan de auteur betrokken geweest. Bij deze wil ik hen bedanken voor hun bijdragen. Enkele van hen wil ik hier noemen.

Allereerst mijn eerste promotor, Hidde Brongersma, omdat hij mij de gelegenheid heeft gegeven om dit onderzoek te doen. Guy Verbist, vanwege de vele discussies, ideeën en adviezen gedurende de afgelopen jaren. Zonder hem zou het nemen van de vele hindernissen tijdens het onderzoek zondermeer meer tijd en moeite hebben gekost. Hans Ottevanger, die de basis voor dit onderzoek heeft gelegd. Tot slot, Vitek Koxa en Ron Pijpers, die een deel van de experimenten die in hoofdstuk 7 van dit proefschrift worden gebruikt, hebben uitgevoerd.



## Curriculum vitae

- 27 aug. 1963* Geboren te St.-Michielsgestel.
- juni 1981* Eindexamen Gymnasium  $\beta$ ,  
Jacob-Roeland lyceum, Boxtel.
- sep. 1981 – feb. 1987* Studie Technische Natuurkunde,  
Technische Universiteit Eindhoven.
- mrt. 1987 – feb. 1988* Militaire dienst.
- mrt. 1988 – aug. 1992* Promotie onderzoek in de groep  
Fysica van Oppervlakken en Grenslagen,  
Technische Universiteit Eindhoven.

# Publications

1. "Rational function approximation of the collision integrals",  
C.A. Severijns, G. Verbist, H.H. Brongersma, J.T. Devreese,  
Nucl. Instr. Meth. B64 (1992) 730
2. "Differential correction algorithm for a function of two continuous variables:  
application to the collision integrals",  
C.A. Severijns, G. Verbist, H.H. Brongersma, J.T. Devreese,  
Comp. Phys. Comm. 70 (1992) 459
3. "SISS-92: a computer code for the simulation of ion-surface scattering",  
C.A. Severijns, G. Verbist, H.H. Brongersma,  
Accepted for publication in Surf. Sci.
4. "Analytical results for the neutralization integral in LEIS",  
G. Verbist, C.A. Severijns, H.H. Brongersma, J.T. Devreese,  
Submitted to Nucl. Instr. Meth. B.
5. "Developments in low-energy ion scattering from surfaces",  
H.H. Brongersma, R.H. Bergmans, L.G.C. Buijs, J.-P. Jacobs, A.C. Kruseman,  
C.A. Severijns, R.G. van Welzenis,  
Nucl. Instr. Meth. B68 (1992) 207
6. "Simultaneous energy and angle resolved ion scattering spectroscopy: first  
results",  
R.H. Bergmans, A.C. Kruseman, C.A. Severijns, H.H. Brongersma,  
Submitted to Appl. Surf. Sci.

STELLINGEN

behorende bij het proefschrift

**Computer Simulation of  
Low-Energy Ion Scattering**

van

C.A. Severijns

4 december 1992

1. Gezien de grote variatie in de experimenteel bepaalde waarden van de correctiefactor voor de afschermingslengte in de twee-deeltjes interactiepotentiaal, is een betere definitie van de kritische strooihoek gewenst.

- *Th. Fauster, M.H. Metzner, Surf. Sci. 166 (1986) 29*
- *C.C. Hsu, J.W. Rabalais, Surf. Sci. 256 (1991) 77*

2. Bij het opstellen van parameterisaties voor neutralisatie in LEIS moet evenveel aandacht aan de benadering van de ionbaan als aan de radiële afhankelijkheid van de neutralisatiekans besteed worden.

- *Hoofdstuk 6 van dit proefschrift*

3. Het vergelijken van quantum-mechanische berekeningen voor de neutralisatie in LEIS met experimentele gegevens is nog niet goed mogelijk.

- *A. Ishii, Surf. Sci. 192 (1987) 172*
- *Y. Muda, D.M. Newns, Phys. Rev. B37 (1988) 7048*
- *Hoofdstuk 7 van dit proefschrift*

4. Met het beschikbaar komen van meer experimentele gegevens over de hoekafhankelijkheid van de ionenfractie zal het bestuderen van ladingsuitwisseling in LEIS pas goed mogelijk worden.

- *Hoofdstuk 7 van dit proefschrift*

5. De structuur van een simulatieprogramma is even zeer bepalend voor haar toepasbaarheid als de gebruikte fysische modellen.

6. De bewering van Aono en Souda dat een baanafhankelijke neutralisatie duidt op een lokalisatie van de neutralisatieprocessen in LEIS is onjuist.

- *M. Aono, R. Souda, Nucl. Instr. Meth. B27 (1987) 55*
- *Hoofdstuk 7 van dit proefschrift*

7. Het enige argument om nog de programmeertaal FORTRAN te gebruiken voor fysische modelberekeningen en simulaties is, dat het tijd en moeite kost om over te stappen naar een andere programmeertaal. Dit argument is alleen juist op de korte termijn.
  
8. Het wezenlijke verschil tussen componist en luisteraar is, dat de componist de harmonische verbanden in de muziek in de tijd *vooruit* hoort terwijl de luisteraar pas *achteraf* in staat is om deze te bepalen.
  
9. In tegenstelling tot wat Souda *et al.* beweren, draagt blocking significant bij tot de variatie in de door hen gemeten azimuthale verdeling van de ionenintensiteit aan NaCl.
  - *R. Souda, M. Aono, C. Oshima, S. Otani, Y. Ishizawa, Nucl. Instr. Meth. B15 (1986) 138*
  - *J.-M. Beuken, E. Pierson, P. Bertrand, Surf. Sci. 233 (1989) 201*
  
10. In tegenstelling tot wat de term “fuzzy logic” doet vermoeden, bevat de technologie die met deze term wordt aangeduid totaal geen logica.
  
11. Het al dan niet tonaal, poly-tonaal of atonaal zijn van muziek wordt niet door de componist maar door de luisteraar bepaald.
  
12. Het plaatsen van onafhankelijke verkeerslichten binnen elkaars invloedsgebied is een hoofdoorzaak van file-vorming.